

Elliptic Flow Measurement of Heavy-Flavour Decay Electrons in Pb-Pb Collisions at 2.76 TeV with ALICE

Dissertation

zur Erlangung des Doktorgrades
der Naturwissenschaften

vorgelegt beim Fachbereich Physik der
Johann Wolfgang Goethe-Universität
in Frankfurt am Main

von

Theodor B. Rascanu
aus Bukarest, Rumänien

Frankfurt am Main 2016
(D 30)

Vom Fachbereich Physik der Johann Wolfgang Goethe-Universität
als Dissertation angenommen.

Dekan: Prof. Dr. Rene Reifarth

Gutachter: Prof. Dr. Harald Appelshäuser
Prof. Dr. Henner Büsching

Datum der Disputation: 20.03.2017

Zusammenfassung

Der LHC Teilchenbeschleuniger am Kernforschungsinstitut CERN bei Genf wurde in der Hoffnung gebaut, Antworten auf aktuelle Fragestellungen der physikalischen Grundlagenforschung finden zu können. Fragen wie „Wie waren die Eigenschaften des frühen Universums?“, „Können wir erklären wie Masse entsteht?“ oder „Was sind dunkle Materie und dunkle Energie?“ sind dabei nicht nur für die Teilchenphysik von Interesse, sondern auch wichtige Problemstellungen der Astrophysik. Die Experimente am LHC wurden jeweils mit unterschiedlichen Zielsetzungen entwickelt. Das ALICE Experiment wurde vornehmlich dahingehend konzipiert, einen besonderen Materiezustand zu untersuchen. Der Zustand höchstmöglicher Dichte und Temperatur, wie man ihn heutzutage höchstens noch in den gewaltigsten Explosionen findet, die das Universum kennt: In dem letzten Todesstoß großer Sonnen, die in Supernova-Explosionen für einige Tage die Helligkeit einer ganzen Galaxie überbieten. In den vergangenen Jahrhunderten waren einige unserer Galaxie so nahe, dass sie tagsüber sichtbar waren. Geschichtlich betrachtet ist der zu untersuchende Materiezustand aber in einem noch viel größeren Zusammenhang wichtig: bei der „Geburt“ unseres Universum. Man geht davon aus, dass in der ersten Mikrosekunde das gesamte Universum aus eben diesem bestand.

In Anlehnung an das aus der Elektrodynamik bekannte Plasma wird dieser Zustand „Quark-Gluon-Plasma“ (QGP) genannt. Während in einem gewöhnlichen Plasma die Bestandteile der Atome (Atomkerne und Elektronen) sich frei bewegen, sind in dem QGP die Bestandteile der Protonen und Neutronen quasi frei: die Quarks und Gluonen. Zusammengefasst werden diese auch Partonen genannt. Aufgrund der Eigenschaften der starken Kernkraft ist dies nur dann der Fall, wenn genügend Energiedichte vorhanden ist. Unter normalen Bedingungen sind die Quarks und Gluonen in Hadronen gebunden. Man nennt dies auch das „Confinement“. Die Eigenschaft der starken Kernkraft, dass bei hohen Energiedichten das Confinement aufgehoben wird, nennt sich „Asymptotic freedom“. Ähnlich wie in thermodynamischen Phasenübergängen kann der Übergang von normaler Materie zu der QGP Phase dabei entweder über Energiezufuhr oder Dichteerhöhung geschehen, wobei entsprechend entweder ein heißes oder ein kaltes QGP entsteht. Die notwendigen Energiedichten sind dabei aber so hoch, dass dies unter Laborbedingungen nur in Schwerionenkollisionen geschehen kann.

Die annähernd auf Lichtgeschwindigkeit beschleunigten Bleikerne, die dazu Verwendung finden, treffen an speziellen Punkten im Beschleuniger zusammen, wo sich die beiden entgegengesetzten Strahlen schneiden. Dies sind eben jene Punkte, um welche die vier LHC Experimente gebaut wurden. Aus den beiden auf höchste Energie beschleunigten Strahlen treffen dort zwei Bleikerne, die aufgrund ihrer Geschwindigkeit stark Lorentz-kontrahiert sind und deren innerer Zeitablauf durch Zeitdilatation stark verlangsamt ist, in ultrarelativistischen Kollisionen aufeinander. Da Bleikerne eine gewisse Ausdehnung haben, die Nukleonen (Protonen und Neutronen) also eine gewisse räumliche Verteilung aufweisen, gibt es eine ganze Bandbreite von möglichen Stößen. Sie können sich entweder streifen, je halb oder voll treffen. Je zentraler der Stoß ist, desto mehr Nukleonen sind daran beteiligt. Diese werden

daher auch „Participants“ genannt, während die beim Stoß unbeteiligten Nukleonen „Spectators“ genannt werden. Sind genügend Participants aufeinander getroffen, so wird das Confinement aufgehoben und die Partonen sind dann für einen kurzen Zeitraum im entstandenen QGP ungebunden. Dies ist ein dann expandierendes Medium, welches sich mit der Zeit abkühlt. Es hat sich gezeigt, dass das expandierende Medium dabei hydrodynamisch beschrieben werden kann. Die nach der Kollision einsetzende kollektive Bewegung des Mediums wird auch Fluss genannt. Unterhalb der kritischen Temperatur hadronisieren die Partonen bis zum „chemical free-out“, wo durch das Beenden der inelastischen Stöße die Hadronenzusammensetzung festgesetzt bleibt. Im darauf folgenden „kinetic freeze-out“ werden schließlich auch elastische Stöße unterbunden, womit dann die Impulsverteilung der Hadronen festgeschrieben ist. In nicht-zentralen Stößen sind die Participants anisotrop im Raum verteilt. Die Exzentrizität der Participants spiegelt sich dann direkt in einer Exzentrizität des QGP wider. Die Form des QGP ist dabei ähnlich der eines American Footballs, dessen Symmetrieachse in der azimuthalen Ebene liegt. Diese steht senkrecht zu der Ebene, die von der Achse entlang des Teilchenstrahls und der Strecke, welche die Mittelpunkte der beiden sich treffenden Kerne verbindet, aufgespannt wird. Diese so definierte Ebene wird auch „Reaction Plane“ genannt. Dadurch, dass Teilchen, die das QGP durchqueren, in der azimuthalen Ebene also je nach Winkel unterschiedliche Wegstrecken durch das QGP zurücklegen müssen, führt die azimuthale räumliche Anisotropie des QGP zu einer azimuthalen Anisotropie in der Impulsverteilung der vom QGP abgestrahlten Hadronen. Aufgrund der Geometrie ist insbesondere das zweite harmonische Moment der Fourierzerlegung der Anisotropie betroffen. Dieses wird auch das „elliptische“ Moment genannt. Es stoßen aber nicht nur die Nukleonen der beiden Kerne aufeinander, sondern es können, aufgrund der extrem hohen kinetischen Energie, direkt die Partonen des einen Kerns mit denen des anderen in harten Stößen kollidieren. Deren Produkte bewegen sich dann innerhalb des Mediums und werden durch dieses beeinflusst. Äquivalent zu diesem Effekt der starken Kernkraft ist der elektromagnetische Energieverlust eines geladenen Teilchens beim Durchfliegen eines Gases. Durch das Betrachten dieser Produkte lassen sich dann Rückschlüsse über die Art und Weise der Interaktion mit dem Medium ziehen und somit auch über die starke Kernkraft selbst. Ein gutes Beispiel für Produkte von harten Partonenstößen sind schwere Quarks, sogenannte charm und bottom Quarks.

Der Energieverlust stark wechselwirkender Teilchen innerhalb des QGP ist zwar einerseits von Interesse, andererseits ergibt sich auch die Schwierigkeit, dass eben durch diese starke Wechselwirkung kaum etwas ungehindert nach außen dringt, sodass die Prozesse, die innerhalb des QGP stattfinden, wie hinter einem Vorhang ablaufen. Es gibt allerdings auch Teilchen, die Produkte von Zerfällen sind, die nicht stark wechselwirken: Die Leptonen. Wenn Leptonen innerhalb des QGP generiert werden, so können sie fast ungehindert nach außen gelangen. Sie stellen somit eine sehr geeignete Sonde dar. Ein wichtiger Vertreter der Leptonen ist das Elektron.

Damit erklärt sich auch das Ziel der vorliegenden Arbeit: Die Messung des zweiten harmonischen Moments der Anisotropie der azimuthalen Impulsverteilung von schweren Quarks stammenden Elektronen, welche in Schwerionenkollisionen von 2.76 TeV pro Nukleon erzeugt wurden. Damit sollen Rückschlüsse auf die Stärke

der Thermalisierung der schweren Quarks und auf die Weglängenabhängigkeit des spezifischen Energieverlustes bei der Wechselwirkung mit dem expandierenden Medium gezogen werden. Es wird dabei nicht gezielt nach den Zerfallsprodukten von **bestimmten** schweren Quarks beinhaltenden Hadronen gesucht, sondern es sollen die Elektronen von **allen** schweren Quarks beinhaltenden Hadronen gleichzeitig gemessen werden. Im Gegensatz zur direkten Messung soll somit eine möglichst große Statistik aufgenommen werden können. Dazu wird der elliptische Fluss aller Elektronen gemessen, die von schweren Quarks stammen könnten und anschließend der Anteil jener abgezogen, die nicht von schweren Quarks stammen.

Die dargestellten Prozesse, von der Kollision über das Deconfinement der Nukleonen in freie Partonen, bis hin zur Hadronisierung der Partonen, geschehen in einem Zeitraum, der ähnlich ist zu der Zeit die das Licht braucht, um das QGP selbst zu durchqueren ($\sim 10^{-24}$ s). Solch kurze Prozesse können nicht aufgenommen werden. Stattdessen werden die Zerfallsprodukte und deren Eigenschaften gemessen. Dazu werden um den Kollisionspunkt zwiebelartig verschiedene Detektoren aufgebaut, die unterschiedliche Aspekte der ausfliegenden Teilchen messen. Der dem Kollisionspunkt nächstliegende Detektor hat dabei die Aufgabe festzustellen, ob die ihn durchfliegenden Teilchen in der primären Kollision entstanden sind oder in sekundären Zerfällen. Im ALICE Experiment ist dafür das „Inner Tracking System“ (ITS) unter anderem zuständig. Ihn umgebend ist die „Time-Projection Chamber“ (TPC). Dieser Gasdetektor misst den Verlauf der Teilchenspuren und deren spezifischen Energieverlust und führt entsprechend die Impulsbestimmung und die Teilchenidentifikation durch. Die Identifikation der Elektronen geschieht in dieser Arbeit im Verbund mit dem „Time-Of-Flight“ Detektor (TOF), der mithilfe der Laufzeitmessung ebenfalls zur Teilchenidentifikation beiträgt. Dabei werden im ersten Schritt alle Spuren verworfen, deren Laufzeit weit außerhalb der zu erwartenden Laufzeit von Elektronen liegt. Im nächsten Schritt werden auch jene Spuren verworfen, deren von der TPC gemessene Energieverlust zu weit von der Erwartung abweicht. Diese Vorgehensweise soll sicherstellen, dass auch in jenen Impulsbereichen, wo einer der beiden Detektoren eine unzureichende Trennschärfe besitzt, trotzdem möglichst nur die Elektronen in die Messung einbezogen werden.

Die Analyse beruht auf Daten der ALICE Kollaboration, welche Ende 2011 aufgenommen wurden. Das zweite Moment der Anisotropie der Impulsverteilung der dabei gemessenen Elektronen wird mithilfe den weitverbreiteten „Event Plane“ und „Scalar Product“ Methoden ausgewertet und untereinander verglichen. Dabei wird die Anisotropie relativ zu der die Reaction Plane approximierenden Event Plane bestimmt, welche ihrerseits aufgrund der Anisotropie der in der Kollision erzeugten Teilchen gemessen wird. Diese wird in der vorliegenden Analyse mithilfe des V-Zero Detektors gemessen, welcher sich wegen seiner Positionierung im Experiment insbesondere dazu eignet, da aufgrund seines Abstands zu den in der TPC analysierten Teilchen andere nicht-kollektive Teilchenkorrelationen stark unterdrückt werden. Um eine möglichst reine und gut definierte Stichprobe an Elektronen zu erhalten, wurden nur Kollisionen und Teilchenspuren in die Stichprobe aufgenommen, deren Parameter nicht außerhalb strenger Grenzen vom experimentellen Aufbau vorgegebenen Betriebsoptimum abweichen. Infolge der Qualitätsüberwachung wurde eine suboptimale Kalibrierung der TPC vorgefunden. Diese Korrelation der TPC-Signale

mit der Multiplizität der aufgenommenen Kollisionen und dem longitudinalen Winkel der Teilchenspuren wurde in einer eigens durchgeführten Nachkalibrierung entfernt.

Die Elektronenidentifikation mithilfe von TPC und TOF lässt erwarten, dass eine gewisse Kontamination der Stichprobe auch unter optimalen Umständen nicht zu verhindern ist. Um festzustellen, wie stark die als Elektronen deklarierte Stichprobe mit anderen Teilchen verunreinigt ist, werden die TPC-Signale, auf deren Basis die letzte Stufe der Teilchenidentifikation erfolgt ist, mit passenden Dichteverteilungen gefittet. Aus den Integralen dieser Verteilungen innerhalb des Annahmereichs wird dann auf die Reinheit der Elektronen in der Strichprobe geschlossen. Der dazu implementierte Fitalgorithmus macht sich dabei zu Nutze, dass die Parameter der Verteilungen sich nur stetig und langsam mit steigendem Impuls verändern. Robuste und effiziente Fitmethoden wurden dazu aufbauend auf aktuelle Forschungsergebnisse implementiert, um die Trends der Parameter auch über die Bereiche hinweg verfolgen zu können, wo aufgrund der Kontamination signifikante Abweichungen unumgänglich sind. Als Dichteverteilung hat sich eine Kreuzung zweier bekannter parametrischer Dichteverteilungen als besonders gut einsetzbar erwiesen. Von der Normalverteilung ausgehend können damit Asymmetrie und Kurtosis stetig verändert werden, dabei steht nicht nur der gesamte leptokurtische Bereich zur Verfügung, sondern auch weite Teile des platykurtischen Bereiches. Um die gefundene Verteilung innerhalb des Fitalgorithmus gebrauchen zu können, mussten ihre Parameter orthogonalisiert werden. Dies geschah nur für die Parameter, die das erste und zweite Moment steuern und dies auch nur näherungsweise für die notwendige Region in der Umgebung des mesokurtischen Bereichs. Es ist aber prinzipiell möglich, die Approximation mithilfe der vergestellten Methode beliebig zu verbessern. Die Messung der Elektronen wird dann um die so bestimmte Kontamination korrigiert.

Die so gemessenen Elektronen stellen dabei die „inklusive“ Messung dar. Um auf die beabsichtigte Messung des elliptischen Flusses von schweren Flavours zu gelangen, müssen von dieser inklusiven Messung noch alle Komponenten abgezogen werden, die nicht von schweren Quarks stammen. Dies geschieht mithilfe einer Simulation der Zerfälle von leichten Hadronen und von direkten Photonen. Diese stellen die Hauptquellen der Elektronen des Hintergrundes dar. Dabei werden die gemessene Impulsverteilung und der gemessene elliptische Fluss von geladenen Pionen skaliert, um so die Spektren der anderen leichten Hadronen (Eta, Omega, Eta-prime und Phi) zu erstellen. Im Fall der direkten Photonen sind nicht nur die gemessenen realen Photonen wichtig, sondern zu gleichen Anteilen die sogenannten virtuellen Photonen. Im Gegensatz zu realen Photonen, die nur bei Vorhandensein von Detektormaterial in ein Elektronenpaar konvertieren können, kann die Photonenquelle bei ausreichender Energie auch direkt Leptonenpaare bilden. Diese Komponente ist in Photonenmessungen nicht enthalten und musste anhand der vorhandenen Daten für reale Photonen rechnerisch ermittelt werden. Die sich mit dieser Methode ergebende Menge an Leptonenpaaren wurde mit Messungen der Zerfallskanäle von sogenannten Dalitz-Zerfällen verglichen, es konnte eine sehr gute Übereinstimmung gefunden werden.

Die Zerfälle der in der Simulation generierten Hadronen in Elektronen wurden mithilfe der PYTHIA6 Bibliothek durchgeführt. Die Wahrscheinlichkeit und die Ki-

nematik einer Konversion von Photonen wurde in einer an die GEANT4 Bibliothek angelehnte Implementation berechnet. Die vorhandenen, auf GEANT3 basierenden, hochgenauen Routinen hatten sich als sehr langsam und ineffizient erwiesen, sodass mithilfe der eigenen Implementierung die Simulationszeit und die notwendige Speichergröße um über je eine Größenordnung gesenkt werden konnten. Die Elektronen der virtuellen Photonen folgen einer Kinematik, die dem Pionzerfall ähnelt. Es hat sich gezeigt, dass sich diese Kinematik für die vorliegende Analyse nicht signifikant von einer Konversion unterscheidet. Dies wurde bestätigt mit Vergleichen von Konversionen von Zerfallsphotonen und Dalitz-Elektronen, wo diese beiden Zerfallskanäle sich ebenfalls nicht signifikant voneinander unterscheiden.

Die so in der Simulation generierten Elektronen können schließlich jeweils, gewichtet auf Basis der Impulsverteilung ihrer Quellen, in den sogenannten Cocktail zusammengenommen werden. Um sicherzustellen, dass das Ergebnis stabil ist und sich andere Annahmen nicht signifikant auf den Cocktail niederschlagen, wurden systematische Tests durchgeführt.

Im letzten Schritt kann nun der Elektronencocktail von der inklusiven Messung abgezogen werden, was schließlich das Endergebnis dieser Arbeit darstellt. Das Ergebnis ist ein signifikanter elliptischer Fluss von schweren Quarks stammenden Elektronen, der sich in seinem Impulsverhalten und in der Abhängigkeit zur Zentralität entsprechend den hydrodynamischen Annahmen verhält, dass schwere Quarks ebenfalls am Fluss teilnehmen und/oder bereits frühzeitig thermalisiert sind und somit trotz ihrer großen Masse und anfänglich sehr hohem Impuls sehr stark mit dem umgebenden Medium interagieren. Dieses Ergebnis bestätigt somit sowohl die ALICE Messungen über den muonischen Kanal als auch die direkte Rekonstruktion der schweren Quarks enthaltenden Hadronen sowie die vorangegangenen Messungen am RHIC.

Insbesondere zusammen mit den entsprechenden Messungen des nuklearen Modifizierungsfaktors, wo die in Proton-Proton und Blei-Blei Kollisionen gewonnen Impulsspektren miteinander verglichen werden, ergibt sich eine Möglichkeit aktuelle Modellrechnungen einzuschränken.

Durch die zur Zeit vorgeschlagenen Verbesserungen an den ALICE Detektoren, welche für zukünftige Datenaufnahmeperioden zur Verfügung stehen werden, wird es möglich sein, mithilfe nur weniger Änderungen an dieser Analyse erste getrennte Ergebnisse für charm und beauty Flavours zu erhalten.

Abstract

The elliptic flow of heavy-flavour decay electrons is measured at mid-rapidity $|\eta| < 0.8$ in three centrality classes (0-10%, 10-20% and 20-40%) of Pb-Pb collisions at $\sqrt{s_{NN}} = 2.76$ TeV with ALICE at LHC. The collective motion of the particles inside the medium which is created in the heavy-ion collisions can be analyzed by a Fourier decomposition of the azimuthal anisotropic particle distribution with respect to the event plane. Elliptic flow is the component of the collective motion characterized by the second harmonic moment of this decomposition. It is a direct consequence of the initial geometry of the collision which is translated to a particle number anisotropy due to the strong interactions inside the medium. The amount of elliptic flow of low-momentum heavy quarks is related to their thermalization with the medium, while high-momentum heavy quarks provide a way to assess the path-length dependence of the energy loss induced by the interaction with the medium.

The heavy-quark elliptic flow is measured using a three-step procedure. First the v_2 coefficient of the inclusive electrons is measured using the event-plane and scalar-product methods. The electron background from light flavours and direct photons is then simulated, calculating the decay kinematics of the electron sources which are initialised by their respective measured spectra. The final result of this work emerges by subtracting the background from the inclusive measurement. A significant elliptic flow is observed after this subtraction. Its value is decreasing from low to intermediate p_T and from semi-central to central collisions. The results are described by model calculations with significant elastic interactions of the heavy quarks with the expanding strongly-interacting medium.

Contents

1	Introduction	3
1.1	The Origins of Particle Physics	3
1.2	The Standard Model of Particle Physics	4
1.2.1	Comparison of the Fundamental Forces	6
1.2.2	Asymptotic freedom	7
1.3	QCD Phase Diagram	9
1.4	Ultra-relativistic nucleus-nucleus collisions	10
1.4.1	Initial Conditions	10
1.4.2	Formation of the QGP	12
1.4.3	Hadronization	12
1.4.4	Signatures of the QGP	13
1.5	Units	14
2	Relativistic Kinematics	17
2.1	Minkowski Space	17
2.2	Lorentz Transformation	18
2.3	Important Relations	19
2.4	Invariant Cross Sections	21
3	Hydrodynamics of the QGP	23
3.1	Thermodynamic Definitions	23
3.2	Assumptions	24
3.3	Relativistic Hydrodynamics	25
3.4	Transverse Expansion	26
3.5	Transverse Mass Scaling	27
3.5.1	Breakdown of m_T -Scaling	29
3.6	Particle Ratios	31
3.7	Chemical and Kinetic Freeze-Out	31
3.8	Anisotropic Flow	32
3.9	Scaling Properties of Anisotropic Flow	34
3.10	Non-Flow Effects	34
4	Experimental Setup	37
4.1	The Large Hadron Collider	37
4.2	A Large Ion Collider Experiment (ALICE)	39
4.2.1	Orientation of the Coordinate System	40
4.2.2	Central-Barrel Detectors	40
4.2.3	Forward Detectors	45
4.2.4	Trigger Setup	47
4.2.5	ALICE-Software	47
5	Heavy-Flavour Elliptic Flow	49
5.1	Subtraction Method	50
5.2	Quantifying Anisotropic Flow	50
5.2.1	Event-Plane Determination	51

5.2.2	Measuring Flow Relative to the Event Plane	53
5.2.3	Event Plane Resolution	53
5.2.4	Scalar Product Method	55
6	Inclusive Electron Measurement	57
6.1	Data Sample and Run Selection	57
6.2	Event Selection	58
6.2.1	Pile-Up Protection	58
6.3	Track Selection	59
6.4	Particle Identification	61
6.4.1	TOF PID	61
6.4.2	TPC PID	61
6.5	TPC Post-Calibration	62
6.6	Contamination	62
6.6.1	Clean Samples	64
6.6.2	Fitting of the TPC signals	65
6.6.3	Contamination Results	66
6.7	Event-Plane Flatness	66
6.8	Event-Plane Resolution	68
6.9	Inclusive Electron Flow	69
7	Background Electron Cocktail	73
7.1	Virtual Photon Production	73
7.1.1	Numerical Considerations	75
7.1.2	Dalitz Decay Branching Ratios	77
7.2	Mother Particle p_T Spectra	78
7.2.1	Pion p_T Spectrum	79
7.2.2	m_T -Scaling Factors	81
7.2.3	Direct Photon p_T Spectra	82
7.2.4	Virtual Direct Photons	84
7.3	Mother Particle v_2 Spectra	84
7.3.1	Pion v_2 Spectrum	85
7.3.2	KE_T -Scaling	85
7.3.3	Direct-Photon v_2 Spectrum	87
7.4	Electron Generation	88
7.4.1	Decay Electrons	89
7.4.2	Conversion Electrons	89
7.4.3	Electrons from Virtual Direct Photons	91
7.5	Cocktail Mixing	94
7.6	Systematic Studies	94
7.6.1	Momentum Spectra Scaling	96
7.6.2	Reconstruction Resolution	96
7.6.3	Late Electrons	96

8	Background Subtraction	99
8.1	Signal-to-Background Ratio	99
8.1.1	Low-Mass Dielectrons	99
8.1.2	Reconstruction Efficiency and Resulting R_{SB}	100
8.2	Final Result and Discussion	101
8.2.1	Comparison to Model Calculations	102
8.3	Outlook	104
9	Summary	105
10	Appendix	107
10.1	Potential Energy	107
10.2	Radiation Length and Pair Production	108
10.3	Random Number Sampling	108
10.3.1	Inverse Transform Sampling	109
10.3.2	Rejection Sampling	109
10.4	Parametric Distribution Functions	109
10.4.1	Skewed Gaussian	109
10.4.2	“Variakurtic” Skewed Gaussian	111
10.5	Feature Detection	112
10.6	FAST-ELTS: An Efficiency Regaining Fast Least Trimmed Squares Fitter	112
10.7	Error Propagation	113
10.7.1	Linear Approximation	114
10.7.2	Deviations from Linearity	114
10.8	Figures for the Centralities 0-10% and 10-20%	114
	List of Figures	121
	List of Tables	122
	References	123

Preface

Ever since people asked why nature is as it is, and tried to find laws describing their observation, the understanding of how nature behaves evolved. One such law, for example, describes how apples fall onto Newton's head. Some other describe how planets orbit the sun. Very soon it was realised that these laws have a lot in common, and actually describe the same fundamental force from different perspectives: we now call this force "gravity". In the following centuries we have realized that there are also other fundamental forces, each having its own very special way of behaving. We call those other forces: electromagnetic, weak nuclear and strong nuclear force. Many questions have been answered up to now. But as it is very often the case, each answer comes at a price, and in science price tags usually say: "another even more fundamental question".

All physics fields like astrophysics, solid state physics, or nuclear physics have different perspectives on our universe. They can thus observe different aspects of the fundamental forces. The achievements in one field can lead to unveilings in others. Amusingly this mutual impact is very strong between two seemingly very distant fields: astrophysics and nuclear physics. In fact, both are not that distant at all when, for example, looking at the goals of current nuclear physics experiments:

- What were the properties of the very early universe?
- Can our models explain the origin of mass?
- What is dark matter, what dark energy?
- Can we explain the evolution of our universe?

These questions are obviously also very fundamental astronomical questions; answering all of those questions is the goal of the experiments built near Geneva at CERN.¹

Each field has its own very special methods of teasing out more knowledge from nature's seemingly bottomless reservoir. The way nuclear physics is today trying to endeavour its sub microscopic view of the world was first travelled by Ernest Rutherford with his scattering experiment. From his experiment we know that the naming of the so-called atom was premature: Since then nuclear physicists are engaged in finding the right description of the substructure of something we today still call "indivisible".

¹The first question is the search of the characteristics of the Quark-Gluon-Plasma, which we shall encounter again later; this will be addressed by ALICE. The second is the search after the Higgs Boson; ATLAS and CMS seem to have finally found this last missing particle of the Standard Model. The question about the nature of dark energy is assigned to CMS only, and last but not least LHCb will try to find out more about the CP-violation of the weak nuclear force, which is important for the asymmetry of matter and antimatter.

1 Introduction

This thesis will begin by introducing the reader to all concepts necessary for understanding the current work and its implications. The concept is that people unrelated to the subject should be able to at least grasp the basics. This is done by first laying out the fundamentals in a narrative style, starting from a quick historical review. For a more quantitative treatment Chapter 2 introduces the mathematical framework needed for Chapter 3 which will derive the physical relations needed in this work from basic principles. Chapter 4 then introduces the experimental setup used to perform the measurement before the idea to the analysis is presented in Chapter 5. The analysis itself is shown in Chapter 6 and Chapter 7 while the result is presented in Chapter 8. The work is then summarised in Chapter 9.

1.1 The Origins of Particle Physics

The idea that it is impossible to divide matter endlessly was a concept by early Greek philosophers. Thus it was thought that all matter is built out of smallest components, which they called $\alpha\tau\omicron\mu\omicron\varsigma$. Later, chemists of the 17th and 18th century showed that certain substances cannot be further divided by chemical methods. Those substances were called chemical elements and it was assumed that these elements were built out of atoms.

The idea of indivisible atoms had soon to be revised. First signs were the great number of elements and the periodicity of their characteristics. This became clearer as the first steps of the emerging nuclear physics were taken:

William Conrad Röntgen's discovery in 1895, the X-rays, led to an extensive search of other radiation sources. Just a year later Henri Becquerel discovered the radiation of uranium salts by their peculiarity of exposing photographic plates in the dark. In 1898 Marie Curie was able to show that this radiation must be an attribute of the uranium atoms themselves and cannot be explained by chemical reactions. She called this spontaneous radiation of the material "radioactivity". Due to the high radiation, Marie and her husband Pierre found two more elements later that year, Polonium and Radium.

Trying to bring some systematics into the different types of radiation, they were named alphabetically in Greek in the order of decreasing interaction with matter. In 1909 Rutherford's experiment of scattered alpha particles on a gold foil led to the conclusion that atoms consist of a small positively charged nucleus surrounded by negative electrons. Just two years later Niels Bohr joined the knowledge of quantum mechanics and the outcome of Rutherford's experiment into his model of the atomic structure.

The restriction to the distinct energies alpha particles have, being emitted by the sources, let soon arise ideas about how to accelerate those charged particles for further experiments. The particle accelerator was invented.

As in 1932 the neutron was found, the nucleus was complete and together with the prediction of the neutrino in 1930 all observations could be well described. This idyllic atmosphere soon vanished in 1937 as a new particle was detected coming with cosmic rays, the muon. The surprise about this unexpected particle, which

was found to be like an electron but heavier, is best summarised in I. I. Rabi's comment: "Who ordered that?"

Until the late 1950's literally hundreds of new particles were found in scattering experiments and could be arranged in two groups: leptons and hadrons. Because of the large number of hadrons the situation was comparable to the situation at the end of the 19th century; where there were simply too many chemical elements for these truly to be called elementary. It was not until the 1960's when deep-inelastic scattering experiments of electrons and nucleons finally made it clear that hadrons could not be elementary either and had to be built up out of even smaller components, which then were called partons [1–3]. However an unambiguous understanding of their nature was missing until the quark model proposed by Murray Gell-Mann and George Zweig [4, 5] became commonly accepted in 1964 as the predicted Ω^- particle was found [6].

This brought a high degree of tidiness into the overwhelming big "particle zoo" of the 1960's. Since then this theory evolved into what we today call the Standard Model. [7–9]

1.2 The Standard Model of Particle Physics

The Standard Model is a theory that describes the known particles and their interactions. At its base there are three quantum field theories: Quantum Electrodynamics (QED) [10], Quantum Chromodynamics (QCD) [11] and the Higgs theory [12]. QED describes the properties and interactions of particles carrying electric or weak charges while QCD describes colour-charged particles and the Higgs theory explains the emergence of mass of all particles.

Matter is composed of fermions, which are half-integer spin particles, while interactions are described as an exchange of the virtual vector gauge bosons of the respective field, which have an integer spin. Quarks and leptons are fermions respecting the Pauli Principle and obeying the Fermi-Dirac-statistics, whereas the bosons obey the Bose-Einstein-statistics, and do not respect Pauli's Principle. The Standard Model includes 12 fermions, 12 anti-fermions, 12 force mediating bosons and the long predicted and most probably finally found Higgs boson [13].

There are six quarks and six leptons and equally many antiparticles. Quarks possess all known charges, and interact thus via all known forces, which makes them unique in that way. They have a mass, they have electric charge and, as well as all other particles, they carry weak charge. In addition to that, quarks also carry another type of charge: the colour charge. Unlike electric and weak charge, of which there are two forms (plus and minus), mass has only one form, while colour charge has six: red, green, blue, anti-red, anti-green and anti-blue. Due to the so-called colour confinement (or just confinement) quarks are bound together to form colour-neutral composite particles. There are two known quark configurations, although more are imaginable [14]: a quark and an anti-quark form a meson, while three quarks form a baryon. These colourful names of the colour charges were chosen because of the following similarity: In principle one can think of the classical colour theory (in its additive form) where anti-red would be cyan, anti-green magenta and anti-blue would be yellow; the confinement would demand composite particles to be

	Generation			Charges					
	1	2	3	Mass m [eV/ c^2]			Electric z [e]	Colour	Weak T_z [g]
Quarks	u	c	t	2.3 M	1.27 G	173 G	2/3	r,g,b	1/2
	d	s	b	4.8 M	95 M	4.18 G	-1/3	r,g,b	-1/2
Leptons	e^-	μ^-	τ^-	511 k	106 M	1.78 G	-1	0	-1/2
	ν_1	ν_2	ν_3	≈ 0			0	0	1/2

Table 1.1: Eigenstates of the fermions according to the Standard Model [15]. The mass is shown for the mass eigenstates, and the weak charge is shown for the left handed weak eigenstates. The weak eigenstates of the neutrinos ν_e , ν_μ and ν_τ are linear combinations of the mass eigenstates ν_1 , ν_2 and ν_3 , and the weak eigenstates of the quarks d', s' and b' are linear combinations of the mass eigenstates d, s and b. For the charged leptons the mass and weak eigenstates coincide.

white.

The remaining six fermions, the leptons, all miss the colour charge, while the three neutrinos also miss the electric charge, which leaves them to interact solely by weak interaction, hence making them hardly detectable. Fermions are grouped in three generations, which are sorted by increasing mass. Second and third generation charged particles decay with very short half-lives, making all visible matter to consist of only first generation charged particles and the very weakly interacting neutrinos of all generations. Table 1.1 summarises the properties of the fermions.

In the Standard Model everything is embedded in the QED, QCD and Higgs quantum fields. When two particles approach each other, the force between them is described as an exchange of virtual gauge bosons. Each charge produces a correspondent fundamental force, and each force has its gauge bosons to mediate it. The higher the absolute amount of charge, the higher the force and the higher the coupling of the gauge boson to the particle. The bosons have to put back the distance between the interacting particles, by propagating through space. The more massive the boson the shorter the distance it can propagate. Both, the coupling and the propagation contribute to the effective strength of the force. Of course the bosons do not only exist in this virtual form, but also as real particles. In this case these are excitations of the respective quantum fields which materialize in the production of the real boson. For more on virtual particles see also Chapter 7.1.

The strongest force is the so-called strong nuclear force; it's mediated by the gluons between colour charged particles. There are eight gluons, each carrying another colour charge. These are the particles which bind colour charge carrying particles together, even themselves, thus their suggestive name. The next strongest fundamental force is the electromagnetic force, which is mediated by the (electrically neutral) photon between electrically charged particles. Since there is a strong nuclear force, we also know of a weak nuclear force: this is mediated by the massive W^+ , W^- and Z^0 bosons between all fermions. This force is the only one to not produce bound compounds, and can thus only be sensed by the transitions it generates, which otherwise would be forbidden; e.g. the beta decay of unstable isotopes (Table 1.2 summarises the properties of the bosons).

The symmetries which are at the base of QED strictly forbid any explicit mass

Interaction	Couples to	Gauge Boson	Mass m [GeV/ c^2]	El. z [e]	Col.	Weak T_z [g]	eff. Range	rel. eff. Strength
Strong	colour	8 gluons	0	0	yes	0	10^{-15}	1
Electromg.	electric	photon	0	0	0	0	∞	10^{-2}
Weak	weak	W^\pm, Z^0	80, 91	$\pm 1, 0$	0	$\pm \frac{1}{2}, 0$	10^{-18}	10^{-14}
Gravitation	mass	graviton ?	0	0	0	0	∞	10^{-38}

Table 1.2: The interactions and their gauge bosons [7]. Each gluon has one of the following colour combinations: $r\bar{g}, r\bar{b}, g\bar{r}, g\bar{b}, b\bar{r}, b\bar{g}, r\bar{r} - g\bar{g}, r\bar{r} + g\bar{g} - b\bar{b}$. Only for the W^\pm bosons does the indicated weak charge directly show the coupling strength. The Z^0 coupling is given by $\frac{T_z - z \cdot x}{\cos \Theta_W}$, with $x = \sin^2 \Theta_W \approx 0.23$, where Θ_W is the Weinberg angle.

terms; these would otherwise lead to a complete breakdown of the theory. This contradicts sharply the observation, where most of the fermions and some of the bosons do have a mass. Looking at the masses of the four bosons of the electroweak sector, the discrepancy is especially striking; the need of an asymmetry in the context of QED is obvious here. The contradiction is that QED which is an incredibly exact theory², whose predictions accurately match the observations, is mathematically incapable of including one of the otherwise most important properties of the particles it describes (their mass).

It was however found that there could be a way of preserving the theory and its underlying symmetry as they are, by “outsourcing” the problem to a then necessary additional scalar field, the so-called Higgs field. This field would break the necessary symmetries spontaneously, whenever the particles would couple to it, thus gaining their mass. In this way both, the mass and the symmetry breaking, would not be part of the QED theory itself but a consequence of the interaction of the QED field with this Higgs field. This was a purely mathematical concept, which needed not necessarily be what happens in reality. However the consequence of this additional field would be that, just like the other fields, it could be stimulated to become excited, producing the real bosons of this field. Thus the detection of the Higgs boson was a major breakthrough, showing that this theory really describes the reality.

There is one other fundamental force which was left out until now: Gravity. It is however by far the weakest of all four forces, which is why it is completely disregarded by the Standard Model. There are however some very extreme cases where all four forces become important (e.g. neutron stars). There a complete description of the problem is currently not possible. This is the limit of today’s Standard Model. There are ambitions to have gravity included into the theory, thus implying the existence of another gauge boson, the graviton. [7, 8]

1.2.1 Comparison of the Fundamental Forces

The fundamental forces can be compared by considering the potential energy between two particles (see Chapter 10.1 for an explanation of the quantities shown). The

²QED and the general relativity theory are the two most accurate theories humanity has produced until now

electrical potential energy between a positron and an electron of charge e which is propagated by virtual photons is given by:

$$W_{el}(r) = -\frac{e^2}{4\pi\epsilon_0 r} = -\frac{\alpha}{r}, \quad \alpha = \frac{e^2}{4\pi\epsilon_0 \hbar c} \approx \frac{1}{137}$$

The gravitational potential energy between two electrons of mass m_e which is propagated by the hypothetical virtual graviton is given by:

$$W_{gr}(r) = -\frac{Gm_e^2}{r} = -\frac{\alpha_G}{r}, \quad \alpha_G = \frac{Gm_e^2}{\hbar c} \approx 2 \cdot 10^{-45}$$

The weak-force potential energy between any two particles with weak charge g which is propagated by the virtual W^\pm -meson of mass m_W is given by:

$$W_w(r) = -\frac{g^2}{r} \exp\left(-\frac{m_W r}{\hbar c}\right) = -\frac{\alpha_w}{r} \exp\left(-\frac{m_W r}{\hbar c}\right), \quad \alpha_w = \frac{g^2}{\hbar c} \approx 3 \cdot 10^{-2}$$

The strong-force potential energy between two quarks which is propagated by virtual gluons is given by:

$$W_s(r) = -\frac{4}{3} \frac{\alpha_s}{r} + kr, \quad \alpha_s \approx 1$$

It can be seen that the electrical and the gravitational potential energy have the same distance behaviour. The first term of the strong force is also equivalent, however there is this second linear term kr , called “string tension”. The naming comes from the image of a string of gluons spanned between the two quarks. For small r the behaviour is according to the first term while for large r the linear term takes over. The energy needed to separate two quarks increases until there has been so much energy put into the gluon string that a quark-antiquark pair is being generated, each bound to one of the initial quarks. This dynamic inseparability of quarks is called confinement and implies that multiple quarks are bound together in hadrons.

When two nucleons are next to each other, there is a reminiscent of the strong force which acts attractive, even though nucleons themselves are “white”. This is due to the fact that the net quarks of hadrons are surrounded by a sea of gluons and virtual quark-antiquark pairs. While the net colour is indeed white, the equilibrium is dynamic and results in a time-dependent polarization. The Yukawa force potential energy between any two nucleons is propagated by a virtual pion with mass m_π and is given by:

$$W_y(r) = -\frac{g_s^2}{r} \exp\left(-\frac{m_\pi r}{\hbar c}\right), \quad \alpha_s = \frac{g_s^2}{4\pi}$$

1.2.2 Asymptotic freedom

The different α 's in the expressions of the potential energy of forces are the coupling constants of the respective force. The difference in coupling strength has a big influence on the ease of the theoretical descriptions; e.g. QED calculations can generally be solved with a perturbation theoretical ansatz, because the interaction probability with an increasing number of photons is decreasing with a factor of $\alpha \approx 1/137$ for each additional photon. In QCD however the coupling strength α_s is

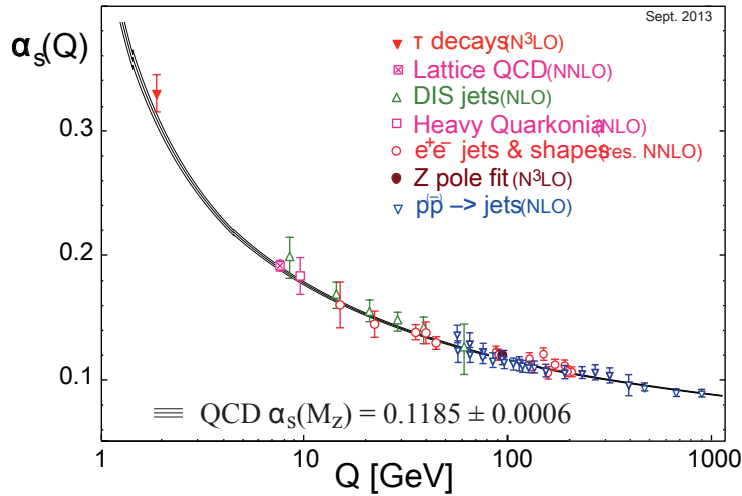


Figure 1.1: Summary of measurements of α_s as a function of the energy scale Q shows how the coupling decreases with increasing energy. [15]

of the order of 1, which means that the decrease in probability of coupling with an increasing number of gluons is nowhere near that small as for QED, thus a solution with perturbation theory is not generally possible. One of the situations where a solution is possible is in the environment which is being produced in heavy-ion collisions. This is the bigger picture of the scope of this analysis.

However, these coupling constants are not strictly constant. This fact is called “running coupling” and is characterized by the dependency on the transferred momentum Q which is proportional to the temperature³ and to the inverse of the distance ($T \propto Q \propto 1/r$). The vacuum around electrically charged particles polarizes, and shields the charge somewhat. The charge seems to diminish moving away from it, or equivalently, the coupling constant α increases with Q . The effect is different for colour charged particles, because now the mediating boson itself carries colour charge. This leads to the reversed behaviour called anti-shielding. Thus α_s is dependent on the energy scale $\Lambda_{QCD} \approx 200\text{MeV}$ and decreases with Q [15]:

$$\alpha_s(Q^2) = \frac{g_s^2(Q^2)}{4\pi} \approx \frac{1}{b_0 \ln(Q^2/\Lambda_{QCD}^2)}$$

Which means that towards large Q ($Q > \Lambda_{QCD}$) the strength of the strong force is being **asymptotically** reduced, the particles become **free** and the confinement is lifted (see also Figure 1.1). The 2004 Nobel Prize in Physics was awarded exactly for this discovery to J. D. Gross, F. Wilczek [16] and H. D. Politzer [17]. For the high Q region this means that for theoretical calculations the well-established perturbative ansatz can be used, just like in QED. Calculations in the non-perturbative regime can be performed with lattice-QCD, which decreases the infinite space-time degrees of freedom to a finite number [18–21].

The behaviour of $\alpha(Q)$ and $\alpha_s(Q)$ suggests that at some Q (or T) both are equal. This is the main building block of a grand unified theory (GUT) which would have

³in case a temperature can be defined

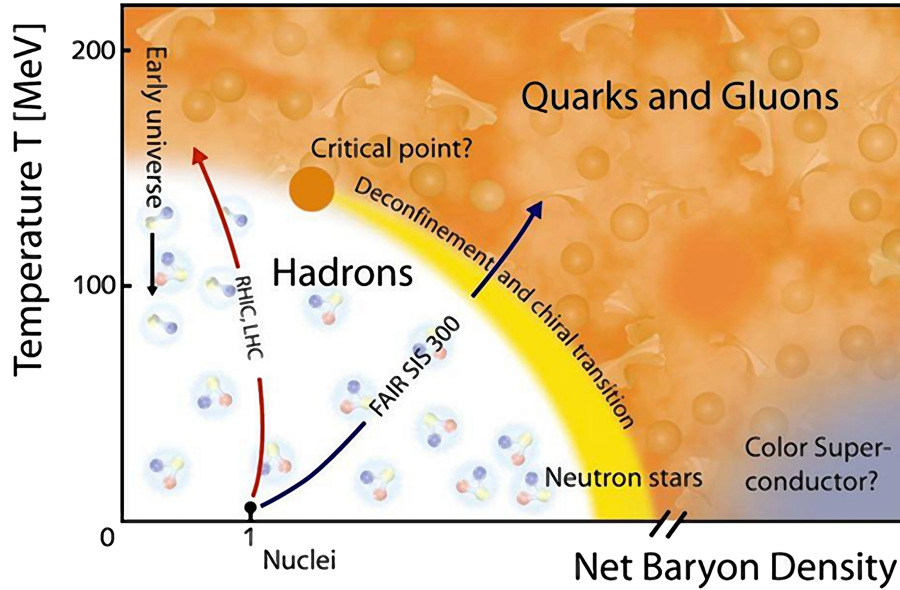


Figure 1.2: Phase diagram of quarks and gluons (Figure by the CBM Collaboration). In normal matter quarks and gluons are bound in hadrons, which compose the nuclei, at density 1 and temperature 0 ($300\text{ K} \approx 0.026\text{ eV}$). Also shown are the traces of the matter during heavy-ion collisions in current accelerators and the early universe. There the transition was about $1\ \mu\text{s}$ after the Big Bang. In the core of neutron stars quark-gluon plasma might exist at low temperatures due to their immense density. [25]

to show that from this point on not only the strengths are equal but also the physics of the electro-weak and strong force.

1.3 QCD Phase Diagram

In 1975 first theories emerged describing a state of matter where quarks and gluons are asymptotically free [22, 23]. At high energy densities, achieved either by high temperature or high compression, nuclear matter undergoes a phase transition lifting the confinement of the strongly interacting quarks and gluons, making them essentially free particles. In analogy to QED this phase was later called quark-gluon plasma (QGP) [24]. An illustration of our current understanding of the phase diagram of nuclear matter is depicted in Figure 1.2. There are three regions: ordinary hadronic matter, cold dense QGP and hot QGP. These are separated by phase transitions of unknown order at the transition temperature and transition density. There is also speculation about the existence of a critical point [26]. At low baryon density and temperature there is the normal hadronic matter with confined quarks and gluons. At small temperatures, around ten times the density of nuclei is needed to approach nucleons so much that their wave functions overlap, thus losing their identity and dissolving into a big nuclear lump containing free quarks and gluons [27–29]. The transition temperature needed for a low-baryon-density medium to reach the QGP phase is in the region of $150 - 200\text{ GeV}$ [30–32].

This state of matter is not only of theoretical relevance. Our universe is thought

to have been in this state right after the Big Bang, where only a low⁴ net baryon density was present but, due to the high temperatures, a high energy density was available. When the universe had expanded enough it cooled down below the critical temperature and quarks and gluons combined to hadrons. Also today QGP might naturally exist: The interior of neutron stars is thought to be a highly compressed, low-temperature QGP [33], while during the very extreme explosions of core-collapse supernovae there might be a brief period where a high-temperature QGP state is sustained [34, 35].

1.4 Ultra-relativistic nucleus-nucleus collisions

The very nature of the strong force to always bind together the colour charged partons is in the way to studying it. Thanks to the asymptotic freedom, ultra-relativistic heavy-ion collisions are a way to get large numbers of free partons, by crossing the phase transitions boundary towards the QGP phase. It has been expected for many years that a hot QGP phase can be produced by the conditions generated in heavy-ion collisions, through large momentum transfers and at small distances. Being propelled by the accelerator to great energies, the colliding nuclei produce high densities and high temperatures. The confinement is lifted, freeing quarks and gluons. An equilibrium is reached shortly thereafter, and a thermalized QGP phase of strongly coupled quarks and gluons is established. Due to its high pressure the resulting QGP is expanding into a fireball bringing quarks and gluons back to their confinement eventually. While this fireball expands and cools down, inelastic interactions between hadrons cease thus fixing the hadron composition of the medium. This stage is called “chemical freeze-out” and is followed by the “thermal freeze-out”, when the mean free path exceeds the system size and the elastic interactions also come to an end, fixing also the momentum distribution.

1.4.1 Initial Conditions

As for every other experiment, it is important to understand the initial conditions before undertaking the experiment itself. In contrast to fixed target experiments, the laboratory frame in collider experiments is identical to the centre-of-mass frame of the two colliding ions. In this frame the two colliding ions are Lorentz contracted along the transversal direction and their internal interactions are slowed down due to the time dilation.

The two nuclei collide with a central separation called **impact parameter**, which together with the beam axis defines the **reaction plane**. Small impact parameters characterize **central collisions**, while **peripheral collisions** are characterized by a large impact parameter. The more central a collision the more nucleons of one nucleus will be colliding head-on with nucleons from the other nucleus. Non-colliding nucleons are called **spectators**, while colliding nucleons are the **participants**. In a collision with enough participants, these will form the QGP while

⁴The low net baryon density is due to the fact that in the first instances our universe had as much matter as anti-matter. Later this balance lost its equilibrium probably due to the CP-violation in the weak interaction.

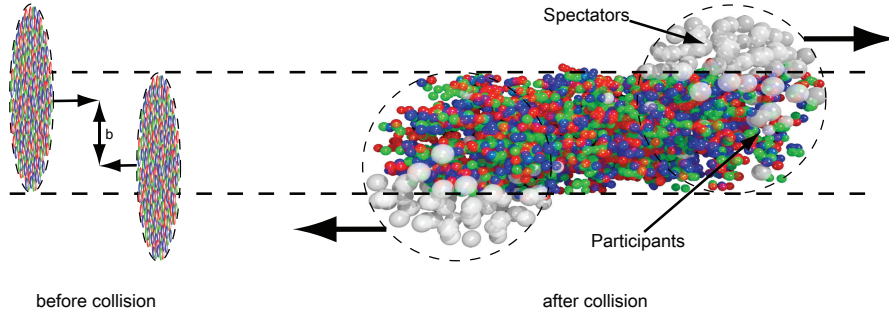


Figure 1.3: UrQMD Simulation of a heavy-ion collision: moments before and after. The incoming ions are Lorentz contracted. The impact parameter b describes the distance between the ion centres.

the spectators will continue their travel almost unaffected. Figure 1.3 shows an UrQMD simulation⁵ of the moments just before and after the collision.

There are many models on the market for the initial conditions. A very simple way to characterize the initial geometry is the Monte Carlo Glauber model.

Monte Carlo Glauber model

In this two-dimensional statistical model, the nucleons are placed inside the nuclei according to the Woods-Saxon probability density, which for small nuclei is similar to a Gaussian distribution. Each nucleon is described by a circle of an area equal to its inelastic cross section $\sigma_{pp,inel}$, which represents the probability of having an inelastic collision in a proton-proton collision. This has to be priorly determined in separate nucleon-nucleon collisions.

A collision of two such nuclei is shown in Figure 1.4. The two nuclei are overlaid with the impact parameter b being the distance of the centres. Overlapping nucleons of the two nuclei produce a **binary collision**. The coordinate system shown is aligned to the **participant plane**, which results from a linear fit of the participants. Due to fluctuations the participant plane is not identical to the reaction plane Ψ_{RP} . The non-spherical, **almond shape** of the participants is characterized by a non-zero eccentricity. As explained later in Chapter 3 this spatial anisotropy leads to anisotropies in other variables. [37]

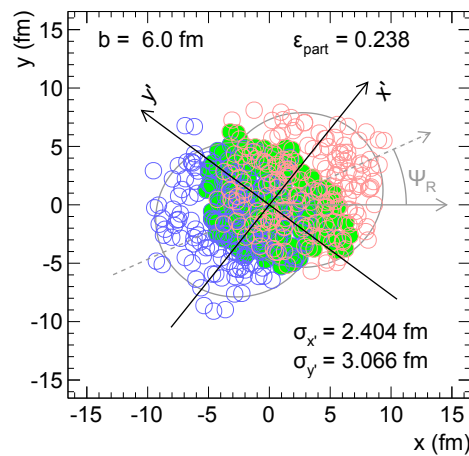


Figure 1.4: Glauber model used for calculating the number of binary collisions. [36]

⁵<http://urqmd.org/>

Parton Distribution Functions

In a heavy-ion collision, there are not only collisions of the participating nucleons, but in fact there are also collisions on the partonic level of the nucleons. Thus, apart from the geometrical configuration of the nucleons, it is important to describe the momentum distribution of all the parton species inside the nucleon. This is done by so-called **parton distribution functions** (PDFs). Typically PDFs are measured by deep-inelastic scatterings experiments. [38–40]

Nuclei are, however, a bound state of multiple nucleons. This can lead to departures of the parton distribution compared to the free-nucleon PDFs. Effects due to this difference are called **initial state effects**. Depending on the momentum transfer and the parton momentum there can be effects like a depletion of the quark density (called shadowing), or an enhancement (called anti-shadowing). This is a field of study on its own and can have a significant influence on the measurements. Corrections to the free parton distribution functions due to the binding of nucleons in a nucleus are called nuclear PDFs (nPDFs). [41–43]

1.4.2 Formation of the QGP

Motivated by the high number and high density of participants, and due to the huge energy density involved, it is expected that a QGP phase is established, dissolving the participant nucleons.

In this work, the hydrodynamic picture will be used. Thus, instead of following the evolution of every single parton, as done in so-called transport models, the bulk of the partons are treated as a fluid analysing their collective behaviour. For more in the subject see Chapter 3.

Embedded into this fluid there can be products of exceptionally hard scatterings of the initial partons. These can be heavy quarks or high-momentum light partons. The formation probability and the momentum of these hard scattering products are given by the PDFs of the two partons scattering, and the cross section of the production process. When the initial scattering is hard, there is a high momentum transfer Q , and the production cross sections can be computed perturbatively.

1.4.3 Hadronization

The expansion of the QGP quickly lowers its temperature. At the phase boundary, the colour charged partons can no longer behave as free particles, but have to hadronize into colour neutral hadrons. Thus, at the phase transition, the relevant degrees of freedom of the system change from partonic to a hadronic nature.

The heavy quarks and high-momentum light quarks, which were produced in hard partonic scatterings, hadronize respectively into heavy-flavour hadrons and jets of light hadrons. The momenta of these with respect to the parton momentum are given by the fragmentation functions (FF), which can be measured in e^+e^- reactions. Because the initial hard scattering is on a much faster time scale than the time dilated initial configuration and the later fragmentation, the production and fragmentation processes can be viewed as independent. This effect is called factorization, because the total production probabilities factorize under these assumptions.

Thus, the cross section of producing the hadron h in the fragmentation of the parton c , which is the product of a hard scattering of the partons a and b of the nucleons A and B , is given by:

$$d\sigma_{AB \rightarrow h}^{hard} = \text{PDF}_{A,a} \left(\frac{p_a}{p_A}, Q^2 \right) \cdot \text{PDF}_{B,b} \left(\frac{p_b}{p_B}, Q^2 \right) \cdot d\sigma_{ab \rightarrow c}^{hard} \left(\frac{p_a}{p_A}, \frac{p_b}{p_B}, Q^2 \right) \cdot \text{FF}_{c \rightarrow h} \left(\frac{p_h}{p_c}, Q^2 \right)$$

1.4.4 Signatures of the QGP

Due to the very short time the QGP state is sustained, and the confinement which permits only colour neutral hadrons to be the final states that can be observed, it is not straight forward to study the QGP. Thus, a series of different observables and signatures has to be considered. All observables are monitored depending on the centrality, as the formation of the QGP should be highly dependent on the number of binary collisions. Additionally, the observables should be compared between collisions of pp, pA and AA⁶ at comparable collision energy per nucleon to verify the influence of the initial state effects.

Because of the strong interaction of the partons inside a QGP, there is the anticipation that there are modifications of the observables from expectations without a medium. The expectations for heavy-ion collisions without a QGP, can be directly deduced from proton-proton collisions, with a numerical scaling to the number of binary collisions inside the heavy-ion collision. Departures from these expectations can be due to either the aforementioned initial state effects or from in-medium modifications of the observables, called **final state effects**. Because both, initial and final state effects currently represent very active fields of study, it is often not trivial to disentangle those two.

Kinematic Probes

The global experimental observables *average transverse momentum* $\langle p_T \rangle$, *hadron rapidity distribution* dN/dy and *transverse energy distribution* dE_T/dy are directly connected to the thermodynamic characteristics temperature, entropy density and energy density of the fireball, which forms at the collision. At the phase transition towards a QGP a sudden rise of the degrees of freedom should be visible in the change of energy density and entropy as function of temperature.

Jet Quenching

When two partons hit head-on (interact via a single gluon exchange), they deflect each other back-to-back with high virtuality. The virtuality is reduced by subsequent gluon radiation or quark-antiquark production. Due to the confinement this collimated spray of partons hadronizes and forms a jet. In case a QGP forms, the partons should experience collisional and radiative energy loss due to the strong interaction with the colour-charged medium. This should alter the jet structure [44], and multi-particle correlations [45], as well as introduce a path-length and momentum dependent suppression of hadrons.

⁶Whereas “pp” mean proton-proton collision and “AA” heavy nuclei collisions, in our case lead

Strangeness Production

Due to strangeness conservation, strange particles can only be produced in pairs. The threshold energy needed is given by the mass of the produced pair. However, inside a QGP where the confinement is lifted, strange quarks pairs can be produced directly, lowering the threshold considerably [46]. Thus, an enhancement of multi-strange hyperons is expected.

Quarkonium Production

While initially thought as an observable directly related to deconfinement in the fireball, recent work shows that there are various mechanisms altering the production of charmonium and bottomium states: While the unbound colour charge of the medium provides a Debye-like screening, resulting in a suppression of individual states depending on the distance of the quark pairs and the temperature of the medium [47], additional quarkonia could be formed via statistical hadronization at the phase boundary [48, 49], or, earlier, via coalescence in the QGP [50].

Electromagnetic Probes

Leptons and photons are probes for the earliest moments of the interaction. Since they are not influenced by the strong force they can leave the fireball much less obstructed than hadrons. Thus, information about the characteristics of the medium before the freeze-out can be gained.

Collective Flow

As shown later in Chapter 3, it is possible to treat the QGP by hydrodynamical models, where thermodynamic quantities like temperature, pressure and viscosity lead to collective movements of the particles.

1.5 Units

The units used throughout calculations are mostly arbitrary, as long as they are used consistently. Historical reasons and convenience are the important factors when considering unit systems. Typically for day-to-day business the International System of Units “SI” is most widely used. Historically its origins date back to the French revolution, where the revolutionary vibe not only enforced radical changes in the political system but also sought to abolish everything which was felt to be only remotely connected to it. Base of the system are seven units⁷: second, metre, kilogram, ampere, kelvin, mole, and candela [53]. This system is convenient for common day-to-day use: Usual sizes are of the orders of the meter, and usual weights are of the order of a kilogram.

⁷While the upcoming redefinition of the SI will significantly change the definitions of the base units, the base units themselves will be the same. The future definition of the SI which was recommended by the International Committee for Weights and Measures (CIPM) will most likely be approved at the 26th General Conference on Weights and Measures (CGPM) expected in 2018. [51, 52]

	Unit	Value of one unit in SI
energy	eV	$1.6022 \cdot 10^{-19} \frac{\text{kg}\cdot\text{m}^2}{\text{s}^2}$
speed	c	$299792.458 \frac{\text{m}}{\text{s}}$
length	fm	10^{-15} m
momentum	eV/c	$5.3442 \cdot 10^{-25} \frac{\text{kg}\cdot\text{m}}{\text{s}}$
mass	eV/c^2	$1.7827 \cdot 10^{-30} \text{ kg}$
temperature	eV/k_B	11600 K
time	fm/c	$3.3356 \cdot 10^{-24} \text{ s}$

Table 1.3: Unit system used in high energy physics

In high-energy physics however these units are inconvenient. Instead the energy scale used is based on the electron volt, which is the amount of energy an electron has after being accelerated by an electric potential of 1 Volt. The length-scale used is based on the femtometre, which is approximately the size of a nucleon. The speed is defined relative to the speed of light and the time scale is relative to the time light needs to cross a femtometre. The units used in this work are given in Table 1.3.

2 Relativistic Kinematics

Due to the high energies the incoming projectiles are accelerated to, not only these are moving at relativistic speed, but also the particles created in the collisions. Thus, a very brief introduction to special relativity shall follow. This chapter introduces the mathematical framework of the theory of special relativity needed for this work, which was first proposed by Albert Einstein in a series of articles [54–58]. From this some important relations are derived and additional important definitions mentioned.

2.1 Minkowski Space

The mathematical arena of Einsteins special relativity is the Minkowski space, which is a four-dimensional vector space with the following inner product as its structure:

$$\mathbf{a} \cdot \mathbf{b} = \langle a, b \rangle := a_0 b_0 - a_1 b_1 - a_2 b_2 - a_3 b_3 = a_0 b_0 - \vec{a} \cdot \vec{b} \quad (2.1)$$

The elements of this inner product space are four-dimensional vectors, called 4-vectors, which are composed of the time as the zeroth component and with the remaining three components taken from the classical three-dimensional space vectors. Bold variables shell represent 4-vectors, italic variables with indices represent components and variables with a vector arrow on top are the Euclidean 3-vectors of the space dimensions. For the definition of the inner product the signature $(+, -, -, -)$ was used and not the equally possible $(-, +, +, +)$. Because of the changing signs in this definition of the scalar product, the structure of this vector space is different from a four-dimensional Euclidean space, where the signature is exclusively positive (or negative).

A side effect of these mixed signs is that it is not possible to globally define an orthonormal basis common to all observers. Thus, in order to cope with skewed coordinate systems it is necessary to borrow from differential geometry, just like it is done in general relativity. Let there be two ways of defining components of a vector, one with an upper index and one with a lower index:

$$\mathbf{a} := \{a^\mu\} = \begin{pmatrix} a^0 \\ a^1 \\ a^2 \\ a^3 \end{pmatrix} \quad \{a_\mu\} = \begin{pmatrix} a_0 \\ a_1 \\ a_2 \\ a_3 \end{pmatrix}$$

Components with lower index are related to components with upper index by the definition:

$$a_0 := a^0, \quad a_i := -a^i, \quad i \in \{1, 2, 3\} \quad (2.2)$$

Components with upper index are called contravariant, and components with lower index are called covariant. The names are a reminder that the mathematical basis of the Minkowski space is multilinear algebra and the covariant description is dual to the contravariant. The inner product can thus be rewritten into a form which

looks more natural, hiding the minus signs:

$$\mathbf{a} \cdot \mathbf{b} = a_0 b^0 + a_1 b^1 + a_2 b^2 + a_3 b^3 = \sum_{\mu=0}^3 a_{\mu} b^{\mu} = \sum_{\mu=0}^3 a^{\mu} b_{\mu} =: a^{\mu} b_{\mu} = a_{\mu} b^{\mu}$$

Using the Einstein notation the summation sign over the common index will always be dropped, taking it as implicit over the necessary variables.

By introducing the metric tensor

$$g_{\mu\nu} := \text{diag}(1, -1, -1, -1) = \begin{pmatrix} 1 & 0 & 0 & 0 \\ 0 & -1 & 0 & 0 \\ 0 & 0 & -1 & 0 \\ 0 & 0 & 0 & -1 \end{pmatrix} = g^{\mu\nu}$$

the inner product can also be written as:

$$a_{\nu} = g_{\mu\nu} a^{\mu}$$

$$a^{\nu} = g^{\mu\nu} a_{\mu}$$

$$\mathbf{a} \cdot \mathbf{b} = a_{\mu} b^{\mu} = g_{\mu\nu} a^{\nu} b^{\mu} = g_{\mu\nu} a^{\nu} g^{\mu\sigma} b_{\sigma} = g_{\mu\nu} g^{\mu\sigma} a^{\nu} b_{\sigma} = a^{\nu} b_{\nu}$$

2.2 Lorentz Transformation

Having defined the mathematical structure, it can now be filled with life inserting the physics. The coordinates x , y and z are used as indices for classical 3-vectors and 0, 1, 2, and 3 for relativistic 4-vectors. Using the following definitions

$$\beta = \frac{v}{c}, \quad \gamma = \frac{1}{\sqrt{1 - \beta^2}}$$

we can introduce the 4-vectors of space-time, velocity and energy-momentum:

$$\mathbf{x} = \begin{pmatrix} x^0 \\ x^1 \\ x^2 \\ x^3 \end{pmatrix} = \begin{pmatrix} ct \\ x \\ y \\ z \end{pmatrix} \quad \mathbf{v} = \begin{pmatrix} v^0 \\ v^1 \\ v^2 \\ v^3 \end{pmatrix} = \begin{pmatrix} \gamma c \\ \gamma v_x \\ \gamma v_y \\ \gamma v_z \end{pmatrix} \quad \mathbf{p} = m_0 \mathbf{v} = \begin{pmatrix} \gamma m_0 c \\ \gamma m_0 v_x \\ \gamma m_0 v_y \\ \gamma m_0 v_z \end{pmatrix} = \begin{pmatrix} E/c \\ \gamma p_x \\ \gamma p_y \\ \gamma p_z \end{pmatrix} = \begin{pmatrix} p^0 \\ p^1 \\ p^2 \\ p^3 \end{pmatrix}$$

These vectors are measured relative to a specific frame. Going to a different frame which moves relative to the initial frame, is done by means of the Lorentz transformation. Any Lorentz transformation Λ can be associated with a transformation matrix $\mathbf{\Lambda} := \{\Lambda^{\mu}_{\nu}\}$. The vectors measured relative to this new frame are then:

$$\mathbf{a}' = \mathbf{\Lambda} \mathbf{a}, \quad a'^{\mu} = \Lambda^{\mu}_{\nu} a^{\nu}$$

The defining property of the Lorentz transformation can be expressed as a requirement on $\mathbf{\Lambda}$:

$$g_{\mu\nu} \Lambda^{\mu}_{\alpha} \Lambda^{\nu}_{\beta} = g_{\alpha\beta} \quad (2.3)$$

Any such transformation preserves the inner product of the underlying Minkowski space (Equation 2.1) by construction:

$$\mathbf{a}' \cdot \mathbf{b}' = a'_\nu b'^\nu = g_{\mu\nu} a'^\mu b'^\nu = g_{\mu\nu} \Lambda^\mu{}_\alpha \Lambda^\nu{}_\beta a^\alpha b^\beta = g_{\alpha\beta} a^\alpha b^\beta = \mathbf{a} \cdot \mathbf{b} \quad (2.4)$$

Inner products can thus be calculated in the most convenient frame, the results are universal. More technically, the symmetry constraints are encapsulated by the term $\text{SO}(1,3)$ ⁸. The situation is very similar to four-dimensional rotations, which are termed $\text{SO}(4)$ and are preserving the usual Euclidean inner product and where the defining property (equivalent to Equation 2.3) of a rotation matrix R can be expressed as $R^{-1}R = \mathbb{1}$.

Given a transformation Λ , the form of its inverse can be derived from Equation 2.3:

$$(\Lambda^{-1})^\mu{}_\nu = (\Lambda^T)_\mu{}^\nu = \Lambda_\nu{}^\mu = g_{\alpha\nu} g^{\beta\mu} \Lambda^\alpha{}_\beta$$

Which means:

$$\Lambda = \begin{pmatrix} \Lambda^0_0 & \Lambda^0_1 & \Lambda^0_2 & \Lambda^0_3 \\ \Lambda^1_0 & \Lambda^1_1 & \Lambda^1_2 & \Lambda^1_3 \\ \Lambda^2_0 & \Lambda^2_1 & \Lambda^2_2 & \Lambda^2_3 \\ \Lambda^3_0 & \Lambda^3_1 & \Lambda^3_2 & \Lambda^3_3 \end{pmatrix} \Rightarrow \Lambda^{-1} = \begin{pmatrix} \Lambda^0_0 & -\Lambda^1_0 & -\Lambda^2_0 & -\Lambda^3_0 \\ -\Lambda^0_1 & \Lambda^1_1 & \Lambda^2_1 & \Lambda^3_1 \\ -\Lambda^0_2 & \Lambda^1_2 & \Lambda^2_2 & \Lambda^3_2 \\ -\Lambda^0_3 & \Lambda^1_3 & \Lambda^2_3 & \Lambda^3_3 \end{pmatrix}$$

Of all possible transformations, one is especially important: the Lorentz boost. It is the transformation between frames of the same orientation and same acceleration but at different relative speeds. For a relative movement of the frames in arbitrary direction with velocity $\vec{\beta}$ we can introduce the Lorentz matrix:

$$\Lambda = \begin{pmatrix} \gamma & \gamma\beta_x & \gamma\beta_y & \gamma\beta_z \\ \gamma\beta_x & 1 + \lambda\beta_x^2 & \lambda\beta_x\beta_y & \lambda\beta_x\beta_z \\ \gamma\beta_y & \lambda\beta_y\beta_x & 1 + \lambda\beta_y^2 & \lambda\beta_y\beta_z \\ \gamma\beta_z & \lambda\beta_z\beta_x & \lambda\beta_z\beta_y & 1 + \lambda\beta_z^2 \end{pmatrix}, \lambda = \frac{\gamma - 1}{\beta^2} \quad (2.5)$$

2.3 Important Relations

With the definitions above some important relations can be found. Throughout this work the convention $c = 1$ will be used.

The velocity of a particle in its rest frame ($\beta = 0, \gamma = 1$) is $\mathbf{v} = (1, 0, 0, 0)$, while its momentum is $\mathbf{p} = (m_0, 0, 0, 0)$.

$$\mathbf{v} \cdot \mathbf{v} = v^\mu v_\mu = v^\mu g_{\mu\nu} v^\nu = v_0^2 - v_1^2 - v_2^2 - v_3^2 = v_0^2 - \vec{v}^2 = 1$$

$$\mathbf{p} \cdot \mathbf{p} = p^\mu p_\mu = p^\mu g_{\mu\nu} p^\nu = p_0^2 - p_1^2 - p_2^2 - p_3^2 = p_0^2 - \vec{p}^2 = m_0^2 \quad (2.6)$$

As shown in Equation 2.4 these results are independent of the frame. The second identity can be rearranged to:

⁸indicating that the transformations are continuous (S) (determinant is positive), orthogonal (O) (unit determinant) and are conserving the inner product of the underlying vector space with an indefinite signature of $(+, -, -, -)$

$$\begin{aligned}
p_0^2 - p_1^2 - p_2^2 - p_3^2 &= p_0^2 - \vec{p}^2 \\
\Leftrightarrow m_0^2 &= E^2 - p^2 \\
\Rightarrow E^2 &= p^2 + m^2
\end{aligned} \tag{2.7}$$

This is the energy-momentum relation which is of utmost importance in high-energy physics. In multi-particle systems, the former expression defines the invariant mass W :

$$W^2 = \left(\sum E\right)^2 - \left(\sum p\right)^2 \tag{2.8}$$

In case that all particles are decay products of some decayed mother particle it holds that the invariant mass equals the mass of the decayed particle: $W = m_0$.

In our context, energy E always means total energy. Subtracting the rest mass, we get the kinetic energy.

$$E_{kin} = E - m = \sqrt{p^2 + m^2} - m = m(\gamma - 1) \tag{2.9}$$

Furthermore it is of use to realize that:

$$\frac{p}{E} = \beta, \quad \frac{E}{m} = \gamma$$

Another useful definition in the framework of special relativity is the rapidity. It is an alternative measure to speed, preserving the additivity known from classical physics.

$$y = \frac{1}{2} \ln \left(\frac{E + p}{E - p} \right) = \tanh^{-1} \left(\frac{p}{E} \right) = \tanh^{-1}(\beta)$$

However, in our case we are only interested in the projection along the beam (see also Chapter 4.2.1 for an explanation of the coordinate system used):

$$y = \frac{1}{2} \ln \left(\frac{E + p_z}{E - p_z} \right) = \tanh^{-1} \left(\frac{p_z}{E} \right) \tag{2.10}$$

In experimental physics another more convenient measure is used, the pseudorapidity. In contrast to rapidity, it has the advantage of being mass independent and can thus be used as an alternative to the polar angle θ . For highly relativistic particles ($p \gg m$) it is identical to rapidity. In the limit of $m \rightarrow 0$ Equation 2.7 yields $E = p$ and Equation 2.10 can be transformed to:

$$\eta = \frac{1}{2} \ln \left(\frac{p + p_z}{p - p_z} \right) = \tanh^{-1} \left(\frac{p_z}{p} \right) = -\ln \left[\tan \left(\frac{\theta}{2} \right) \right] \tag{2.11}$$

This definition is useful because particle production upon a collision is usually given in terms of rapidity, while in high-energy experiments rapidity is approximately equivalent to the pseudorapidity which is just a geometrical measure.

The projection of the produced particle's momentum onto the transverse plane is another very important measure.

$$p_T = \sqrt{p_x^2 + p_y^2} \tag{2.12}$$

The more energy of the incoming projectiles is converted in the collision, the more particles are generated with transverse momentum. Often we will restrict ourselves to statements which are true only at vanishing longitudinal momentum ($p_z = 0$), describing what happens in the transverse plane at $\eta = 0$. In this context we can also define the projection of the total energy onto the transverse plane, it is called transverse mass:

$$E = \sqrt{m^2 + p^2} \xrightarrow{p=p_T} \sqrt{m^2 + p_T^2} =: m_T \quad (2.13)$$

Similarly we can define the transverse kinetic energy:

$$E_{kin} = E - m = \sqrt{m_0^2 + p^2} - m \xrightarrow{p=p_T} \sqrt{m_0^2 + p_T^2} - m = m_T - m := KE_T \quad (2.14)$$

2.4 Invariant Cross Sections

In high-energy physics, measurements are not based on single occurrences but on statistical repetition of the interesting events. The rate at which these events occur is given by the product of the luminosity \mathcal{L} of the beam (closely related its intensity) and the cross section σ of the process.

$$\frac{dN}{dt} = \mathcal{L} \cdot \sigma$$

The total amount of events is simply given by the integral over time; the longer we record, the more events we will have recorded:

$$N = \int \mathcal{L} \cdot \sigma dt = \sigma \int \mathcal{L} dt$$

The luminosity is given by the experimental setup and is unrelated to the physical cross section, which is what we try to measure (see also Chapter 4 and Equation 4.1). Thus for a given data sample N and σ are different by just a constant. Often, it is important to not only measure the total cross section, but to identify how it depends on other variables. We will typically evaluate our results momentum-dependent:

$$\frac{d^3\sigma}{dp^3} \propto \frac{d^3N}{dp^3}$$

While the cross section is a Lorentz-invariant quantity the differential cross-section as introduced above is not. To achieve this, a multiplication with the energy is needed:

$$E \frac{d^3\sigma}{dp^3} \propto E \frac{d^3N}{dp^3}$$

Depending on the situation other coordinate systems may be preferred:

$$\frac{d^3\sigma}{dp^3} = \frac{d^3\sigma}{dp_x dp_y dp_z} = \frac{d^3\sigma}{p_T dp_T d\varphi dp_z} = \frac{d^2\sigma}{2\pi p_T dp_T dp_z} = \frac{d^2\sigma}{2\pi E p_T dp_T dy}$$

3 Hydrodynamics of the QGP

Useful properties of the produced QGP and of the particles radiated from it will be derived in this chapter. First it will be shown that it is not unreasonable to assume that hydrodynamics can be applied to the system, then, after laying out the framework of the calculations, all important relations will emerge from very few and basic principles. This chapter was strongly influenced by the following publications: [59–63].

For a sound hydrodynamic description, it is necessary that thermodynamic variables such as temperature and pressure can be defined. The number of particles in a QGP produced by the two colliding $^{208}\text{Pb}^{82+}$ ions is certainly high enough for a thermodynamic description. However, the QGP is expanding at a relativistic pace. Such a system can certainly not be in a global equilibrium, which would be necessary for a standard thermodynamic description. With global thermodynamic equilibrium violated, the best we can hope for, is that at least parts of the system are in a local equilibrium.

The applicability of hydrodynamics is strongly related to the Knudsen number:

$$Kn = \frac{\lambda}{R}$$

In a fluid the mean free path λ must be small compared to the size of the system R , implying $Kn \ll 1$. Measurements at RHIC and estimations for the LHC show that during the high temperature phase it is very probable that the system is at least at some point in time in local thermodynamical equilibrium and such that at least there hydrodynamics is applicable [60, 64].

3.1 Thermodynamic Definitions

In the following a small volume element of the QGP shall be described as being in local thermodynamic equilibrium where the following properties are regarded as well defined:

- Volume V
- Pressure P
- Internal energy U
- Baryon number N
- Entropy S
- Baryon chemical potential μ
- Energy density $\epsilon = U/V$
- Entropy density $s = S/V$
- Baryon density $n = N/V$

The fundamental thermodynamic relation describes the change in internal energy expressed in terms of changes in the variables S , V and N :

$$dU = TdS - PdV + \mu dN \quad (3.1)$$

The equation holds for all systems in equilibrium. The transition to relativistic thermodynamics is done by recognizing that N is not simply the number of particles, since this is not conserved in relativistic systems. The system can however have other conserved quantities, which in our case is the baryon number.

The internal energy is a homogeneous function of the first degree:

$$U(\alpha S, \alpha V, \alpha N) = \alpha U(S, V, N)$$

Taking this and the previous expression (Equation 3.1) together with Euler's theorem on homogeneous functions it follows:

$$U = TS - PV + \mu N$$

For the fluid cell we want to study this translates to:

$$\epsilon = Ts - P + \mu n \quad (3.2)$$

3.2 Assumptions

The hydrodynamics of a QGP fluid cell will be derived from the axiomatic assumption that it almost⁹ reaches local thermodynamic equilibrium in its rest frame¹⁰, describing a perfect fluid. Thus, the fluid, isotropically distributed in this cell, is inviscid and neither has shear stresses nor is it heat conductive.

We will further assume that the fluid is baryonless ($n = 0$). This assumption is not as absurd as it sounds. Although there are indeed nucleons hitting in a collision, meaning that there is net baryon number, there is also the huge collision energy¹¹. Thus there are so many quarks and anti-quarks pairs being generated, that the net baryon number density is very small.

The entropy of an inviscid fluid is conserved throughout its evolution. With both S and N conserved, the fluid cell will undergo an isentropic evolution. Under these assumptions and with $U = \epsilon V$ the fundamental thermodynamic relation (Equation 3.1) simplifies to:

$$\begin{aligned} dU &= d(\epsilon V) = \epsilon dV + V d\epsilon = -PdV \\ \Leftrightarrow \quad \frac{d\epsilon}{\epsilon - P} &= -\frac{dV}{V} \end{aligned}$$

With $s = S/V$ it follows:

$$\begin{aligned} \frac{ds}{dV} &= \frac{d}{dV} \left(\frac{S}{V} \right) = -\frac{S}{V^2} = -\frac{s}{V} \\ \Leftrightarrow \quad d(\ln s) &= \frac{ds}{s} = -\frac{dV}{V} = \frac{d\epsilon}{\epsilon - P} \end{aligned} \quad (3.3)$$

⁹We will in fact let some place for small departures from perfect equilibrium.

¹⁰the frame in which its net momentum vanishes

¹¹2.76 TeV per nucleon, each weighing 940 MeV

3.3 Relativistic Hydrodynamics

The energy and momentum of a such a fluid cell in its rest frame is given by the energy-momentum tensor T_{rf} .

$$\mathbf{T}_{rf} = \begin{pmatrix} \epsilon & 0 & 0 & 0 \\ 0 & P & 0 & 0 \\ 0 & 0 & P & 0 \\ 0 & 0 & 0 & P \end{pmatrix}$$

The local energy density ϵ is related to the local pressure P by the equation of state. The equation of state describes how the fluid behaves, as well as its phase diagram. So in the language of hydrodynamics, this is in fact what we are actually after.

With the Lorentz transformation matrix Λ we can change the energy-momentum tensor T to a moving frame. Since it is enough to have T expressed to the first order in the fluid velocity, the matrix of the Lorentz transformation (Equation 2.5) can be simplified to:

$$\Lambda = \begin{pmatrix} \gamma & \gamma\beta_x & \gamma\beta_y & \gamma\beta_z \\ \gamma\beta_x & 1 + \lambda\beta_x^2 & \lambda\beta_x\beta_y & \lambda\beta_x\beta_z \\ \gamma\beta_y & \lambda\beta_y\beta_x & 1 + \lambda\beta_y^2 & \lambda\beta_y\beta_z \\ \gamma\beta_z & \lambda\beta_z\beta_x & \lambda\beta_z\beta_y & 1 + \lambda\beta_z^2 \end{pmatrix} \approx \begin{pmatrix} 1 & \beta_x & \beta_y & \beta_z \\ \beta_x & 1 & 0 & 0 \\ \beta_y & 0 & 1 & 0 \\ \beta_z & 0 & 0 & 1 \end{pmatrix}, \lambda = \frac{\gamma - 1}{\beta^2}$$

In its matrix form the Lorentz transformed energy-momentum tensor reads:

$$\mathbf{T} = \Lambda \mathbf{T}_{rf} \Lambda^T = \begin{pmatrix} \epsilon & (\epsilon + p)\beta_x & (\epsilon + p)\beta_y & (\epsilon + p)\beta_z \\ (\epsilon + p)\beta_x & P & 0 & 0 \\ (\epsilon + p)\beta_y & 0 & P & 0 \\ (\epsilon + p)\beta_z & 0 & 0 & P \end{pmatrix}$$

In the typical relativistic representation the elements of matrix T are called $T^{\mu\nu}$ and can be written using the Einstein notation:

$$T^{\mu\nu} = (\epsilon + p)u^\mu u^\nu - P g^{\mu\nu} \quad (3.4)$$

where $g^{\mu\nu} = \text{diag}(1, -1, -1, -1)$ is the metric tensor and \mathbf{u} is the 4-velocity with components u^μ .

$$\mathbf{u} = \begin{pmatrix} \gamma \\ \gamma\beta_x \\ \gamma\beta_y \\ \gamma\beta_z \end{pmatrix}$$

Energy and momentum conservation is generally expressed by the vanishing derivatives of $T^{\mu\nu}$, the so-called continuity equation:

$$\partial_\mu T^{\mu\nu} = 0$$

Inserting here the above expression for $T^{\mu\nu}$ (Equation 3.4) the following four equations emerge:

$$\begin{aligned}\frac{\partial \epsilon}{\partial t} + \vec{\nabla} \cdot ((\epsilon + P)\vec{u}) &= 0 \\ \frac{\partial}{\partial t}((\epsilon + P)\vec{u}) + \vec{\nabla} P &= \vec{0}\end{aligned}\quad (3.5)$$

This, together with the equation of state and the continuity equations for all other conserved quantities represents a closed system of equations. To study just the propagation of small disturbances in the fluid, the energy density and pressure can be rewritten as a constant with small perturbations $\delta\epsilon$ and δP respectively:

$$\begin{aligned}\epsilon &= \epsilon_0 + \delta\epsilon \\ P &= P_0 + \delta P\end{aligned}\quad (3.6)$$

Inserting this into the previous expression (Equation 3.5) and linearising we finally get:

$$\begin{aligned}\frac{\partial(\delta\epsilon)}{\partial t} + (\epsilon_0 + P_0)\vec{\nabla} \cdot \vec{u} &= 0 \quad \Leftrightarrow \quad -\frac{\partial(\delta\epsilon)}{\partial t} = (\epsilon_0 + P_0)\vec{\nabla} \cdot \vec{u} \\ (\epsilon_0 + P_0)\frac{\partial\vec{u}}{\partial t} + \vec{\nabla}(\delta P) &= \vec{0} \quad \Leftrightarrow \quad (\epsilon_0 + P_0)\frac{\partial\vec{u}}{\partial t} = -\vec{\nabla}(\delta P)\end{aligned}$$

The first equation is the energy conservation: if the system volume increases ($\vec{\nabla} \cdot \vec{u} > 0$), the energy density decreases ($-\partial(\delta\epsilon)/\partial t < 0$). The second equation is Newton's second law: the system inertia ($\epsilon_0 + P_0$) times its acceleration ($\partial\vec{u}/\partial t$) equals to the force on the volume ($-\vec{\nabla}(\delta P)$). The force pushes the fluid towards lower pressure. In our case of a QGP in vacuum, the QGP will thus expand.

3.4 Transverse Expansion

To analyse the expansion we go back to the vector part of the continuity equation (Equation 3.5) and assume that the expansion builds up with vanishing initial value ($\vec{u}(t=0) = \vec{0}$).

$$\begin{aligned}\frac{\partial}{\partial t}((\epsilon + P)\vec{u}) &= -\vec{\nabla} P \\ \Leftrightarrow \quad \vec{u}\cancel{\frac{\partial}{\partial t}} + \epsilon\frac{\partial\vec{u}}{\partial t} + \vec{u}\cancel{\frac{\partial P}{\partial t}} + P\frac{\partial\vec{u}}{\partial t} &= -\vec{\nabla} P \\ \Leftrightarrow \quad \frac{\partial\vec{u}}{\partial t} &= -\frac{1}{\epsilon + P}\vec{\nabla} P\end{aligned}$$

Together with Equation 3.3 and the velocity of sound $c_s = \sqrt{(\partial P/\partial\epsilon)}$ we thus get the acceleration in the two transverse directions:

$$\begin{aligned}\frac{\partial u_x}{\partial t} &= -\frac{1}{\epsilon + P}\frac{\partial P}{\partial x} = -c_s^2\frac{\partial(\ln s)}{\partial x} \\ \frac{\partial u_y}{\partial t} &= -\frac{1}{\epsilon + P}\frac{\partial P}{\partial y} = -c_s^2\frac{\partial(\ln s)}{\partial y}\end{aligned}\quad (3.7)$$

We insert a distribution for s matching the density profile of the collision, which we take as a Gaussian for simplicity:

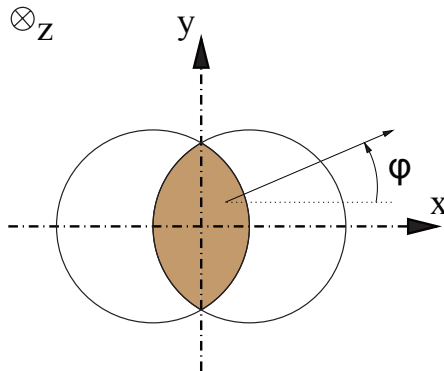


Figure 3.1: Spatial distribution of a non-central collision in the transverse plane.

$$s(x, y, z) = s_0 \exp \left(-\frac{x^2}{2\sigma_x^2} - \frac{y^2}{2\sigma_y^2} - \frac{z^2}{2\sigma_z^2} \right) \quad (3.8)$$

with σ_x and σ_y being the transverse widths of the distribution (Figure 3.1). Inserting this into the transverse acceleration (Equation 3.7) and integrating over t we get the time-dependent speed of the expansion:

$$\begin{aligned} u_x &= - \int_0^t c_s^2 \frac{\partial}{\partial x} \left(-\frac{x^2}{2\sigma_x^2} \right) dt = \int_0^t \frac{c_s^2 x}{\sigma_x^2} dt = \frac{c_s^2 x}{\sigma_x^2} t \\ u_y &= - \int_0^t c_s^2 \frac{\partial}{\partial y} \left(-\frac{y^2}{2\sigma_y^2} \right) dt = \int_0^t \frac{c_s^2 y}{\sigma_y^2} dt = \frac{c_s^2 y}{\sigma_y^2} t \end{aligned} \quad (3.9)$$

When the collision is non-central, it results by definition that $\sigma_x < \sigma_y$, which implies $u_x > u_y$. The expansion is strongest along the shorter axis of the overlap region, because here the pressure gradient is largest.

3.5 Transverse Mass Scaling

The particles in the fluid have a momentum distribution due to the fluid temperature. In contrast to the usual treatment of statistical quantities, we will allow our cell to not completely reach equilibrium by requesting maximum entropy for the particle distribution not measured by the Boltzmann-Gibbs entropy ($S = -k \sum_i p_i \ln p_i$) [65] but by the Tsallis entropy instead [66]:

$$S = -k \sum_i p_i^q \ln_q p_i$$

With the Tsallis index q representing the departure from equilibrated and uncorrelated microstates, and defining the q -logarithm and q -exponential [67], which in the limit $q \rightarrow 1$ reduce to the usual logarithm and exponential (see also Figure 3.2 left panel):

$$\ln_q(x) := \frac{x^{1-q} - 1}{1 - q} \quad \exp_q(x) := [1 + |x|(q - 1)]^{\frac{\text{sign}(x)}{q-1}}$$

Requesting that the particle distribution is of maximum entropy, it can be shown that in the rest frame of a fluid cell of volume dV , having dN particles in the

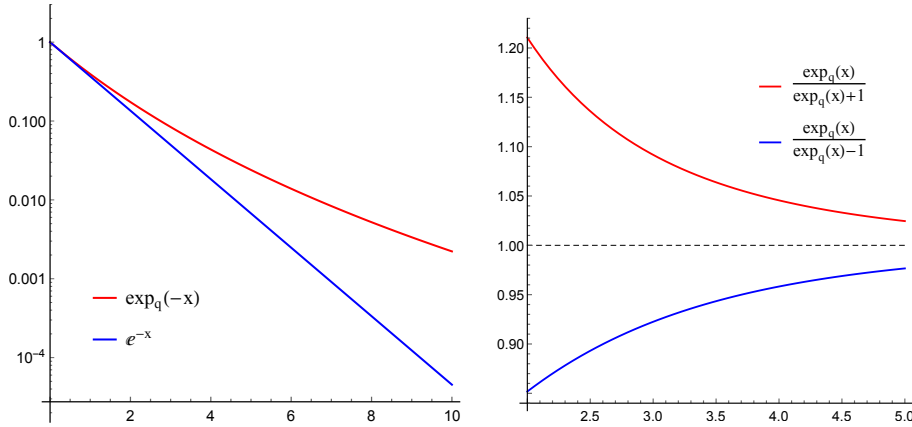


Figure 3.2: Comparison of the q -exponential with the normal exponential (left) and comparison of the fermionic with the bosonic spectrum (right). With $x = m_T/T$ and calculated at a realistic $q = 1.15$ [68, 69].

momentum range dp^3 with energy E and degeneracy g , and depending on the particle type (fermion/boson: $+/-$ respectively) the momentum distribution is [70]:

$$\frac{d^3n}{dp^3} = \frac{1}{dV} \frac{d^3N}{dp^3} = \frac{g}{(2\pi)^3} \left[\exp_q \left(\frac{E - \mu}{T} \right) \pm 1 \right]^{-1} \approx \frac{g}{(2\pi)^3} \exp_q \left(-\frac{E}{T} \right) \quad (3.10)$$

We already said that we want to examine a baryonless fluid, which implies that $\mu = 0$. We also drop the distinction between bosons and fermions¹², thus getting the Tsallis-Boltzmann momentum distribution, which would further reduce to the Maxwell-Boltzmann distribution in the limit $q \rightarrow 1$. In the following we want to restrict ourselves to particles moving faster than the fluid. The energy of a particle of momentum p in the fluid cell with velocity u as measured in the laboratory frame can be written as:

$$E = p^\mu u_\mu = p^0 u^0 - \vec{p} \cdot \vec{u} = u^0 \sqrt{m_0^2 + \vec{p}^2} - \vec{p} \cdot \vec{u}$$

In the last step Equation 2.6 has been used. We further restrict ourselves to the radial direction, studying particle production at $\eta = 0$. This implies $p_z = 0$ and $p = p_T$. Together with the definitions of transverse momentum (Equation 2.12) and transverse mass (Equation 2.13) the last expression can be now written as:

$$E = m_T u^0 - p_T u_T \quad (3.11)$$

And thus the momentum distribution becomes:

$$\frac{d^3N}{dp^3} \propto \exp_q \left(-\frac{m_T u^0 - p_T u_T}{T} \right) \quad (3.12)$$

¹²For a m_T of a few times the T_c onwards this approximation is very good (shown in Figure 3.2 right panel)

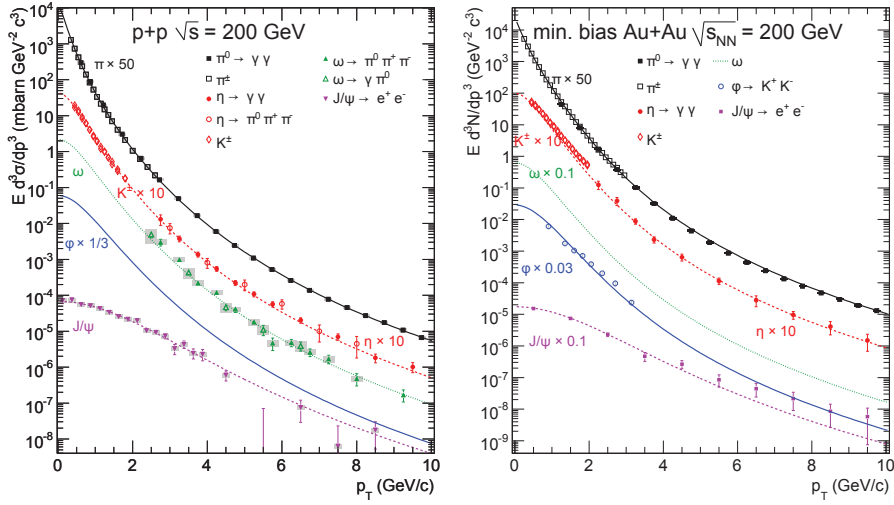


Figure 3.3: Comparison of pp (left) and $Au+Au$ (right) data to m_T -scaling at $\sqrt{s_{NN}} = 200$ GeV at the RHIC [75]

In the picture of a motionless fluid ($u_T = 0$, $u^0 = 1$), this momentum distribution becomes the so-called Tsallis momentum spectrum:

$$\frac{d^3 N}{dp^3} \propto \exp_q \left(-\frac{m_T}{T} \right) \quad (3.13)$$

This result is strictly true only for the particles that are moving through the medium. Inspired by the Cooper-Frye freeze-out picture [71] we however assume that the hadronization does not change the momentum distribution, which means that all particle species (pion, kaon, kaon...) will have the same momentum spectrum when expressed in m_T . This is the m_T -scaling property. And indeed in pp as well as in p - Pb collisions where there should be no fluid and thus no fluid motion, Equation 3.13 describes the data very accurately: for both, unidentified and identified particles [72–74]. For heavy-ion collisions the underlying spectrum must be tweaked, and the m_T -scaling property is less accurate. Figure 3.3 shows a compilation of measurements together with a parametrisation based on m_T -scaling.

This pure hydrodynamic derivation does not work however for Ion-Ion collisions, where the strongly interacting medium produces effects of non-thermodynamical nature, especially for high momenta. This introduces deviations from the functional form described here. Thus there the momentum spectra are described by functional forms with a different high momentum behaviour, like e.g. proposed by Hagedorn [76]. The differences are however still rather subtle and it is indeed nice to see that one can reach this important result from first principles.

3.5.1 Breakdown of m_T -Scaling

Up to now a motionless fluid was assumed in the calculation, which is not exactly true in heavy-ion collisions. Additionally to this, also the interactions of the particles with the medium introduce subtle changes to the spectra, so that these are no longer accurately described by the Tsallis function. For a first estimation of the

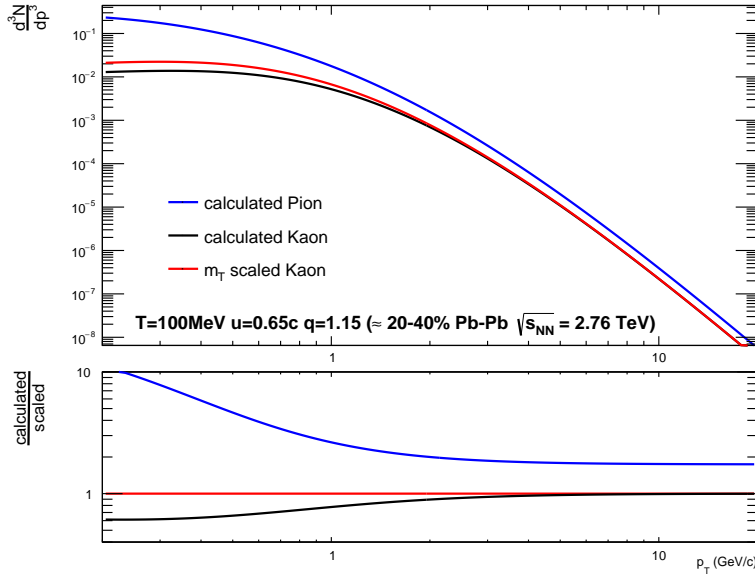


Figure 3.4: For low momenta the m_T -scaling (red) deviates from the Tsallis spectra (black) when calculated with finite flow. The baseline for the m_T -scaling is usually the pion (blue). This plot can be compared to Figure 7.3 showing the situation with real data.

consequence of a finite flow to the grade of the m_T -scaling approximation, however, these additional effects shall be disregarded and the spectra are further assumed to be Tsallis-like.

The m_T -scaling property is extensively used when a particle's momentum spectrum is being calculated based on another particle's momentum spectrum measurement. Usually the particle measured is the pion, thus the momentum spectrum of some other particle P of mass m_P would be approximated due to m_T -scaling to:

$$\frac{d^3 N_P}{dp^3} \approx \frac{d^3 N_\pi}{dp^3} \frac{\exp_q \left(-\frac{\sqrt{m_P^2 + p_T^2}}{T} \right)}{\exp_q \left(-\frac{\sqrt{m_\pi^2 + p_T^2}}{T} \right)}$$

While the particle ratio would be approximated to:

$$\Leftrightarrow \frac{\left(\frac{d^3 N_P}{dp^3} \right)}{\left(\frac{d^3 N_\pi}{dp^3} \right)} \approx \frac{\exp_q \left(-\frac{\sqrt{m_P^2 + p_T^2}}{T} \right)}{\exp_q \left(-\frac{\sqrt{m_\pi^2 + p_T^2}}{T} \right)} \quad (3.14)$$

Figure 3.4 shows the discrepancy between the left hand side (real spectrum ratio) and the right hand side (m_T -scaling ratio) of Equation 3.14 as well as their double ratio. It was calculated for the kaon with the pion as baseline and using a realistic combination of the fluid velocity, temperature and Tsallis index ([68, 69, 77, 78]). The overall scaling factor must be measured, and introduces its own uncertainty.

With increasing particle p_T , the grade of the m_T -scaling approximation increases, the flow becomes more and more negligible. So for Pb-Pb collisions, the situation is

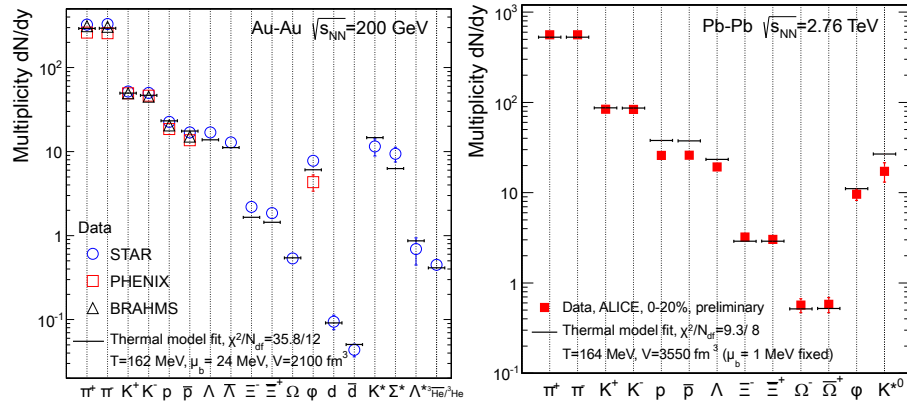


Figure 3.5: Thermal Model particle ratios compared with measurements from RHIC (left) and LHC (right) [80].

rather obscure: in the low momentum region, below $2 - 4$ GeV/ c , the spectrum can be described by a Tsallis momentum spectrum, where however due to the presence of flow the simple m_T -scaling does not work, and in the high momentum region the m_T -scaling does work but the spectrum is not of the simple Tsallis form anymore.

Although not perfect, in practice the m_T -scaling is still sufficiently accurate for many studies. Also in this work it is extensively used.

3.6 Particle Ratios

Instead of analysing the momentum spectrum of the generated particles, the momentum distribution (Equation 3.10) can also be used to obtain the number of particles of a given species emitted by a fluid element. Integrating over all momenta we get for each particle species i :

$$n_i = \frac{g_i}{(2\pi)^2} \int_0^\infty \frac{p^2 dp}{\exp_q\left(\frac{E - \mu_B}{T}\right) \pm 1}$$

Again assuming the Cooper-Frye freeze-out picture, this expression can be directly viewed as a statement for each produced particle species. Thermal models based on this approach [48, 49] have turned out to be very accurate in describing the real particle ratios in a wide energy range [79, 80]. Figure 3.5 shows the measured particle ratios compared to thermal model global fit.

3.7 Chemical and Kinetic Freeze-Out

While in pp collisions the temperatures extracted from measurements of the particle ratios and the m_T spectra are similar, in heavy-ion collisions this is no longer the case. The temperature from the momentum distributions is significantly below that of the particle ratios. The former is called kinetic freeze-out temperature T_k and the latter chemical freeze-out temperature T_{ch} . Temperatures extracted at the LHC

are: $T_k \approx 100$ MeV [68, 69, 77] and $T_{ch} \approx 165$ MeV [80]. The interpretation of the observation that $T_k < T_{ch} \approx T_c$ is that there is a two-step procedure:

Inelastic interactions in the expanding and cooling medium cease at T_c , thus fixing the hadron composition. When the mean free path exceeds the system size, also the elastic interactions come to an end, fixing the momentum distribution.

3.8 Anisotropic Flow

As shown in Chapter 3.4 in case of non-central collisions, the initial spacial anisotropy (Equation 3.8) is translated into a velocity, or momentum anisotropy (Equation 3.9). To get a momentum dependent result of this anisotropy, the observation of the transverse expansion (Equation 3.9) is now to be incorporated into the momentum distribution (Equation 3.12).

But first the problem needs to be expressed in polar coordinates, because these are more natural to this problem. Any angular distribution can be described in a Fourier-decomposition. The polar form of the Gaussian profile (Equation 3.8) of the entropy on the transverse plane with eccentricity ε_n then becomes:

$$s(r, \varphi) = s_0 \exp \left(-\frac{r^2}{2\sigma_r^2} \left(1 + 2 \sum_n \varepsilon_n \cos n\varphi \right) \right) \quad (3.15)$$

Inserting this into the polar form of the transverse acceleration (equivalent to Equation 3.7)

$$\frac{\partial u_r}{\partial t} = -\frac{1}{\epsilon + P} \frac{\partial P}{\partial r} = -c_s^2 \frac{\partial(\ln s)}{\partial r}$$

yields the polar form of the transverse speed (equivalent to Equation 3.9):

$$u_r(\varphi) = t \frac{c_s^2 r}{\sigma_r^2} \left(1 + 2 \sum_n \varepsilon_n \cos n\varphi \right) = v_T \left(1 + 2 \sum_n \varepsilon_n \cos n\varphi \right)$$

with $v_T = tc_s^2 r / \sigma_r^2$ being the transverse fluid speed. With $u^0 = \sqrt{1 + \bar{u}^2}$ and expanding to the first order in ε_n it follows:

$$u^0(\varphi) = \sqrt{1 + (v_T \left(1 + 2 \sum_n \varepsilon_n \cos n\varphi \right))^2} \approx v^0 + \frac{v_T^2}{v^0} 2 \sum_n \varepsilon_n \cos n\varphi$$

Both $u(\varphi)$ and $u^0(\varphi)$ can now be inserted into Equation 3.11:

$$E = m_T u^0 - p_T u_T = \left(m_T v^0 - p_T v_T \right) + \left(m_T \frac{v_T^2}{v^0} - p_T v_T \right) 2 \sum_n \varepsilon_n \cos n\varphi$$

This in turn is inserted into the general expression of the momentum distribution (Equation 3.10) yielding a φ -dependent momentum distribution:

$$\frac{d^3 N}{p_T dp_T dp_z d\varphi} \propto \exp_q \left(\frac{-m_T v^0 + p_T v_T}{T} + \frac{-m_T v_T^2 / v^0 + p_T v_T}{T} 2 \sum_n \varepsilon_n \cos n\varphi \right)$$

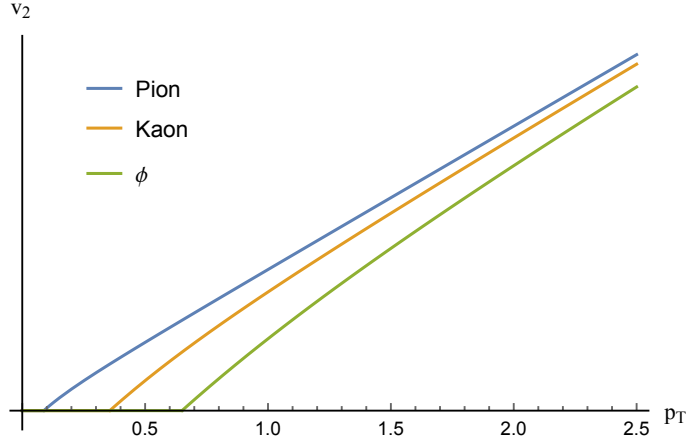


Figure 3.6: Elliptic flow of particles of different masses based on Equation 3.17 with a fluid velocity of $0.65 c$ [77].

The first term is the momentum distribution as known from Equation 3.12 and the second is the anisotropic flow. The latter is a relatively small modulation to the total spectrum. In that case the q -exponential approximately splits while the q can be dropped altogether for the modulation part:

$$\frac{d^3 N}{p_T dp_T dp_z d\varphi} \propto \exp_q \left(-\frac{m_T v^0 - p_T v_T}{T} \right) \exp \left(\frac{p_T - m_T v_T / v^0}{T} 2v_T \sum_n \varepsilon_n \cos n\varphi \right)$$

While the first term is the already known momentum distribution, the second term can be further simplified with $\exp(x) \approx 1 + x$:

$$\frac{d^3 N}{p_T dp_T dp_z d\varphi} = N_0 \cdot \left(1 + 2 \sum_n \frac{v_T \varepsilon_n}{T} \left(p_T - m_T \frac{v_T}{\sqrt{1 + v_T^2}} \right) \cos n\varphi \right)$$

The φ -dependent momentum distribution can now be rewritten in terms of v_n to a Fourier-like decomposition

$$\Rightarrow \frac{d^3 N}{p_T dp_T dp_z d\varphi} = N_0 \cdot \left(1 + 2 \sum_n v_n \cos n\varphi \right) \quad (3.16)$$

by defining the Fourier coefficient v_n :

$$v_n := \frac{v_T \varepsilon_n}{T} \left(p_T - m_T \frac{v_T}{\sqrt{1 + v_T^2}} \right) \quad (3.17)$$

Analysing this result for a given fluid velocity v_T it can be shown that the v_n coefficient increases almost linearly with p_T . At the same p_T , higher-mass particles have a lower v_n , a feature called mass ordering (Figure 3.6). The result is mathematically consistent only when the particles move at speeds higher than the speed of the fluid, thus when the term in brackets of the above equation is positive.

Throughout the derivation we have argued that we analyse an inviscid fluid. However, from string theory it appears that there is a non-zero lower bound to how

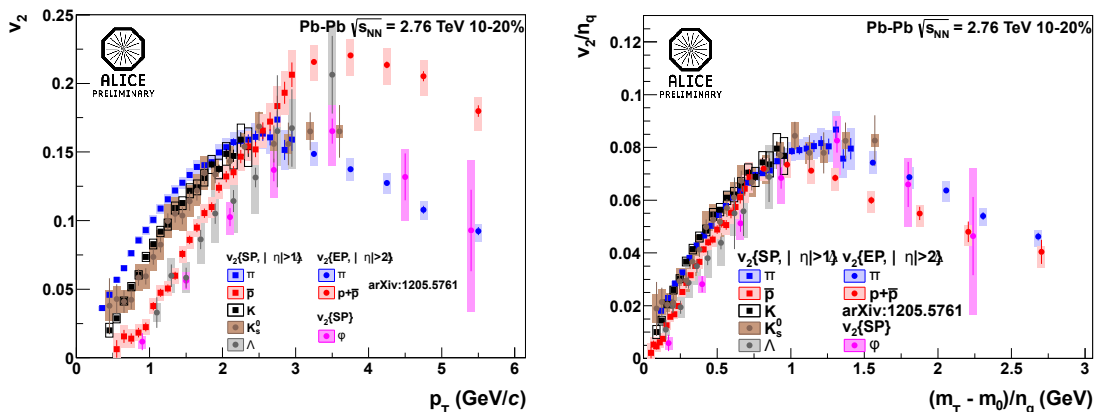


Figure 3.7: The measured identified-particle elliptic flow (left) is reasonably described by the KE_T -scaling (right) [89]

low the viscosity can get [81, 82]. Due to its dissipative effects, viscosity drives down the v_n , with ever stronger suppression of the higher orders [83].

Furthermore, due to the interaction of particles traversing the medium with the medium, and the path-length dependence of the energy-loss, the v_n decreases at intermediate p_T and remains low at higher p_T . [84–86]

3.9 Scaling Properties of Anisotropic Flow

The quarks and gluons of the QGP will eventually hadronize into measurable particles. During this hadronization, partons close in phase space have the chance to coalesce. In this picture, the hadron momentum will be the sum of the momenta of its recombined partons. Indeed, at RHIC it was found that the absolute v_n of different particle species scale with the number of valence quarks [87, 88].

$$v_n^{hadron}(p_T) = \sum_i v_n^{parton}(x_i \cdot p_T) \quad , x_i = \frac{p_{parton}}{p_{hadron}}$$

This scaling property is called quark number scaling, it is not perfect however. The scaling property is improved when not the momentum but the kinetic energy is viewed as conserved. With the restriction to the radial direction ($\eta = 0$, $p = p_T$) we can use the definition of the transverse kinetic energy (Equation 2.14) and write:

$$v_n^{hadron}(KE_T) = \sum_i v_n^{parton}(x_i \cdot KE_T) \quad , x_i = \frac{p_{parton}}{p_{hadron}}$$

Figure 3.7 shows the scaling behaviour with ALICE measurements. Both scalings are rather empirical findings and cannot not reproduce all the data in every detail.

3.10 Non-Flow Effects

All correlations among particles which are not due to the collective effects of the expanding fluid are called non-flow effects. These comprise two- and multi-particle

correlations due to momentum conservation, quantum statistics, resonances or jet production. In phase space such correlations are, however, of a more local nature than flow and usually scale inversely to the number of analysed particles. Observing particles at very different pseudorapidities suppresses such non-flow effects from flow measurements effectively and efficiently. [90–92]

4 Experimental Setup

4.1 The Large Hadron Collider

The Large Hadron Collider is a ring accelerator at the European Organisation of Nuclear Research (commonly called CERN) situated near Geneva, at the border of Switzerland and France. In 2001 the construction of the LHC started, replacing the predecessor accelerator LEP (Large Electron-Positron Collider) in its 26.7 km circumference tunnel. Almost exactly 25 years after its approval by the CERN Council on December 16th 1994, the first pp collisions were recorded on November 23rd 2009.

The peak centre-of-mass collision energy of the collider is 14 TeV for protons. To achieve this, the LHC consists of 1392 superconducting dipole magnets generating a magnetic field of 8.33T, to guide the two particle beams of opposing directions on their way through the tunnel. With this magnetic field it is possible reach an energy of up to 5.52 TeV for fully stripped lead ions $^{208}\text{Pb}^{82+}$. The two beams, which are 20 cm apart, are focused by 392 superconducting quadrupole magnets to a size of only $16\ \mu\text{m}$ in transverse direction. The magnets are cooled to 1.9K, which is well below the transition temperature of the NbTi alloy windings in the magnets, to maximise the field strength required for the highest particle energies and for preserving the Helium in its superfluid phase.

Before being injected into the LHC particles are successively pre-accelerated in an accelerator cascade starting at the linear accelerator LINAC 2 / LINAC 3¹³ followed by the accelerator rings PSB / LEIR¹³, PS and SPS (Figure 4.1). Once in the LHC, particles are further accelerated up to the peak energy.

The actual layout of the LHC is not a perfect circle, but includes eight 528 m straights and eight arcs. In the middle of four of the straights the two particle beams cross each other. These are the spots where the collisions happen and are called interaction points (IP). Each of the four experiments of the LHC has one of these points at its centre. The other four straights house the beam cleaning, dumping and accelerating facilities. In Table 4.1 the main parameters of the LHC are shown.

For all today's experiments it is important to collect lots of statistics. This is due to the fact that many of the interesting physics processes have a low cross section and are thus very rare. In this context the beam intensity or the so-called luminosity \mathcal{L} is an important measure.

$$\mathcal{L} = \frac{N_a N_b n f_r}{4\pi\sigma_x\sigma_y} \quad (4.1)$$

Due to technical reasons, the two beams (a and b) are not continuous, but consists of a number of bunches N where each bunch consists of a number of particles n . These bunches have a revolution frequency f_r and a transversal profile with the widths σ_x and σ_y . The units of the luminosity are $\text{cm}^{-2}\text{s}^{-1}$. When multiplied with the total cross section of a given process it yields the rate of that process. [93, 94]

¹³The first mentioned accelerator is used for protons exclusively, the second mentioned is for lead ions.

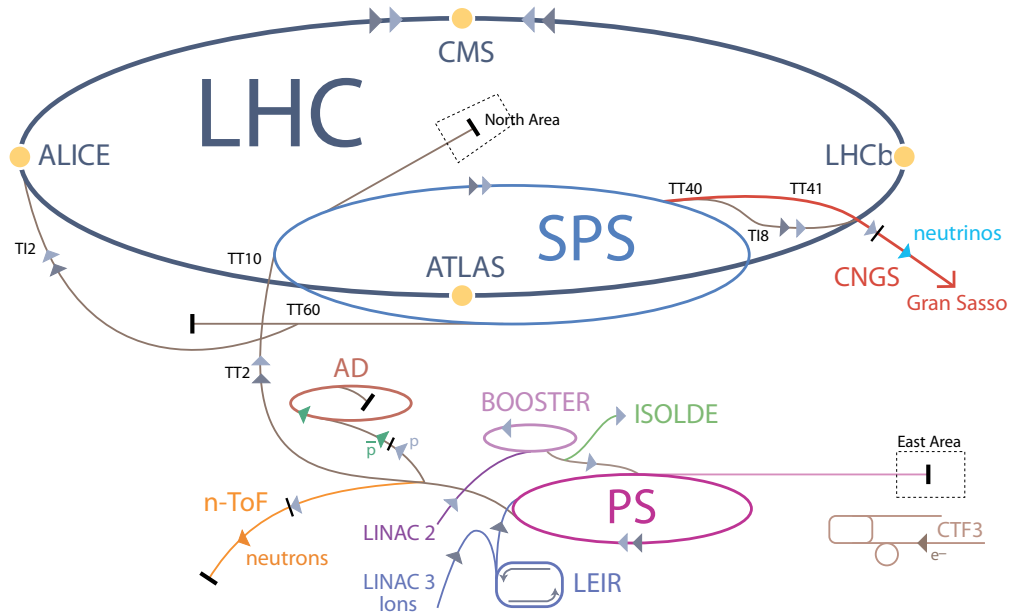


Figure 4.1: The CERN accelerator complex. Protons are starting their way at LINAC 2 and lead ions at LINAC 3. [95]

Parameter	Value
Total length	26.659 km
Minimal radius	2805 m
Momentum at injection per proton	450 GeV/c ²
Maximal momentum per proton	14 TeV/c ²
Dipole field at 450 GeV/c ²	0.535 Tesla
Dipole field at 7 TeV/c ²	8.33 Tesla
Revolution frequency	11.245 kHz
Particles per bunch	$1.15 \cdot 10^{11} / 10^8$
Bunches per beam	2808 / 592
Transverse beam size at interaction	16.7 μm
Longitudinal bunch size	7.55 cm
Luminosity	$10^{34} \text{ cm}^{-2}\text{s}^{-1} / 10^{27} \text{ cm}^{-2}\text{s}^{-1}$

Table 4.1: Main parameters of the LHC. [93, 95]

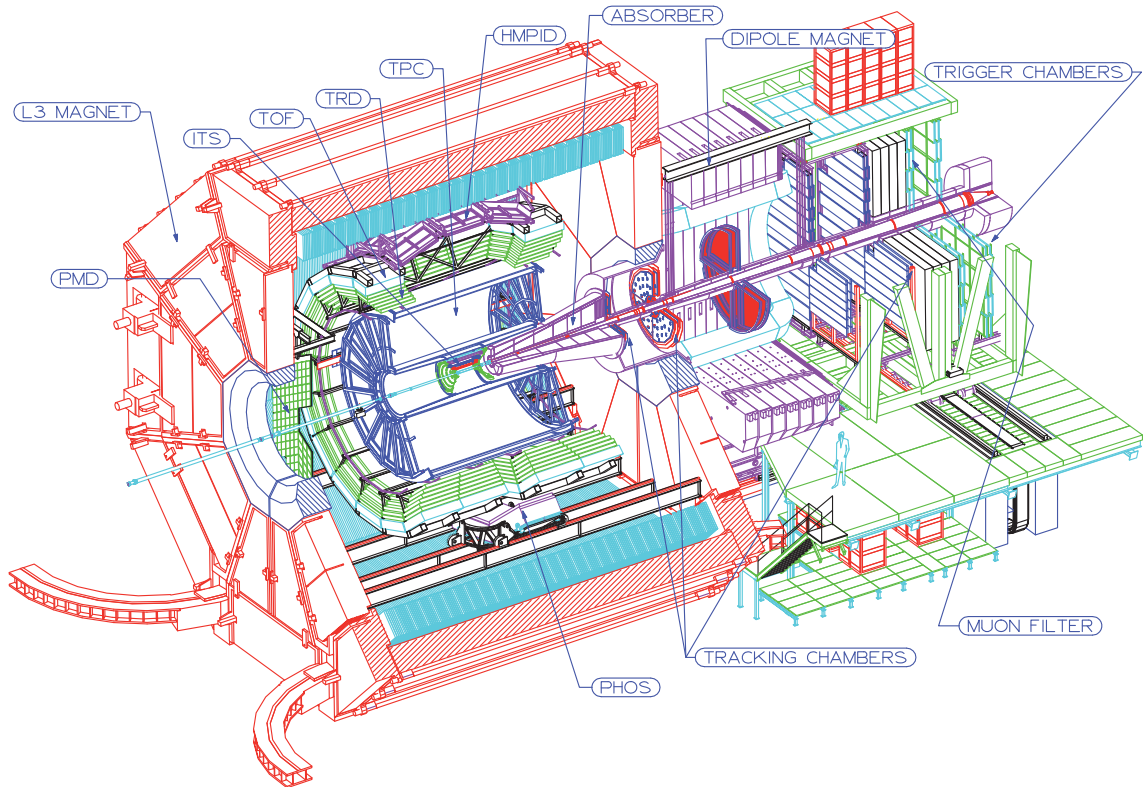


Figure 4.2: The ALICE Experiment and its detectors.

4.2 A Large Ion Collider Experiment (ALICE)

ALICE is an experiment devoted to the study of strongly interacting matter and the characteristics of the Quark-Gluon-Plasma in heavy-ion collisions.

The aspect of ALICE is dominated by the huge magnet of the old LEP experiment L3, which is being reused (Figure 4.2). Its dimensions are almost 15 m cubed, giving enough room for most of the particle detectors. Only the forward spectrometer of the muon detector resides outside the magnet. The other detectors are placed onion-like around the interaction point.

Scope of this magnet is to create a homogeneous magnetic field in which charged particles are forced to circular trajectories with radii dependent on their momentum. The particle mass, in fact the quantity of interest, can only be identified with the help of additional measurements. The magnetic field of 0.5 T which is the lowest of all LHC experiments allows reconstruction down to very low transverse momenta.

As a large number of particles are produced in heavy-ion collisions, detectors must be endowed with high spatial resolutions to be able to trace the trajectories. Data taking must be capable of routing and saving enormous amounts of data.

The ALICE experiment incorporates 18 detectors, that can be divided into two groups: the Central-Barrel detectors, and the forward detectors.

4.2.1 Orientation of the Coordinate System

The ALICE coordinate system is a right-handed orthogonal Cartesian system with its point of origin at the beams' interaction point (IP). [96]

z-Axis is parallel to the beam. The experiment side pointing towards positive z is called side A (as in anti-clockwise direction on the accelerator) and the side pointing towards negative z is called side C (clockwise). The muon arm is on side C, at negative z.

x-Axis is perpendicular to the beam direction, aligned with the local horizontal and pointing to the accelerator centre. Positive x is from the IP toward the accelerator centre (side I, inward), negative x is outward (side O, outward). Figure 4.2 is shown as seen from side I.

y-Axis is perpendicular to the x-axis and the beam direction, pointing upward. Positive y is from the IP upward (side U), negative y is downward (side D)

The x and y axes span the transverse plane. The azimuthal angle φ is in this plane, increasing from the x-axis at $\varphi = 0$ towards the y-axis at $\varphi = \pi/2$. The polar angle θ increases from the z-axis at $\theta = 0$ ($\eta = \infty$) towards the transverse plane at $\theta = \pi/2$ ($\eta = 0$).

4.2.2 Central-Barrel Detectors

The central barrel incorporates all main detectors. The most important detectors have full azimuthal coverage in the pseudorapidity range of $|\eta| < 0.9$. The interplay of these detectors provides an excellent particle identification, good track and vertex resolutions with a wide transverse momentum reach. [97]

Time Projection Chamber

The Time Projection Chamber (TPC) is the main ALICE detector, and with its active volume of 88 m^3 also the biggest. Its size is key for its task: High-resolution particle tracking and high-efficiency particle identification.

The TPC (Figure 4.3) consists of a cylindrical field cage that is surrounded by an airtight containment vessel with two end-plates sealing off at the base. The two end-plates are equipped with two rings of 18 multi-wire proportional chambers (MWPC) with 557 568 readout pads. Halfway through the cylinder (at $\eta = 0$) there is the central electrode. With its high voltage, and together with the grounded end-plates, it provides the necessary electric field along which charged particles can drift. Filled with a Ne CO₂ gas mixture charged particles flying through the gas lose energy by colliding with the gas molecules, ionising the gas along their path. The electrons from the ionized atoms drift along the field towards the readout planes, measuring the location and the drift time of the electron, reaching a resolution of about 0.8 – 1.2 mm in all three dimensions. The particle tracks are reconstructed joining all measured ionization electron positions to continuous tracks. The magnetic field of the L3 magnet bends the tracks, which allows to assign a momentum to each

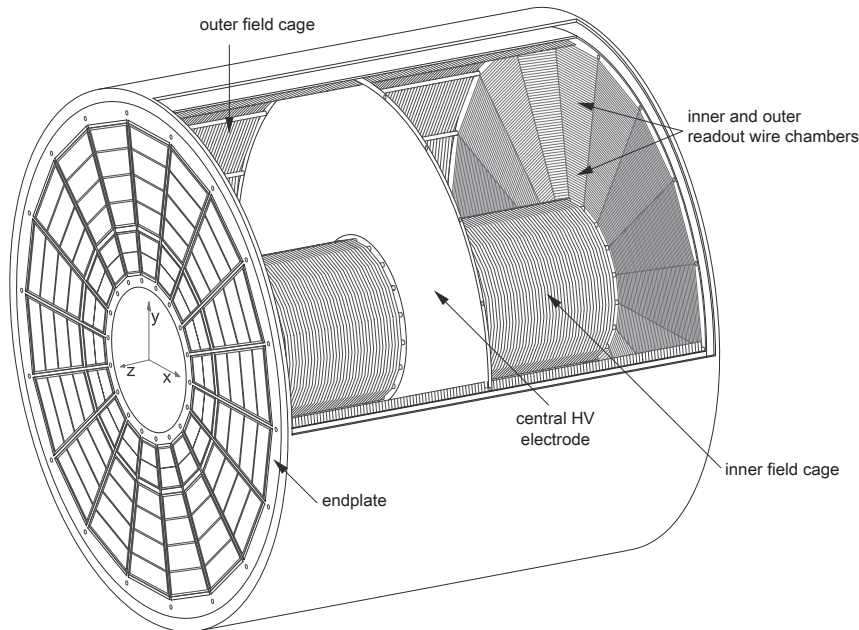


Figure 4.3: Layout of the ALICE TPC

track. Together with the track length, the total amount of ionization along the whole track is measured and provides the dE/dx -measurement.

The average amount of energy loss per unit length and thus the amount of ionisation electrons is dependent on the properties of the gas and the properties of the particle. It is given by the Bethe-Bloch equation:

$$\left\langle -\frac{dE}{dx} \right\rangle = 4\pi N_A r_e^2 m_e c^2 z^2 \frac{Z}{A} \frac{1}{\beta^2} \left[\frac{1}{2} \ln \left(\frac{2m_e c^2 \beta^2 \gamma^2 W_{max}}{I^2} - \beta^2 - \frac{\delta(\beta\gamma)}{2} \right) \right] \quad (4.2)$$

where N_A is Avogadro's number, m_e is the electron mass, r_e is the classical electron radius. z is the charge of the particle, β is its velocity and γ the Lorentz factor. A and Z is the mass number and the proton number of the gas, I is its effective ionization potential and W_{max} is the maximum energy transfer allowed in each interaction of the particle of mass M with the gas:

$$W_{max} = \frac{2m_e c^2 \beta^2 \gamma^2}{1 + \left(2\gamma + \frac{m_e}{M} \right) \frac{m_e}{M}}$$

At low particle energy the Bethe-Bloch equation formula is dominated by the term β^{-2} and thus the energy loss falls steeply. With further increasing velocity the energy loss stabilises and rises slightly in the relativistic regime until it saturates in the high relativistic region. Based on the amount of energy loss and combined with the momentum measurement particles can be identified.

The size of the TPC was chosen given the following considerations: The minimum possible inner radius of the TPC ($r_{in} \approx 85$ cm) is given by the maximum acceptable hit density, the outer radius ($r_{out} \approx 250$ cm) is determined by the minimum track length required for the expected dE/dx resolution ($\sigma_{TPC} \approx 5\%$) and the cylinder length of 5.1 m is trade-off between the maximum acceptable drift time and the minimum acceptable polar acceptance. [15, 98–101]

detector	layer	radial	acceptance		resolution	
		position (cm)	azimuth	polar	transverse plane	along beam
SPD	1	3.9	full	$ \eta < 2.0$	$100 \mu\text{m}$	$600 \mu\text{m}$
	2	7.6		$ \eta < 1.4$		
SDD	3	15.0	full	$ \eta < 0.9$	$200 \mu\text{m}$	$600 \mu\text{m}$
	4	23.9				
SSD	5	37.8	full	$ \eta < 1.0$	$300 \mu\text{m}$	$2400 \mu\text{m}$
	6	42.8				

Table 4.2: Active area of the ITS layers

Inner Tracking System

The Inner Tracking System (ITS) is the innermost detector of ALICE. Its main objective is to determine the primary and secondary vertices. It improves the momentum and angle resolution of the reconstructed particles and contributes to the particle identification, especially for low-momentum particles. It consists of three types of two-layered silicon detectors, from inside to outside these are: The very high-resolution silicon pixel detector (SPD) situated at radii of 4 cm and 7 cm, which is followed by the silicon drift detector at 15 cm and 24 cm, and lastly the layers of the silicon strip detectors at 39 cm and 44 cm.

The first two layers are not only crucial for the primary and secondary vertex determination. A match of an inward-track prolongation from the outer detectors can provide important information for separating decay electrons from primary particles and decay electrons from secondary particles. Thus electrons from gamma conversions outside of the innermost layers can be completely suppressed, bringing down the relevant material budget.

The analogue readout of the four outer layers, provide the possibility for a dE/dx measurement. [102, 103]

Transition Radiation Detector

The Transition Radiation Detector (TRD) is a gas detector, at a radial position $2.9 < r < 3.7$ m (Figure 4.4). It serves mainly two independent purposes in ALICE: It completes the particle tracking between TPC and TOF and distinguishes between pions and electrons in momentum regimes where TPC and TOF are not efficient. The TRD is sub-sectioned into 18 super-modules, containing 5 stacks of 6 readout chambers each, totalling into 540 readout chambers. The readout chambers consist of a radiator of 48 mm thickness and a drift chamber of 37 mm thickness. At the entrance of the drift chamber there is the drift electrode, which is followed by the cathode and anode wires and finally the readout pads. By the applied high voltage between the drift electrode and the anode wires, ionisation electrons drift towards the amplification region. The cathode wires separate the drift from the amplification region and guarantee a homogeneous field in the drift region.

Each readout chamber has about 2000 readout pads with an active area of $0.725 \times 8.5 \text{ cm}^2$. The pads of the 6 readout chambers of each stack have an alternating tilt of 2° in the pad plane. The pads are thus rather parallelograms than rectangles.

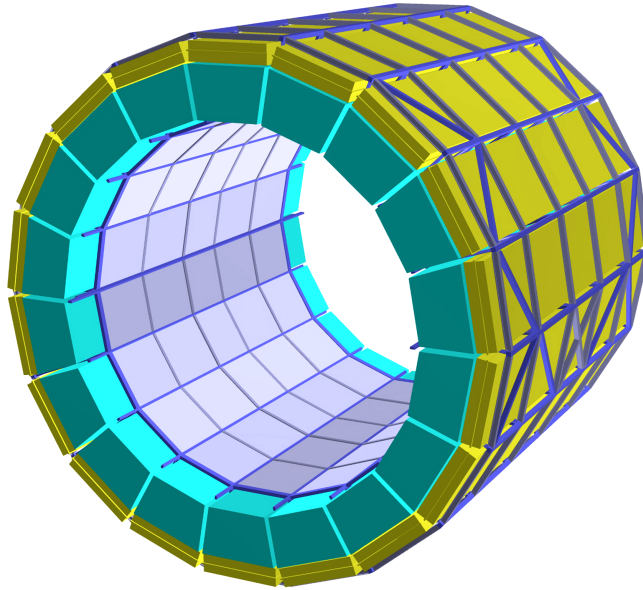


Figure 4.4: Layout of the ALICE TRD (green) and TOF (yellow)

This layout increases the total resolution along the longer side of the pad in beam direction.

As the TPC the TRD measures the charges released by a traversing particle. However, additionally to the ionization according to the Bethe-Bloch equation, the TRD radiator generates transition radiation for highly relativistic particles. The transition radiation was predicted by Ginzburg and Franz in 1946 [104] for non-relativistic particles and was first detected in 1959 by Goldsmith and Jelley [105]. A particle traversing the border of two regions with different dielectric constants may emit transition radiation. The energy is given by the following expression

$$\frac{d^2W}{d\omega d\vartheta} = \frac{2\alpha\hbar\vartheta^3}{\pi} \left[\left(\frac{1}{\gamma^2} + \vartheta^2 + \frac{\omega_1^2}{\omega^2} \right)^{-1} - \left(\frac{1}{\gamma^2} + \vartheta^2 + \frac{\omega_2^2}{\omega^2} \right)^{-1} \right], \quad (4.3)$$

where ω is the frequency, ϑ the angle of emitted radiation, $\omega_{1,2}$ are the plasma frequencies of the two media and finally γ is the Lorentz factor of the particle. This equation has a maximum at an angle of $\vartheta = 1/\gamma$ and thus the radiation gets preferably emitted in forward direction. The total energy is given by integrating Equation 4.3 over all angles and photon frequencies to

$$W = \iint \left(\frac{d^2W}{d\omega d\vartheta} \right) d\omega d\vartheta = \gamma \frac{\alpha\hbar}{3} \frac{(\omega_1 - \omega_2)^2}{\omega_1 + \omega_2}, \quad (4.4)$$

which is linearly dependent on the Lorentz factor of the particle.

However as the intensity is very low, the probability of a single emitted photon at one transition is of the order of the fine structure constant α , making many transitions necessary. The total probability for the emission of transition radiation (TR) inside a readout chamber is raised by the radiator, providing many transitions. It consists of a sandwich of two Rohacell HF71 foam sheets and mats of polypropylene

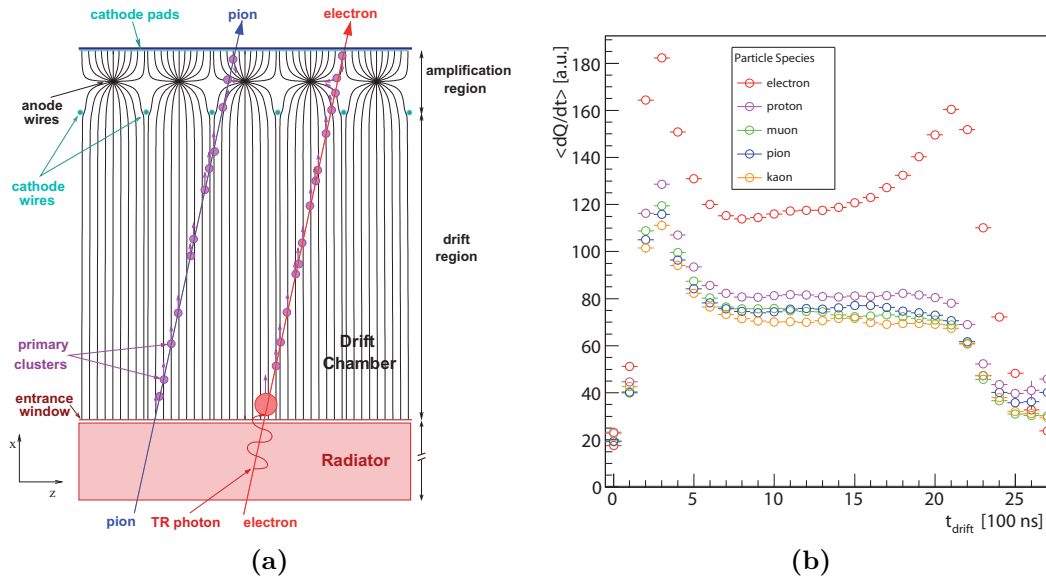


Figure 4.5: Cuts through a TRD readout chamber (a). Simulation of the average pulse height of different particles (b).

fibres. These components were chosen as a compromise between TR yield, radiation thickness and mechanical stability.

Transition radiation from ultra-relativistic electrons is in the energy range of soft to hard X-rays (< 50 keV [106]), which get absorbed by the gas, thus ionising it, when entering the drift chamber. Providing a high absorption probability is crucial as only then the TR photon can be detected. As the photo effect is proportional to the atomic number of the gas atoms, the gas used in the TRD chambers consists mainly of Xenon which has an atomic number of 54. Figure 4.5 shows the working principle. [107]

Time-of-Flight Detector

The Time-of-Flight detector (TOF) is exclusively dedicated to particle identification. It consists of Multi-gap Resistive-Plate Chambers (MRPC) with 157 248 readout pads distributed in 18 azimuthal sectors at distance of 3.8 m from the beam pipe, just outside the TRD (see also Figure 4.4). Each pad has an active area of 2.5×3.5 cm². To measure the time of flight the TOF requires a high-resolution start-of-time measurement, which is provided by the T0 detector. With a total time-resolution of 85 ps it contributes to the particle identification in the transverse momentum region where the TPC signals of the different particles have their crossings, and thus the dE/dx method cannot yield an unique answer (see also Figure 6.4). For this, it is necessary to match the track prolongation from the TPC with hits in the TOF. [108, 109]

Electromagnetic Calorimeter

The Electromagnetic Calorimeter (EMCal) is a Pb-scintillator sampling calorimeter consisting of 12672 towers with alternating layers of Pb and polystyrene scintillator

each covering an active area of $12 \times 12 \text{ cm}^2$. It has an acceptance of 107° in azimuth and a polar acceptance of $|\eta| < 0.7$ at a distance of 4.5 m from the beam pipe. The EMCal completes the measurements of jet properties and enhances the capabilities of measuring high p_T photons, neutral hadrons, and electrons. Matching the track momentum measured with the other detectors with the collected energy measured by the EMCal provides a powerful method for separating electrons from the other particles. [110]

Photon Spectrometer

The Photon Spectrometer is an electromagnetic calorimeter of high granularity, providing photon and neutral pion identification, and separating direct from decay photons. Its acceptance is restricted to the very mid-rapidity region of $|\eta| < 0.12$, and to 100° in azimuth.

High Momentum Particle Identification Detector

The High Momentum Particle Identification Detector is a proximity focusing Ring Imaging Cherenkov detector with a liquid radiator. It provides π^\pm/K^\pm and $K^\pm/(p, \bar{p})$ separation up to 3 GeV/c and 5 GeV/c respectively. [100]

4.2.3 Forward Detectors

In ALICE all detectors which have their acceptance in the range $|\eta| > 1$ are called to be in forward direction.

Muon Spectrometer

The Muon Spectrometer is exclusively devoted to the measurement of muons. Many important hadronic observables have muonic decay channels. As all leptons, muons do not interact strongly and can thus, once generated, propagate mostly unobstructed through the QGP.

The Muon Spectrometer is located in the forward part of the ALICE detector and covers an angular region of $2^\circ < \theta < 9^\circ$, corresponding to a pseudorapidity of $2.5 < \eta < 4.0$. It is composed of a dipole magnet, a trigger system and a tracking system. These are all located outside the ALICE L3 magnet, and are behind several absorbers which extend into the L3 magnet towards the interaction point in a conic form. The absorber stops most of the flux of hadrons, electrons and gammas, and thus guarantees a very high muon purity. However, although not being stopped, the muons arriving have experienced multiple scatterings inside the absorber, which leads to a reduced momentum resolution.

T0

The T0 supplies a fast timing signal which is used for a wake-up call to the TRD, it delivers the time reference for the TOF and determines the z position of the primary interaction. It consists of two rings of 12 Cherenkov counters mounted around the

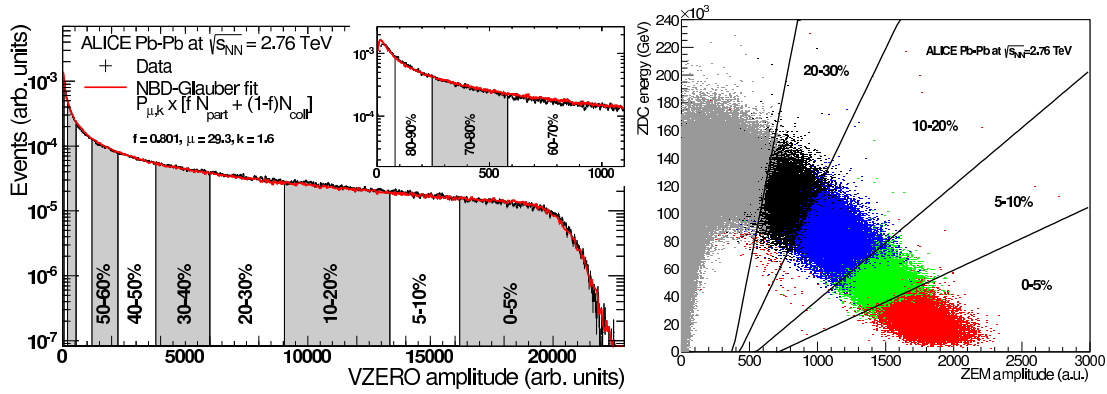


Figure 4.6: Centrality estimation using the V0 (left) and the ZDC (right)

beam pipe at opposite positions relative to the interaction point at $z = -72.7$ cm and $z = 375$ cm covering the pseudorapidity ranges $2.9 < \eta < 3.3$ and $-4.5 > \eta > -5$ respectively at full azimuthal coverage. [111]

V0

The V0 consists of two ring-arrays of plastic scintillator counters on opposing sides of the interaction point (A and C side). The V0A subdetector covers the pseudorapidity range $2.8 < \eta < 5.1$ while the V0C covers the range $-1.7 > \eta > -3.7$. It is used to reject background events for the MUON detector, it provides minimum-bias triggers for the central barrel detectors in both pp and ion-ion collisions, and it serves as an indicator of the centrality percentile of the collision via the deposited energy of the event (shown in Figure 4.6 left).

Additionally the detector generates a coarse event classification for ion-ion collisions based on three multiplicity levels: minimum-bias, semi-central, and central ion-ion collisions. [111, 112]

ZDC

Zero Degree Calorimeters are hadronic calorimeters used to collect the energy of the spectator nucleons. The Zero degree ElectroMagnetic calorimeters (ZEM) are used to collect the energy from gammas which is correlated to the energy of the collided participant nucleons. The correlation of the ZDC signal to the ZEM signal provides an additional centrality measure (shown in Figure 4.6 right). Additionally the ZDC can be used a luminosity monitor.

Two sets of hadronic ZDCs are located at 116 m on either side of the Interaction Point (IP) and two ZEMs are placed at about 7 m from the IP. [113]

FMD

The main purpose of the Forward Multiplicity Detector is to provide information about the charged particle multiplicity at pseudorapidities not covered by ITS. To-

gether with the ITS it provides a gap-less measurement of the charged particle multiplicity distributions the range $-3.4 < \eta < 5.0$. [111]

PMD

The Photon Multiplicity Detector measures multiplicity and the spatial distribution of photons, enabling the determination of the interaction plane, and the study of event-by-event fluctuations in the forward rapidity region.

4.2.4 Trigger Setup

Modern collider experiments search for improbable and thus rare events. For being able to still have enough statistics, high collision frequencies are needed. Saving continuously all data from all detectors is not an option for the ALICE experiment, since due to the high granularity, the detectors produce huge amounts of data while operating. Thus a trigger system must be implemented, to be able to activate the detectors and the data taking only when physical important events occur.

The Central Trigger Processor (CTP) combines and synchronises the trigger decisions from the triggering detectors, and sends the result to all detectors. Some detectors are continuously operational, some need a very early activation, and other can handle longer delays. Thus the triggering system is divided in multiple stages. The first trigger decision, called L0, must be delivered $1.2 \mu\text{s}$ after the collision took place. For that the triggering detectors contributing to this decision must hand in their decision already 800 ns after the collision. Only very fast detectors can achieve that. Slower trigger detectors, like the TRD, may have a delay up to $6.1 \mu\text{s}$ and contribute to the L1 trigger signal, which is then delivered after $6.5 \mu\text{s}$. After $88 \mu\text{s}$ the last trigger signal (L2) is delivered. It is used as a past-future protection, to veto against previous L1 triggers.

Being the fastest detector in the central barrel, the SPD can provide a multiplicity and topology based L0 trigger signal to other detectors. Additionally the TOF provides L0 triggers to select ultra-peripheral collisions, minimum bias events in proton-proton collisions and cosmic muons for the calibration of central detectors and cosmic-ray physics. The EMCal can be used to trigger on hard jets, photons and electrons at either L0 or L1.

4.2.5 ALICE-Software

In the ALICE Collaboration each sub-detector group is responsible for building and testing their detectors, mounting them into the experiment, and maintaining them. During operation detectors will generate data, which is analysed or reconstructed. The reconstruction algorithms must be in a working, well tested state when the experiment starts. This is only possible when all data output of the experiment can be simulated long before first collisions. This is especially challenging when taking into account the comparable low collision energies of previous experiments: e.g. RHIC has a peak energy of 500 GeV in pp and 200 GeV per nucleon in AA, which means that the models describing the expected characteristics of collisions at LHC were extrapolations with quite big uncertainties.

All reconstruction and simulation algorithms of the detector data are written in C++, and follow the concept of object oriented programming. The individual detector algorithms have a common interface and are concentrated into one package called AliRoot, which uses ROOT as its base. ROOT is a framework, which provides standardisation among different platforms (i386, AMD64, ppc ...), methods for many programming problems (mathematical, input and output, graphical...) and a C++ interpreter. Through this interpreter all methods within the compiled libraries of the AliRoot and ROOT framework can be called directly. Commands to the interpreter can be saved in so-called macros.

The AliRoot package is being developed with the help of an online version control system, called git. All changes are committed into the development repository including a short description. The version control system saves not only the newest version, but also all necessary information for extracting previous versions. This is a very important feature as in such a big project as AliRoot it is indeed possible that multiple incompatible changes are committed almost simultaneously by different people. All changes since the beginning of the development can be viewed by help of an online interface¹⁴. By branching in the current development repository, git also provides the possibility of creating stable releases. There the update policy is restricted to bug fixes only.

¹⁴<http://git.cern.ch/pubweb/>

5 Heavy-Flavour Elliptic Flow

Charm and bottom quarks are called heavy-flavour quarks or simply heavy quarks. They are called heavy because their mass is large compared to the relevant energy scale inside the QGP¹⁵:

$$m_Q \gg \Lambda_{QCD}$$

Because of this property, heavy quarks can be described perturbatively even at low momenta, in contrast to the light quarks or gluons which can be treated perturbatively only at high momenta. Due to their high mass, heavy-quark pair production is limited to the initial stage of the collisions, almost exclusively in primary and secondary hard partonic scattering processes [114]: The total heavy-quark yield is dependent mostly on the initial state, and not expected to be changed significantly by any final-state effects. Final-state effects which are the interactions of the quarks with the medium [115], are described by radiative [116, 117] and collisional energy loss [118, 119], and should produce a mass-dependent softening of the momentum distributions. Experiencing the full evolution of the medium, heavy-flavour hadrons and their products are thus effective probes to study its properties.

A way to study the heavy-quark energy loss in strongly interacting matter is to analyse that modification of the momentum spectra, by comparing the particle yield in heavy-ion collisions with pp collisions. This can be quantified by the nuclear modification factor R_{AA} :

$$R_{AA} = \frac{1}{\langle N_{coll} \rangle} \frac{dN_{AA}/dp_T}{dN_{pp}/dp_T} = \frac{1}{\langle T_{AA} \rangle} \frac{dN_{AA}/dp_T}{d\sigma_{pp}/dp_T}$$

where dN_{AA}/dp_T is the measured invariant yield in nucleus-nucleus collisions and dN_{pp}/dp_T ($d\sigma_{pp}/dp_T$) is the corresponding invariant yield (cross-section) in pp collisions. $\langle N_{coll} \rangle$ and $\langle T_{AA} \rangle$ are the average number of binary collisions and the nuclear overlap function in a given centrality bin, which are obtained via Glauber model calculations [37, 120] (see also Chapter 1.4.1). A strong suppression of heavy flavours was found at both RHIC [121–125] and at the LHC [126–129].

It was shown in Chapter 3 that describing the QGP as a thermalized fluid, the emergence of anisotropic flow (Equation 3.17) is a direct consequence of the spatial anisotropy of the collision system expressed in its azimuthal eccentricity (Equation 3.15). Particles emitted in the reaction plane have a shorter in-medium path length than those emitted perpendicularly to it, leading to a positive elliptic flow [130, 131].

Measurements of light flavours at RHIC [132, 133] and at the LHC [36, 134–136] show a large elliptic flow at low momenta, which is decreasing towards central collisions. This is considered as an evidence for the collective hydrodynamical expansion of the medium [137–139].

For heavy flavours the amount of the elliptic flow of low-to-intermediate momentum heavy quarks indicates the degree of thermalization of these heavy quarks, while at higher momenta this it is giving indications of the path-length dependence of the in-medium energy-loss. Measurements of heavy flavours that were conducted at RHIC [124, 140] at $\sqrt{s_{NN}} = 200$ GeV show a clear non-zero elliptic flow, while

¹⁵Although the top quark is also heavy, it does not produce any stable bound states

measurements at lower energy are found to be consistent with zero. At the LHC, the ALICE collaboration has measured the D-meson's elliptic flow at mid rapidity [141, 142] and heavy-flavour decay muons at forward rapidity [143]. Together with the related paper [144], this work extends the existing ALICE data, by quantifying the elliptic flow of heavy quarks through a measurement of the decay electrons at mid rapidity.

5.1 Subtraction Method

A very obvious way to measure heavy quarks is to measure the products of the coalescence of these heavy quarks directly. However, there is a variety of different hadrons into which heavy quarks can coalesce. And all these heavy-flavour carrying hadrons have in common that they have a wealth of different decay channels themselves, making it complicated to have a high-statistics pure sample.

In contrast to directly measuring the heavy-flavour hadrons, this work tries to go a different route, by measuring the decay electrons of all heavy hadrons at a time. Inspired by work previously conducted at the PHENIX experiment at RHIC [124, 145], a background electron cocktail will be subtracted from the inclusive electron measurement to reach the desired result. Due to the still relatively large branching ratios of the semi-leptonic decays of the heavy-quark hadrons and the high electron reconstruction capabilities of ALICE, there is the educated guess of an increased statistics compared to the direct measurement of heavy hadrons. At the very least this measurement will provide another perspective on the issue together with a different systematic.

The general idea is to measure the elliptic flow of all decay electrons (a.k.a. the inclusive measurement, Chapter 6), and then subtract the elliptic flow of all decay electrons from light hadrons (a.k.a. the background measurement, Chapter 7), resulting into the elliptic flow of decay electrons from heavy hadrons, which is the intended measurement of this work (Chapter 8):

$$v_2^{HFE} = \frac{(1 + R_{SB})v_2^{incl} - v_2^{back}}{R_{SB}} \quad (5.1)$$

where R_{SB} is the ratio of the heavy-flavour decay electron yield to that of the non-heavy-flavour background electrons.

5.2 Quantifying Anisotropic Flow

A number of different methods measuring the anisotropic flow in heavy-ion collisions have been published up to now: [90, 146–149]. The method used in this work is the so-called event plane method, which is generally one of the most widespread in use. Additionally the inclusive measurement and the needed data of the light flavour hadrons is cross-checked with the scalar-product method.

As shown in Chapter 3.8 anisotropic flow can be quantified by an azimuthal Fourier decomposition of the particle yield (Equation 3.16). However there it was tacitly assumed that the orientation of the symmetry axis of the collision is known. This defined the alignment of the problem in space (see Figure 3.1). This can of

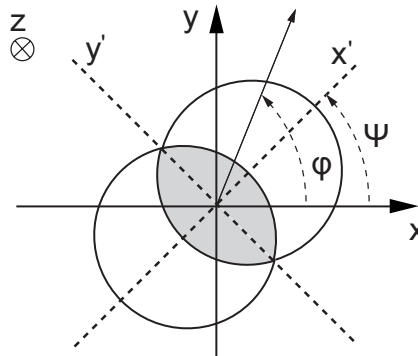


Figure 5.1: Definition of the angles used in the flow measurement. The coordinate system defined by the collision is arbitrarily rotated against the coordinate system of the experiment.

course only be true in a simulation, but not in the experimental measurement. There the Fourier decomposition of a given collision is actually given by

$$\frac{d^3N}{p_T dp_T dy d\varphi} = N_0 \left(1 + 2 \sum_n v_n \cos n(\varphi - \Psi_n) \right) \quad (5.2)$$

where Ψ_n is the azimuthal angle of the symmetry axis in this collision as measured in the laboratory system (see Figure 5.1). Next it will be shown how this axis can be defined and how the v_n parameters can be measured experimentally.

5.2.1 Event-Plane Determination

The reaction plane is the plane parallel to the beam connecting the centres of the two nuclei. This is however impossible to measure experimentally because we cannot take such a microscopic point of view during the measurement. The participant plane is the plane described by the symmetry axis of the participant nucleons. Due to fluctuations of the nucleons in the nuclei, the reaction plane and the participant plane do not coincide exactly. The only fact that the participant plane can be defined implies that there is a spatial anisotropy of the participants. As shown in Chapter 3.8 this is the spatial anisotropy (Equation 3.15) which induces exactly the particle number anisotropy we are after (Equation 5.2). So it seems to be the symmetry axis about which to measure the anisotropic flow. However, in our experiments we measure the products of the collision of the participant nucleons, and not the nucleons themselves. Thus, also the participant plane is impossible to measure.

Assuming that each of the recorded events comprises exactly one collision, the best we can do is to extract the symmetry axis of each event from the azimuthal particle number distribution. A such defined event plane should be close to the participant plane.

A very direct way to evaluate the event plane angle Ψ_n and the v_n parameters simultaneously for each event is to simply fit the azimuthal particle number distribution in the wanted (pseudo-) rapidity bin over all momenta with the needed

harmonics of the Fourier series [150]:

$$\begin{aligned} \frac{dN}{d\varphi} &= N_0 \left(1 + 2 \sum_n v_n \cos n(\varphi - \Psi_n) \right) \\ \Leftrightarrow \frac{1}{2N_0} \frac{dN}{d\varphi} - \frac{1}{2} &=: f(\varphi) = \sum_n v_n \cos n(\varphi - \Psi_n) \end{aligned} \quad (5.3)$$

This procedure has however a very important limitation: The particles used to determine the event plane angle and the flow parameters are exactly the same. Thus, when only the flow of a specific particle species is of interest, this would be limiting the event plane determination to just this particle species, unnecessarily decreasing the precision. In general it is advantageous to split the measurement in two: determine the event plane for each event with all available particles, and then evaluate the v_n parameters for the particle species analysed averaging over all events.

It can be shown that:

$$\begin{aligned} v_n \cos n(\varphi - \Psi_n) &= v_n \cos(n\Psi_n) \cos(n\varphi) + v_n \sin(n\Psi_n) \sin(n\varphi) = \\ &= a_n \cos(n\varphi) + b_n \sin(n\varphi) \end{aligned}$$

with the Fourier coefficients $a_n := v_n \cos(n\Psi_n)$ and $b_n := v_n \sin(n\Psi_n)$. Yielding the usual form of a Fourier series:

$$f(\varphi) = \sum_n v_n \cos n(\varphi - \Psi_n) = \sum_n a_n \cos(n\varphi) + b_n \sin(n\varphi)$$

For a given function $f(\varphi)$ the Fourier coefficients can be expressed as:

$$a_n = \frac{1}{\pi} \int_{-\pi}^{\pi} f(\varphi) \cos(n\varphi), \quad b_n = \frac{1}{\pi} \int_{-\pi}^{\pi} f(\varphi) \sin(n\varphi)$$

Taking a_n and b_n as components of a vector, defines the flow vector \vec{Q}_n :

$$\vec{Q}_n := \begin{pmatrix} a_n \\ b_n \end{pmatrix} \quad (5.4)$$

By the definitions of a_n and b_n , \vec{Q}_n can be rewritten in terms of $n\Psi_n$ which can be identified as the azimuthal angle of \vec{Q}_n :

$$\begin{aligned} \vec{Q}_n &= \begin{pmatrix} v_n \cos(n\Psi_n) \\ v_n \sin(n\Psi_n) \end{pmatrix} \\ \tan n\Psi_n &= \frac{\sin(n\Psi_n)}{\cos(n\Psi_n)} = \frac{v_n \sin(n\Psi_n)}{v_n \cos(n\Psi_n)} = \frac{b_n}{a_n} \end{aligned} \quad (5.5)$$

The final expression gives an indication on how to compute the event plane angle directly in the data, when we identify $f(\varphi)$ with the azimuthal particle distribution

of the given event. Thus a_n and b_n are just sums over all particles weighted with the sine or cosine of the particle's azimuthal angle:

$$a_n = \frac{1}{N} \sum_i \cos(n\varphi_i), \quad b_n = \frac{1}{N} \sum_i \sin(n\varphi_i) \quad (5.6)$$

By introducing weights into the sums of a_n and b_n it is possible to further increase the sensitivity of the measurement, and decrease the measurement errors [146, 149]. It was shown that the optimal choice of weights, maximising the measurement value, is given by the resulting measurement of $v_2(p_T)$ itself [146]. This circular dependence is of course highly unfortunate. A very rough approximation is however enough, and thus the following very simple parametrisation is usually used instead:

$$w_i(p_T) = \begin{cases} p_T & p_T < 2 \text{ GeV}/c \\ 2 & \textit{else} \end{cases}$$

5.2.2 Measuring Flow Relative to the Event Plane

Having calculated the event plane for each event we are now in the position of evaluating the Fourier series for all events, identifying $f(\varphi)$ now with the azimuthal particle distribution of all events:

$$f(\varphi) = \sum_n v_n \cos n(\varphi - \Psi_n)$$

Since the term in the cosine is completely determined for each particle, we can regard this expression as a Fourier series in its normal form, with all sine terms missing:

$$\sum_n v_n \cos(x)$$

Using the knowledge from the previous paragraph we can identify v_n as the Fourier parameter:

$$\begin{aligned} v_n &= \frac{1}{\pi} \int_{-\pi}^{\pi} f(\varphi) \cos(x) = \frac{1}{\pi} \int_{-\pi}^{\pi} f(\varphi) \cos n(\varphi - \Psi_n) = \\ &= \frac{1}{N} \sum_i \cos n(\varphi_i - \Psi_n) =: \langle \cos n(\varphi - \Psi_n) \rangle = v_n \end{aligned} \quad (5.7)$$

In contrast to the event plane determination (Equation 5.6) the sum now runs over all particles of all events.

5.2.3 Event Plane Resolution

Up to now, and especially so in Chapter 3, it was implicitly assumed that the event plane angle Ψ_n is perfectly determined. However in Equation 5.6 the sum runs over all the particles of one collision. Having only a finite number of particles in each event deteriorates the quality of the result, the less particles there are. Thus the event plane angle determined has an intrinsic statistical uncertainty due to the number of particles present in the event. This measured event plane angle Ψ'_n is off

by a value Δ of the real event plane angle Ψ_n , which could have been measured had there been an infinite number of particles in that same event: $\Delta = \Psi'_n - \Psi_n$. Thus instead of measuring $v_n = \langle \cos n(\varphi - \Psi_n) \rangle$ (Equation 5.7), the following is actually measured:

$$\langle \cos n(\varphi - \Psi'_n) \rangle = \langle \cos n(\varphi - (\Psi_n + \Delta)) \rangle$$

This can be simplified¹⁶ taking into account that different events have uncorrelated Ψ and Δ , which results in a factorisation of the averages, and that both Ψ and Δ are symmetrically distributed around 0 and thus $\langle \sin X \rangle = 0$:

$$\begin{aligned} \langle \cos(\varphi - (\Psi + \Delta)) \rangle &= \langle \cos \varphi \cos(\Psi + \Delta) + \sin \varphi \sin(\Psi + \Delta) \rangle = \\ &= \langle \cos \varphi (\cos \Psi \cos \Delta + \sin \Psi \sin \Delta) + \sin \varphi (\sin \Psi \cos \Delta + \cos \Psi \sin \Delta) \rangle = \\ &= \langle \cos \varphi \rangle (\langle \cos \Psi \rangle \langle \cos \Delta \rangle + \langle \sin \Psi \rangle \langle \sin \Delta \rangle) + \langle \sin \varphi \rangle (\langle \sin \Psi \rangle \langle \cos \Delta \rangle + \langle \cos \Psi \rangle \langle \sin \Delta \rangle) = \\ &= (\langle \cos \varphi \rangle \langle \cos \Psi \rangle + \langle \sin \varphi \rangle \langle \sin \Psi \rangle) \langle \cos \Delta \rangle = \langle \cos(\varphi - \Psi) \rangle \langle \cos \Delta \rangle \end{aligned}$$

The term $\langle \cos n\Delta \rangle$ is called the event plane resolution: $\sigma_{EP} := \langle \cos n\Delta \rangle$. Thus the result of Equation 5.7 can be recovered even if only Ψ'_n can be measured instead of Ψ_n , as long as σ_{EP} can be estimated:

$$v_n = \langle \cos n(\varphi - \Psi_n) \rangle = \frac{\langle \cos n(\varphi - \Psi'_n) \rangle}{\sigma_{EP}} \quad (5.8)$$

A way to estimate the event plane resolution is to separate the particles of each event in multiple groups (A, B,..) and measure the event plane angle for each of these groups ($\Psi'_{A,n}, \Psi'_{B,n}, \dots$). The Δ of each event is then estimated by comparing these subevent plane angles.

The simplest case is to take two equal subevents A and B, where $\Psi'_{A,n}$ and $\Psi'_{B,n}$ are measured. Equivalently to the event plane resolution we define the subevent plane resolution: $\sigma_{sEP,A} := \langle \cos n\delta \rangle$, where $\delta = \Psi'_{A,n} - \Psi_n$. But since the groups A and B are on an equal footing in average the same holds also for group B: $\sigma_{sEP,B} = \sigma_{sEP,A} = \sigma_{sEP}$. Thus we can write:

$$\sigma_{sEP}^2 = \langle \cos n\delta \rangle^2 = \langle \cos n(\Psi'_{A,n} - \Psi_n) \rangle^2 = \langle \cos n(\Psi'_{A,n} - \Psi_n) \rangle \langle \cos n(\Psi'_{B,n} - \Psi_n) \rangle$$

To this¹⁶ we can add appropriate sine terms since, due to the symmetry property of Ψ , these average to 0 as long as the subevents are uncorrelated:

$$\begin{aligned} \langle \cos(\Psi'_{A,n} - \Psi_n) \rangle \langle \cos(\Psi'_{B,n} - \Psi_n) \rangle &+ \overbrace{\langle \sin(\Psi'_{A,n} - \Psi_n) \rangle}^0 \overbrace{\langle \sin(\Psi'_{B,n} - \Psi_n) \rangle}^0 = \\ &= \langle \cos(\Psi'_{A,n} - \Psi_n) \cos(\Psi'_{B,n} - \Psi_n) + \sin(\Psi'_{A,n} - \Psi_n) \sin(\Psi'_{B,n} - \Psi_n) \rangle = \\ &= \langle \cos((\Psi'_{A,n} - \Psi_n) - (\Psi'_{B,n} - \Psi_n)) \rangle = \langle \cos(\Psi'_{A,n} - \Psi'_{B,n}) \rangle \\ &\Rightarrow \sigma_{sEP}^2 = \langle \cos n(\Psi'_{A,n} - \Psi'_{B,n}) \rangle \end{aligned}$$

¹⁶suppressing the n's due to the lack of space

Thus the subevent resolutions for both of the groups are equal and can very simply be measured by just averaging the cosine of the difference of those two subevent plane angles. The event plane resolution scales approximately with the particle multiplicity like $1/\sqrt{N}$ (see [90, 146]). Assuming that the groups A and B each divide the total event by half, we get:

$$\sigma_{EP} = \sigma_{sEP}\sqrt{2} = \sqrt{2 \langle \cos n(\Psi'_{A,n} - \Psi'_{B,n}) \rangle} \quad (5.9)$$

The deduction of the subevent resolution assumed that the subevents are uncorrelated by anything else than flow. This is not true in the presence of non-flow effects (Chapter 3.10). However, due to the fact that the correlation length of these effects is generally smaller than for flow, it is possible to suppress them by measuring the particles at very different pseudorapidities (η). For example by introducing an η -gap between the two subevents A and B.

When however it is not wished or not possible to define two equal subevents, because for example the detector itself is not symmetric, then it is necessary to define three subevents (A, B and C). These can then be arbitrarily distributed in space. It can be shown that the event plane resolution of detector A is then given by the three subevent resolutions σ_{sAB} , σ_{sAC} and σ_{sBC} :

$$\sigma_{EP,A} = \sqrt{\frac{\sigma_{sAB}^2 \sigma_{sAC}^2}{\sigma_{sBC}^2}}, \quad \sigma_{sXY} = \langle \cos n(\Psi'_{X,n} - \Psi'_{Y,n}) \rangle \quad (5.10)$$

5.2.4 Scalar Product Method

It has been shown that a slight variation of the above can further improve the sensitivity of the measurement, decrease the errors and increase its robustness in face of fluctuations [Adler2002, 151]. The determination of the v_n parameters (Equation 5.8) is changed by introducing a weight, which is the length of the event's flow vector (Equation 5.4):

$$v_n = \frac{\langle |\vec{Q}_n| \cos n(\varphi - \Psi'_n) \rangle}{\sigma_{SP}} = \frac{\langle \vec{Q}_n \cdot \vec{u} \rangle}{\sigma_{SP}} \quad (5.11)$$

Because of the properties of the scalar product, it is possible to write the expression as a scalar product of the flow vector \vec{Q}_n and the unit vector of each particle's azimuthal trajectory \vec{u} . The same is true for the denominator which corresponds to the event plane resolution (Equation 5.9). It can be written in terms of two subevent flow vectors as:

$$\sigma_{SP} = \sqrt{2 |\vec{Q}_{A,n}| |\vec{Q}_{B,n}| \langle \cos(\Psi'_{A,n} - \Psi'_{B,n}) \rangle} = \sqrt{2 \langle \vec{Q}_{A,n} \cdot \vec{Q}_{B,n} \rangle}$$

And in case it is not possible to define two equal subevents, it follows for the three subevents:

$$\sigma_{SP} = \sqrt{\frac{\langle \vec{Q}_{A,n} \cdot \vec{Q}_{B,n} \rangle \langle \vec{Q}_{A,n} \cdot \vec{Q}_{C,n} \rangle}{\langle \vec{Q}_{B,n} \cdot \vec{Q}_{C,n} \rangle}} \quad (5.12)$$

6 Inclusive Electron Measurement

This chapter discusses the measurement of the inclusive electron sample. The inclusive measurement determinates the electron spectra of all electrons. To get the electrons from heavy flavours only, the background electron spectra must be subtracted, this will be described later in the subsequent chapters.

6.1 Data Sample and Run Selection

The data sample used in this work is from the LHC data taking period LHC11h recorded by ALICE in fall 2011. Each data taking period takes roughly one month. During this time the data taking is split into separate runs. The length of each run is dependent on the running conditions of the experiment. A run can be as short as a few minutes and as long as many hours. A typical problem of the period were readjustments of the TPC high voltage, and hardware failures of the ITS.

After data taking, the run is saved and several quality assurance and calibration procedures are carried out. Any problems with data taking, quality assurance or calibration are saved in the run condition table. Only good runs are taken into account for this work's analysis. Additionally runs are also excluded when there is evidence for unusual detector behaviour. Figure 6.1 shows a comparison of runs with the usual TPC signal of the period and the signal of the additionally excluded runs. The runs included in the analysis are:

167987, 167988, 168310, 168311, 168322, 168325, 168341, 168342, 168361, 168362, 168458, 168460, 168464, 168467, 168511, 168512, 168514, 168777, 168826, 168988, 168992, 169035, 169040, 169044, 169045, 169091, 169094, 169099, 169138, 169144, 169145, 169148, 169156, 169160, 169167, 169238, 169411, 169415, 169417, 169418, 169419, 169420, 169475, 169498, 169504, 169506, 169512, 169515, 169550, 169553, 169554, 169555, 169557, 169586, 169587, 169588, 169590, 169591, 169835, 169837, 169838, 169846, 169855, 169858, 169859, 170027, 170040, 170081, 170083, 170084, 170085, 170088, 170089, 170091, 170155, 170159, 170163, 170193, 170203, 170204, 170207, 170228, 170230, 170268, 170269, 170270, 170306, 170308, 170309, 170311, 170312, 170313, 170315, 170387, 170388, 170572, 170593

The colour coding of this list indicates the magnetic field setup of the L3 magnet for the respective run: **blue** for negative field and **red** for positive field.

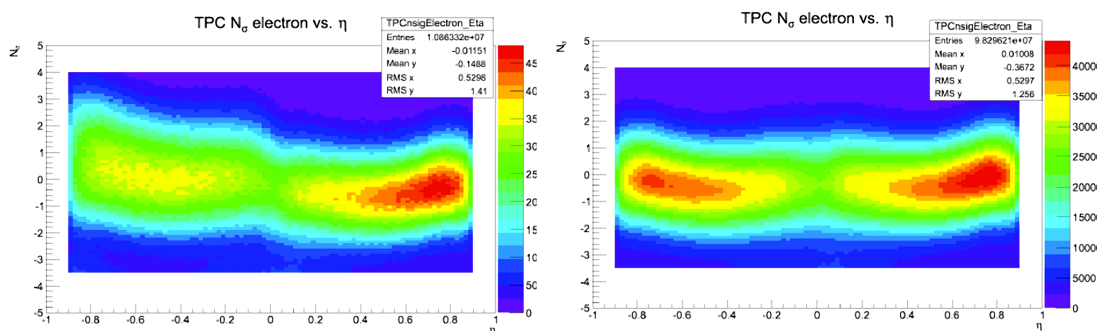


Figure 6.1: TPC signal of excluded runs (left) and of normal runs (right).

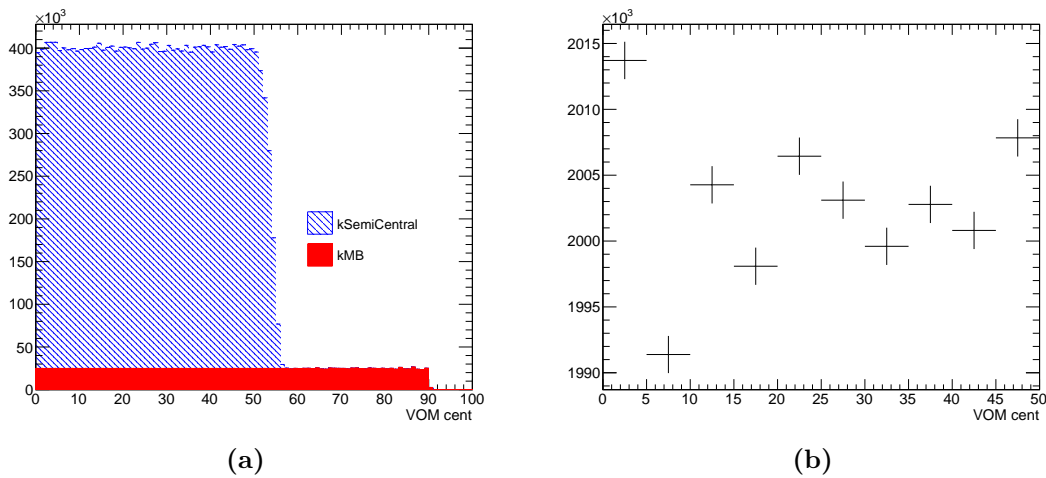


Figure 6.2: Centrality dependence of the number of events provided by the trigger setup (a) and the same quantity after all event cuts (b).

6.2 Event Selection

There are three main trigger scenarios used in this data sample: kCentral, kSemi-Central and kMB. The former two are centrality triggers imposing a minimum-multiplicity threshold for the V0 detector, while the latter is the minimum-bias trigger, which is activated whenever the following three conditions are met:

- a signal in two readout chips of the outer layer of the SPD
- a signal in the V0A
- a signal in the V0C

The purpose of the minimum bias trigger is to provide an event sample characterized by an as even as possible distribution of all event properties. For most analyses the amount of statistics provided by this trigger is however not enough. In this case and when there are certain centralities of interest the semi-central or central triggers provide a 10-fold or even higher increase in statistics. In this work the minimum bias and semi-central triggers have been used to provide a flat distribution of events in the considered centrality range (shown in Figure 6.2 a).

In order to avoid an asymmetric acceptance in the ITS, the position of the collision, the so-called primary vertex, must be inside a range of 10 cm from the nominal centre of ALICE. With a nominal bunch length of $\sigma_b = 7.55$ cm [93] this equals almost exactly 2 standard deviations of the vertex position distribution with a nominal width of $\sigma_z = \sigma_b/\sqrt{2} = 5.33$ cm.

6.2.1 Pile-Up Protection

Due to the intensity of the beam and the relatively long drift time of the TPC there is the possibility of an undetected second collision of other two nuclei. In this case the recorded event would include both collisions, while the tracks from

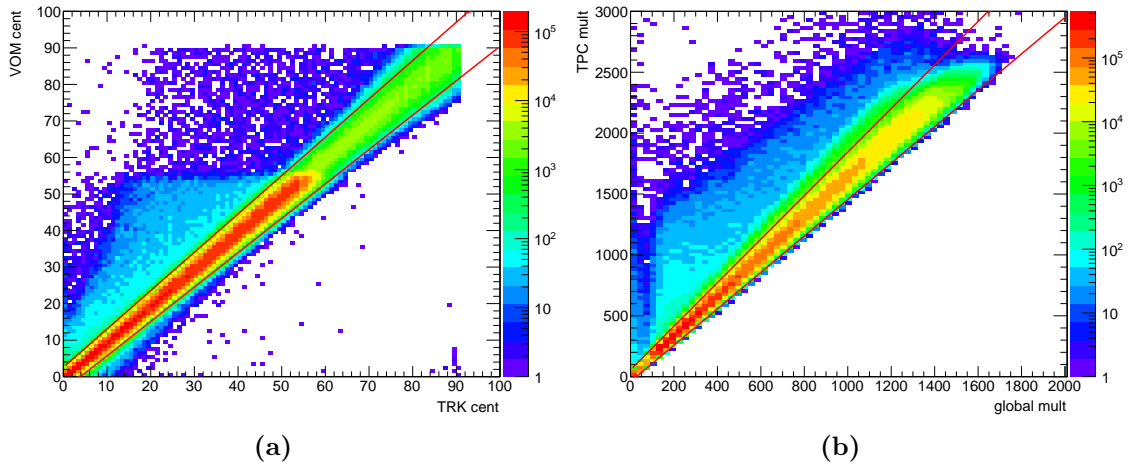


Figure 6.3: Correlation of the two centrality measures (a) and of the two track definitions (b) and the respective 3 sigma regions

the second collision would contaminate the tracks from the primary collision. This behaviour was analysed using correlations between two definitions of centrality and two definitions of found tracks.

The primary definition of the centrality percentile used throughout this work is based on the V0 detector (see also Figure 4.6). The second definition used for the correlation is based on the number of TPC tracks.

The second correlation analysed is comparing directly the number of tracks using two definitions: the number of standalone TPC tracks (AOD filter bit 1) and the number of global tracks with refits in TPC and ITS (AOD filter bit 16).

Both correlations are shown in Figure 6.3 together with the event cuts used. The cuts are based on linear fits of the bin-wise parameters of Gaussian fits of the sliced correlation plots including three standard deviations around the central region. It is important for the cut to be at a constant sigma value independently from the centrality, to not introduce a centrality dependence (see Figure 6.2 b).

6.3 Track Selection

The particle tracks which are considered to be electrons and are included in the analysis must have passed certain quality cuts. The first quality cuts are introduced by the data reduction mechanism. The whole raw data of the experiment is only saved temporarily. From the raw data the important properties of the particle trajectories are extracted and saved in the so-called ESD data sample. Since this data is still very large and can be processed only very slowly, the data is further compressed into the AOD data sample, by removing very low quality tracks. There are different samples of AOD data saved which can be chosen by setting a filter bit. The data sample used was AOD145 with filter bit 16. Additionally the following track cuts were applied:

Tracking

In order to predominantly select primary particles only tracks originating with a maximal distance of closest approach (DCA) to the primary vertex of the event where chosen.

All accepted tracks are required to have the tracking status bits “ITS refit” and “TPC refit” set. This indicates a successful termination of the Kalman filter tracking algorithm. To further increase the track quality, tracks with an increased fraction of clusters which are shared between multiple tracks were rejected as well as tracks with a low total number of assigned ITS and TPC clusters.

ITS Pixel Requirement

A very crucial cut for the analysis is the requirement of hits in the first two ITS layers, the pixel layers. Electrons are not only produced directly by decaying particles, but can also be produced by converting photons. Since gammas have many sources which are unrelated to the heavy flavour this work is interested in, it is important to decrease the amount of electrons produced in gamma conversions as much as possible. Requiring hits in the first two layers of the ITS radically reduces the amount of these electrons, since conversions are then only possible in the beam pipe, in part of the first pixel layer and in the air in between. However due to the huge amount of particles in the ITS pixel layers, there is the possibility that hits are wrongly associated to particle tracks, which are then included in the data sample although the electrons were actually produced in gamma conversions after the ITS pixel layers. The consequences of these so-called late electrons are studied in Chapter 7.6. The sources of gammas as well as the conversion into electrons are discussed in Chapter 7.

Summary of all track cuts:

- Pseudorapidity range: $|\eta| < 0.8$
- $DCA_{xy} < 1$ cm, $DCA_z < 2$ cm
- Rejecting tracks with kinks
- ITS requirements:
 - ITS refit status bit
 - At least 4 ITS clusters
 - A hits in both ITS pixel layers (kBoth)
 - χ^2 per ITS pixel ≤ 36
- TPC requirements:
 - TPC refit status bit
 - At least 110 TPC clusters
 - At least 80 TPC clusters used for PID
 - Fraction of TPC clusters shared between multiple tracks less than 10%

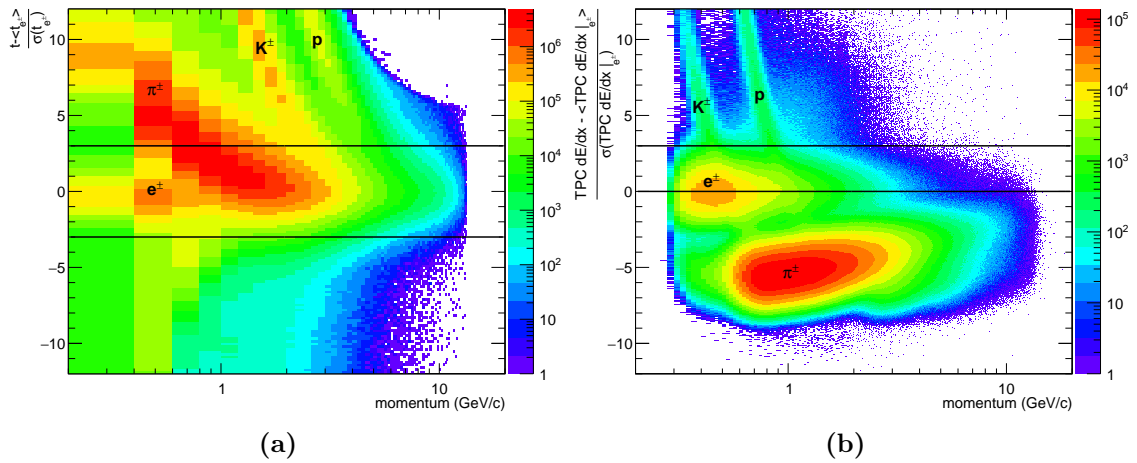


Figure 6.4: The PID cuts for the TOF (a) and the TPC (b)

6.4 Particle Identification

In this analysis particle identification (PID) effectively means electron identification, since these are the only particles of interest. The electrons are identified using the TPC and TOF detectors (Chapter 4.2.2).

6.4.1 TOF PID

The Time-Of-Flight detector measures the arrival time at which it is hit by charged particles with high precision (< 100 ps), relative to a start signal which is generated by the T0 detector. Figure 6.4 (a) shows the arrival times for all particles which passed the track quality cuts (Chapter 6.3) relative to the expected arrival time of electrons. Tracks are said to pass the TOF PID cut when their arrival time is within the region of three standard deviations around the electron expectation. It can be seen that the pions are merging into this region very early (< 1 GeV/c), while the kaons and protons enter this region only at around 2 GeV/c and 4 GeV/c respectively. To remove these pions, kaons and protons from the electron sample an additional PID cut is applied in the TPC.

6.4.2 TPC PID

The particle identification with the TPC is based on the Bethe-Bloch equation (Equation 4.2). Charged particles going through a gas will ionize the gas, losing energy per unit path length (dE/dx). This ionization energy is determined by the TPC by measuring the ionized charges along the track. Figure 6.4 (b) shows the measured TPC dE/dx for all particles which passed the track quality cuts and the TOF PID cut, relative to the expected energy loss of electrons. The pions can now be efficiently removed by rejecting anything with negative relative dE/dx.

It can be seen that there are still some kaons and protons visible in the low momentum region, even though in this momentum region the arrival time of the

particles is far more than 12σ away from the electron expectation in the TOF. This behaviour is evidence for a misassociation of TOF hits and TPC tracks. Apparently the TOF's high precision time measurement is deteriorated by a suboptimal choice of its spacial granularity. Any resulting contamination of the electron sample with unwanted particles is analysed in Chapter 6.6 and then subtracted from the final result of the inclusive electron measurement.

6.5 TPC Post-Calibration

Although the data sample used should actually be calibrated, it has turned out that in the case of the TPC, the calibration was not completely meeting the demands. As shown in Figure 6.5 (a) and (b), the mean of TPC signal has a drift with respect to the event multiplicity and shows a wiggle around the expectation when compared against the track's pseudorapidity. Both of which should in fact be flat. Additionally the units of the ordinate should exactly match the width of one standard deviation of the electrons' TPC signal, which is not exactly the case. Especially the departure of the mean from the expectation is problematic since the TPC PID cut is supposed to cut exactly there. A systematic departure means unnecessarily increasing the pion contamination or cutting into too much of the electrons.

Since the multiplicity of an event is completely uncorrelated to the track pseudorapidity it is possible to correct the two effects mostly independently. The only interconnection between the two corrections is that both move the same quantity and thus correcting both effects in one go would actually produce an overcorrection. Thus an iterative approach was used were first the wiggle against the track pseudorapidity is corrected for and then, after a repeated analysis step of the pseudorapidity corrected data, the multiplicity drift.

The correction is done by first selecting a momentum range where the electrons are best separated from the other particles. The momentum range used was at around $0.75 \text{ GeV}/c$. As shown in Figure 6.4 (b) the distance of the electrons to the pions is almost at its maximum, while the kaons and protons are sufficiently far away, and the total amount of electrons is still very high. Vertical slices of the histograms shown in Figure 6.5 (a) and (b) are fitted with an appropriate distribution function in the electron range. A good description is provided by a slightly skewed version of the Gaussian distribution (see Chapter 10.4 for details). A typical fit of the TPC signal of such a single multiplicity bin with this distribution is shown in Figure 6.5 (c). The mean and sigma extracted from the fits of the momentum and pseudorapidity slices are plotted in Figure 6.5 (d) and (e). These plots are then finally fit with an appropriate function, which is a linear function in case of the multiplicity drift and a multi-trigonometric function in case of the eta dependence. These fits are then introduced as a correction for the data, processed during the data analysis.

6.6 Contamination

It is of utmost importance to have a clean electron sample. Significant contamination of the electron sample with other particles can influence the results. Thus, at least

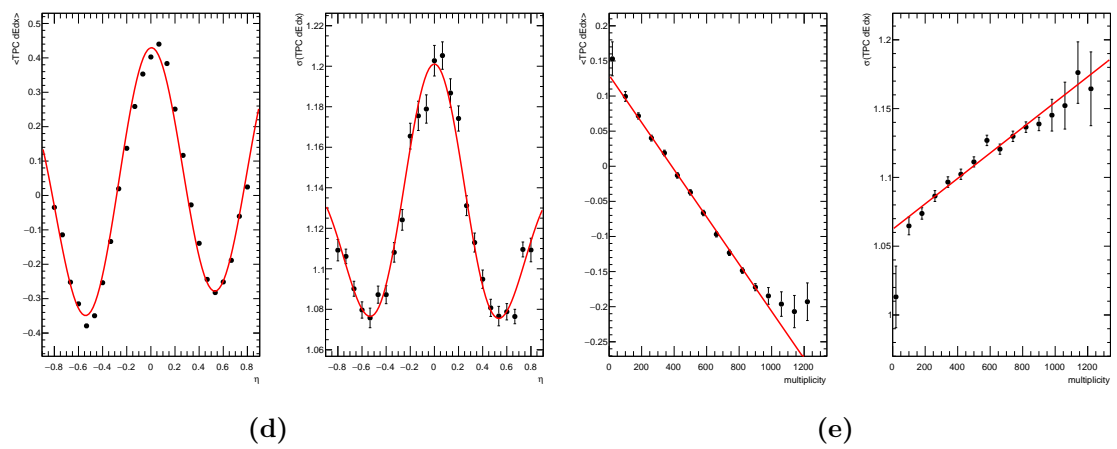
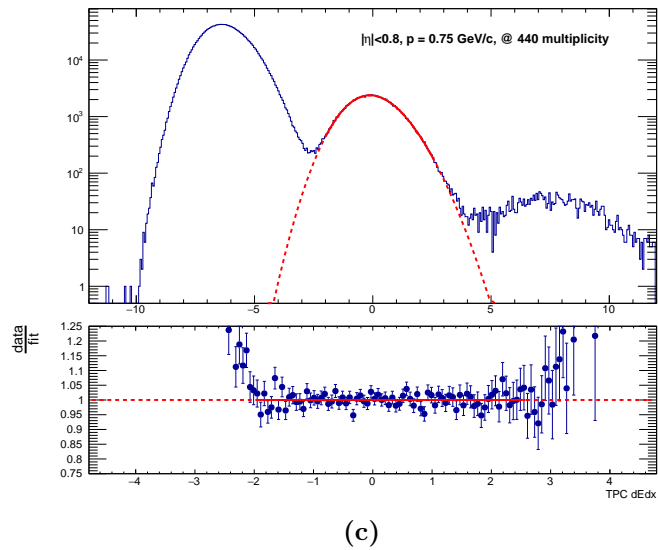
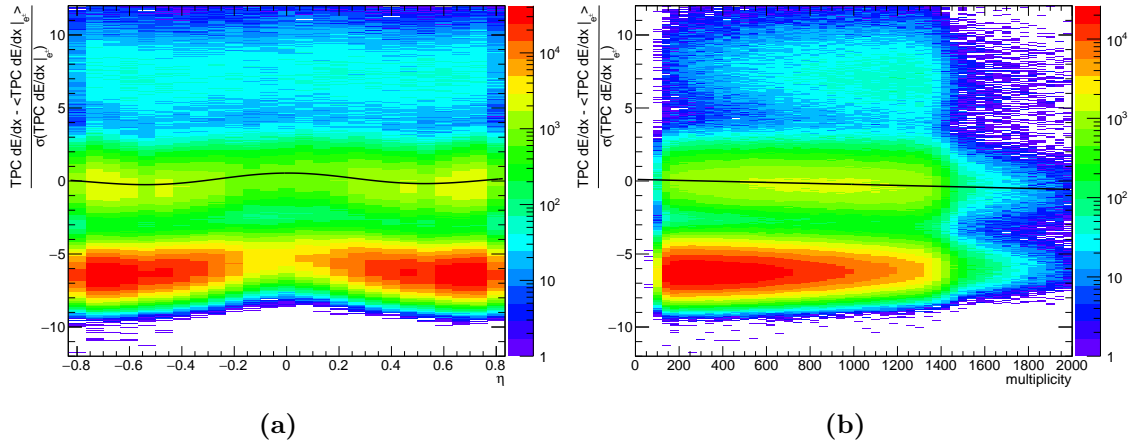


Figure 6.5: Dependency of the TPC signal against pseudorapidity (a) and track multiplicity. Typical bin-wise fit of the TPC signal in the electron range (c). Fit of the bin-wise fit parameters (d) and (e).

from a quality assurance point of view, the contamination of the electrons must be checked. It is clear from Figure 6.4 that there must be some degree of contamination left even after the last PID cut in the TPC.

The contamination C of a given particle species j at a given momentum bin p is calculated by fitting the signals s of all the individual particle species i in the final PID detector with an appropriate distribution function $f_i(s)|_p$ and compare the integrals of the distributions in the PID cut range of this detector. In this case, this detector is the TPC with a signal range of [0..3]. Thus the purity P of a given particle species j is given by:

$$1 - C_j(p) = P_j(p) = \frac{\int_0^3 f_j(s)|_p ds}{\sum_i \int_0^3 f_i(s)|_p ds} \quad (6.1)$$

The distribution function used to fitting the TPC signals is, as in Chapter 6.5, a skewed Gaussian for the electrons, protons and kaons. For the pions an even more general distribution is used: a “variakurtic” skewed Gaussian (see Chapter 10.4 for details). In contrast to what has been done in the TPC post-calibration, not only must now all the particle species be fitted but this also has to be done at all momenta. This is a much more demanding task, since at certain momenta the particles’ TPC signals overlap (see Figure 6.4). To further complicate the situation, not the bulk of the distributions is of interest but their tails, which are also mostly overlapping between the particles.

6.6.1 Clean Samples

The procedure to find the appropriate distribution function is greatly helped when the particle signals can be analysed separately, without the overlaps. At the expense of a reduced statistics it is possible to identify pions, protons and electrons by using a kinematic technique. For this, so-called V^0 candidates are identified. These are short-lived neutral particles decaying into two inversely charged long-lived particles. These are identified by tracking all unlike-charged particle pairs, and selecting all with a maximal closest distance and with a total momentum originating next to the events primary vertex.

Particles with such a topology are γ , K_S^0 , Λ and $\bar{\Lambda}$, with the following decay channels:

- $\gamma \rightarrow e^+e^-$
- $K_S^0 \rightarrow \pi^+\pi^-$
- $\Lambda^0 \rightarrow \pi^-p$ and $\bar{\Lambda}^0 \rightarrow \pi^+\bar{p}$

Armenteros and Podolanski [152] have shown that it is possible to discriminate between these mother particles by the virtue of two kinematic variables: the transverse momentum of the decay particles relative to the mother (q_T) and the longitudinal momentum asymmetry α :

$$\alpha = \frac{q_L^+ - q_L^-}{q_L^+ + q_L^-}$$

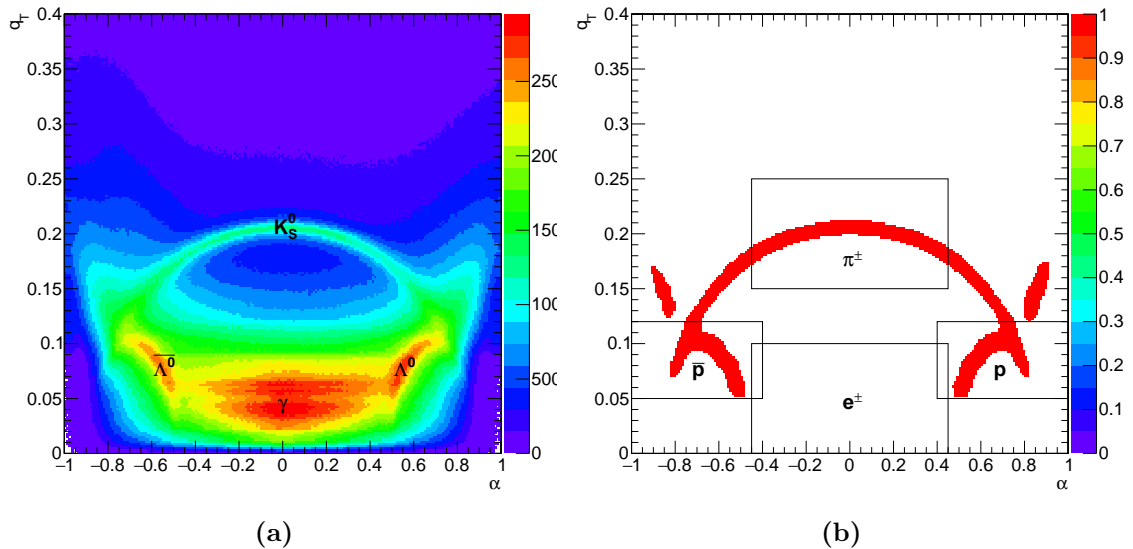


Figure 6.6: The Armenteros-Podolanski plot is used to create the clean samples. (a) is the raw plot, (b) is contrast-enhanced version used for selecting the particles.

Figure 6.6 shows the so-called Armenteros-Podolanski plot of the two variables. The initial plot (a) has been processed to enhance the contrast reaching the final binary decision plot (b), used to decide whether a V^0 candidate is accepted. This is done using methods known from image processing for detecting regions of interest. The algorithm implemented uses the principles of the so-called Laplacian of the Gaussian method (see Chapter 10.5 for details). Candidates in the marked regions produce the clean TPC signal samples.

The charged-kaon clean samples needed for the very low momentum region were produced using a very tight TOF cut of one standard deviation. The remaining contamination is in this case higher than for the other particles. Like e.g. in case of the protons where the pions are also produced in the Λ decays and are selected by the same cut as the protons. However in the needed momentum range of the respective clean samples, each is still clearly distinguishable in the TPC signals.

6.6.2 Fitting of the TPC signals

The key to fitting the TPC signals of all particle species over the whole momentum range is to realize that the momentum bins are highly correlated. Going from one momentum bin to the next, will barely change the distribution of the TPC signals. In an iterative method it is thus possible to first fit the particle signals in non-overlapping momentum regions, use robust fits on the distribution parameters to denoise them in the observed range and to interpolate or extrapolate to an extended range for the next iteration.

Depending on the parameter different robust fits have been used: Since the mean position and width of the electron signals has already been corrected in Chapter 6.5, a simple constant fit was enough. The mean positions of the other particles can be fitted with variations of the Bethe-Bloch equation (Equation 4.2). It turned out

that the skewness of all the particle distributions, apart from the pion, is momentum independent and can be fit with a constant. For the pion a log-linear fit was used. The scales of the distributions were fitted with splines using a custom made interface library to the cubic spline curve fitting capabilities of the ALGLIB C++ library¹⁷ performing a penalized spline regression.

Due to the bin-wise fitting of the distributions to the TPC signal, the distribution parameters have a natural statistics jitter. In the overlapping momentum regions there can be very significant false departures due to unavoidable ambiguities in individual momentum bins. Of course, due to the high correlation of the momentum bins, the distribution parameters should in fact change only very smoothly throughout the whole momentum range. This is guaranteed by an iterative procedure, where each iteration itself is a multi-step procedure: In each momentum bin the particle species signals are first individually fit using fitting parameters of the previous bin, as well as the clean samples of the particle signals as seeds. This is followed by a joined fit of all particles distributions. This is repeated for all momentum bins. An iteration ends after fitting the last momentum bin with the smoothing of the bin-wise parameters. This smoothing is based on a robust fit of each of the distribution parameters. The robust fitter used is described in Chapter 10.6. In each iteration, more and more parameters are being fixed and the momentum range is increased also into the overlapping regions.

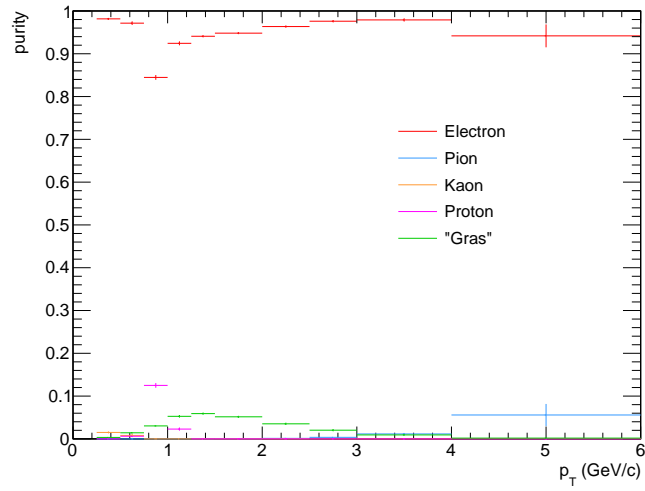
6.6.3 Contamination Results

Based on the parameters extracted by fitting the TPC signals, it is possible to calculate the electron purity for each momentum bin by evaluating Equation 6.1. Figure 6.7 shows the results of the contamination analysis. The protons cross the electron band at around 1 GeV/c, and towards the high end of the range, the pions come ever closer. From about 0.5 GeV/c to 3 GeV/c, there is an additional component, which can be seen more clearly in the plot of the function fits (b) as an enhancement on the right side of the electron signal. It will be referred to as “gras”. This seems to originate from tracks with wrongly merged clusters. As most of the particles produced are pions, it is safe to assume that pions also represent the majority of this contribution.

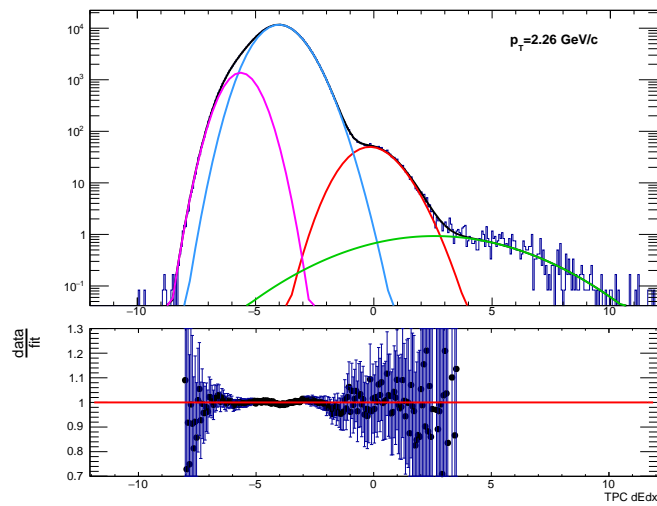
6.7 Event-Plane Flatness

Following the discussion in Chapter 5.2.1 the event plane is an important ingredient for the flow measurement. The detector used for the event plane determination is the V0 detector. It consists of two subdetectors at two opposite points in forward and backward direction around the interaction point (see also Chapter 4.2.3). Its pseudorapidity coverage places the V0 detector at a very different position in phase space compared to the central barrel which is at mid-rapidity. The fact that the analysis uses particles reconstructed by the central barrel detectors, can be exploited by using the V0 detector for the event plane determination thus suppressing non-flow effects (see Chapter 3.10).

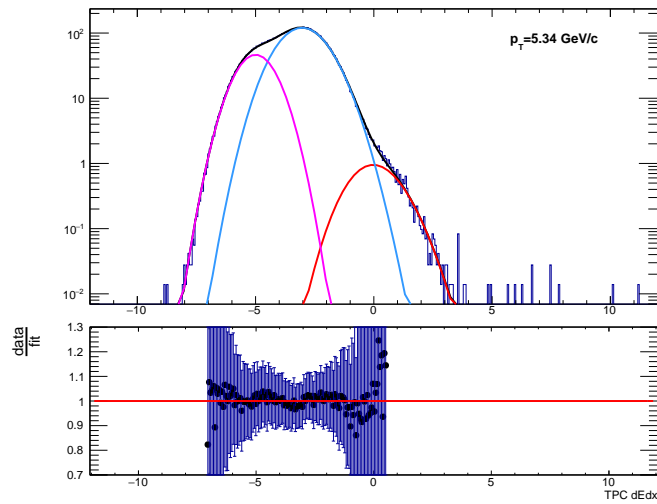
¹⁷<http://www.alglib.net/>



(a)



(b)



(c)

Figure 6.7: Purity of the electron sample, and the composition of the contamination (a). Also shown are examples of the fits used to evaluate the contamination at two momenta (b, c).

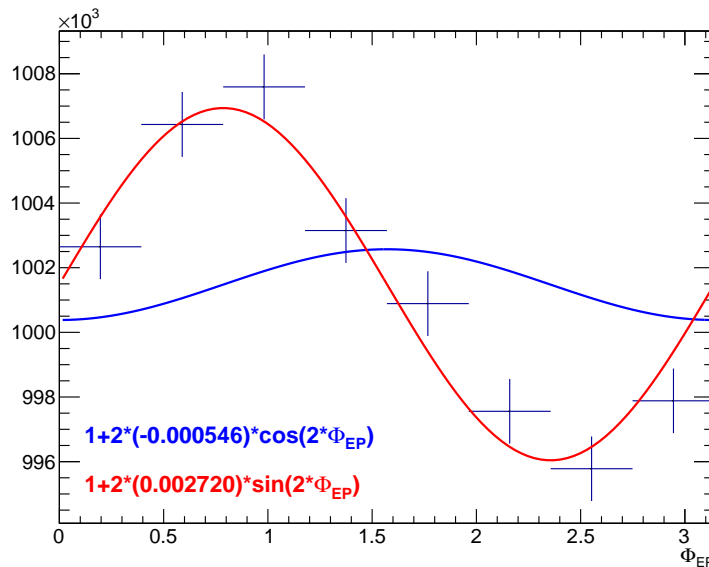


Figure 6.8: The distribution of the event-plane angle is already very flat so that it does not influence the flow measurement.

The event plane is defined by the position of the two colliding nuclei. Since this positioning is completely random, for a full azimuth acceptance detector with perfect alignment and calibration the distribution of the event plane angle should be perfectly flat for a large data set. It is crucial to check this property, since deviations would contribute to a fake measurement of flow. Figure 6.8 shows the distribution of the reconstructed event plane angle and its contribution to the components of the flow vector \vec{Q} (see Equation 5.4). The deviation from perfect flatness is around two orders of magnitude lower than the expected amount of true flow, making a correction unnecessary.

6.8 Event-Plane Resolution

An important ingredient to a flow measurement is the determination of the event-plane resolution. As discussed in Chapter 5.2.3 the resolution is limited not only by the detector resolution, but also due to the number of particles present in the event at hand. Had the same event included more (or less) particles, the resolution would have been better (worse).

The two halves of the V0 detector, V0A and V0C, are taken together to determine the event plane. Since these two subdetectors have an asymmetric pseudorapidity coverage in forward and backward direction (see Chapter 4.2.3) it is not possible to divide the total event in two equal subevents. It is thus necessary to include a third detector to determine the resolution (see Chapter 5.2.3) which is then calculated by the three-subevents method (Equation 5.10). The third detector included is the TPC. Since this is the very detector used for the analysis, care must be taken to remove analysed particles from the sample to not contaminate the result with autocorrelations. Since the data of both V0A and V0C are taken together for

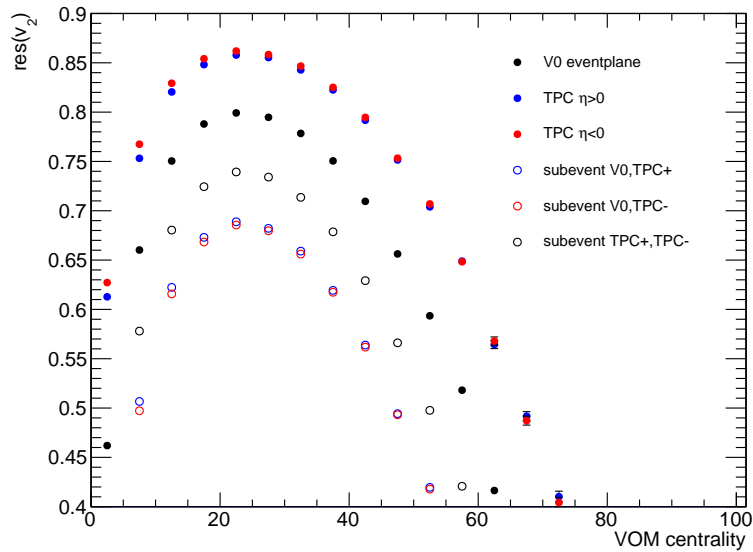


Figure 6.9: Event plane resolution of the three subdetectors and the subevent resolutions for all combinations. Due to its coarser granularity the V0 has a lower resolution than the TPC.

the event plane determination, the V0 must be taken as one of the three needed subevents and the V0A and V0C cannot be separated. The other two subevents are then the forward and backward halves of the TPC. Figure 6.9 shows the subevent plane resolution of the three subdetector combinations and the resulting event plane resolutions.

6.9 Inclusive Electron Flow

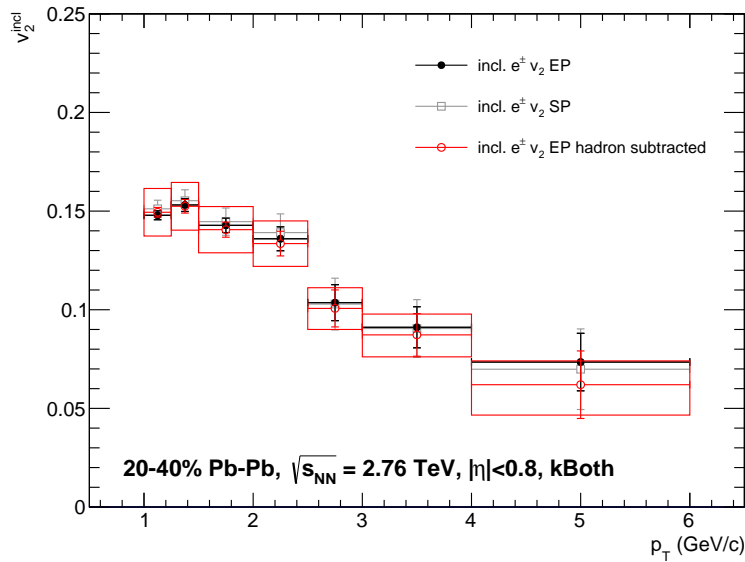
Figure 6.10 (a) shows the v_2 extracted from the inclusive electron sample analysed. Due to the hadron contamination and the available statistics, the momentum range of the analysis was restricted to $1 - 6 \text{ GeV}/c$. The repeated analysis using the scalar product method is showing a result consistent with the event plane method.

The systematic uncertainty (Figure 6.10 b) is the result of combining the following sources of uncertainty:

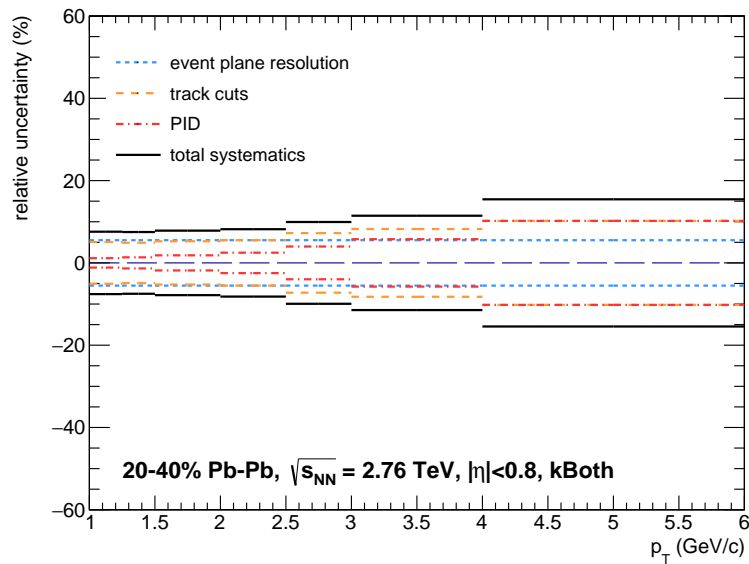
- variations of the tracking cuts (± 0.0075 units v_2)
- variations of the PID cuts (up to ± 0.0075 units v_2)
- the measured variation of the event plane resolution inside the centrality bin ($\pm 5.5\%$)

Checks of systematic deviations due to the field polarity and the particle charge yielded no significant changes outside the statistical uncertainty.

The subtraction of the hadron contamination is performed using Equation 5.1, while R_{SB} is here the ratio of the amount of electrons to the amount of contamination. The hadron contamination was subtracted according to the pion elliptic flow



(a)



(b)

Figure 6.10: Inclusive electron elliptic flow (a). The systematic uncertainty and the contributions to it (b). The figures of the other centralities analysed are attached in the appendix (Figure 10.1 and Figure 10.2).

measurement presented in Chapter 7.3 (and shown in Figure 7.5). The different sources of uncertainty together with the uncertainty on the amount of contamination and on the pion spectrum are propagated using a numerical estimation of the second order approximation to the full propagation (see Chapter 10.7 for details).

7 Background Electron Cocktail

The previous chapter describes how the inclusive electron measurement has been performed. To extract the heavy-flavour electrons from the inclusive electron measurement, the so-called background has to be subtracted. This chapter shows how the background is evaluated.

The background electrons would ideally comprise all unwanted electrons which cannot be rejected in the inclusive measurement. Of interest are electrons from heavy hadrons in this work. Thus, the other main electron sources that need to be subtracted are leptonic and semi-leptonic decays of light mesons and conversions of decay and direct photons. The method used to subtract these electrons from the inclusive measurement is based on the so-called cocktail subtraction method (see Chapter 5.1).

In this method the background is simulated by calculating the decay kinematics of all the unwanted electron sources into electrons. Each source particle (also called mother particle) is generated in a Monte Carlo event generator, based on measured mother particle spectra. The electrons generated by the simulated decay kinematics are then mixed together into the electron cocktail, which is then subtracted from the inclusive measurement.

The simulation which was implemented for this work is based on a simulation of the following sources:

- Dalitz decays of π^0 , η , ω , η' , ϕ
- Leptonic decays of η , ρ^0 , ω , η' , ϕ
- Conversions of decay photons from π^0 , η , ρ^0 , ω , η'
- Conversions of real prompt and thermal photons
- Virtual prompt and thermal photons

The input to the simulation are the source particle p_T and v_2 spectra, which in the case of the mesons are entirely based on the ALICE measurements of charged pions (π^\pm).

7.1 Virtual Photon Production

Photons, and especially virtual photons are an important contribution to the cocktail. Thus it is important to understand their production channels.

Whenever a photon is produced by a source, it would have been instead possible for the source to have produced an electron-positron pair under certain circumstances. In the theory the production of an electron-positron pair is treated by allowing the photon source to not only produce the photons at their specific mass ($m_\gamma=0$), but of any mass. Particles produced at a different mass than their usual mass are called off-shell particles or virtual particles. The difference in mass between the particle produced and the specific unique mass a real particle of this type has is called virtuality. According to Equation 2.7 the mass of a particle fixes the relation of energy to momentum. Raising the precondition of a specific mass basically

means that the particle source is allowed to produce the particle with uncorrelated energy and momentum. Since real particles of a specific type always have an unique mass, the particles produced at different masses must somehow lose this virtuality (additional mass).

For a high energy photon source, this means that the produced photons can be so massive that they immediately decay into electron-positron pairs. A very significant publication on this topic is from Kroll and Wada [153]. The number of virtual photons $N_{\gamma_{ee}^*}$ of mass $m_{\gamma_{ee}^*}$ decaying into a pair of electrons each of mass m_e per real photon N_γ is given by:

$$\left(\frac{1}{N_\gamma} \frac{dN_{\gamma_{ee}^*}}{dm_{\gamma_{ee}^*}} \right)_{\text{free}} = \frac{2}{3\pi\alpha} \frac{1}{m_{\gamma_{ee}^*}} \left(1 + 2 \left(\frac{m_e}{m_{\gamma_{ee}^*}} \right)^2 \right) \sqrt{1 - 4 \left(\frac{m_e}{m_{\gamma_{ee}^*}} \right)^2} \quad (7.1)$$

This expression is 0 for $m_{\gamma_{ee}^*} < 2m_e$, because a pair production needs at least the energy equivalent to the masses of the particles to be produced. For $2m_e < m_{\gamma_{ee}^*} < 3m_e$ the function increases almost “vertically” until it levels off and drops for higher masses as $1/m_{\gamma_{ee}^*}$. We see in the expression that the probability of a virtual photon scales with $1/\alpha$, which is a direct consequence of the QED Lagrangian. Although being thus two orders of magnitude below the number of real photons, the electrons of both, real and virtual photons, compete because the conversion of real electrons introduces the same factor $1/\alpha$.

The total number of virtual photons (and thus the number of real electron-positron pairs) is then given by integrating the above formula over all masses. However any attempt of doing so immediately fails with the integral diverging. If this rather surprising result had been true, it would have meant that every photon source produced an infinite number of electron-positron pairs. With a reassuring glimpse towards the lamp standing next to us, the expression obviously is still missing an important constraint.

Virtual photons, or in general virtual particles, are called virtual because they are the hypothetic particles needed to explain the propagation of the forces within the quantum field theories. In principle we could even completely skip the virtual photon stage, and view the above expression just as a statement on the production of electron pairs of a given invariant mass (Equation 2.8) per real photon. This invariant mass however is an other way of giving the electron pair a specific centre of mass energy. Viewed from this perspective it is not that surprising at all anymore that the first attempt to integrate must have failed. The omission of course was that a lamp cannot produce more energy than it has power, and that a particle cannot decay into something more massive than itself. In case we have a total energy constraint E_{max} , the above formula must thus read:

$$\left(\frac{1}{N_\gamma} \frac{dN_{\gamma_{ee}^*}}{dm_{\gamma_{ee}^*}} \right)_{E_{max}} = \left(1 - \left(\frac{m_{\gamma_{ee}^*}}{E_{max}} \right)^2 \right)^3 \cdot \left(\frac{1}{N_\gamma} \frac{dN_{\gamma_{ee}^*}}{dm_{\gamma_{ee}^*}} \right)_{\text{free}} \quad (7.2)$$

This additional factor suppresses the function towards E_{max} . In case of a particle P decaying, the energy constraint is given by the particles rest mass: $E_{max} = m_P$. When we have a given particle decaying into photons, the above expression is only true in case of exactly point-like particles. For particles of finite size, the expression

must be corrected by multiplying it with the so-called form factor $F(q)$, which is the Fourier transform of the spatial charge distribution:

$$\left(\frac{1}{N_\gamma} \frac{dN_{\gamma_{ee}^*}}{dm_{\gamma_{ee}^*}} \right)_P = F_P(m_{\gamma_{ee}^*}) \cdot \left(\frac{1}{N_\gamma} \frac{dN_{\gamma_{ee}^*}}{dm_{\gamma_{ee}^*}} \right)_{E_{max}=m_P} \quad (7.3)$$

The relevant decay channel where virtual photons play a major role, is the variant of the two photon decay, where one of the photons is replaced by a virtual photon. This decay channel is called Dalitz decay, and is significant for this work for π^0 , η and η' mesons. To sufficient precision, the form factor for a particle P can be written as:

$$F_P(q) = \frac{1}{1 + \frac{q^2}{\Lambda_P^2}} \quad (7.4)$$

The relevant particle-dependent scale Λ_P , is also related to the so-called slope parameter b_P or to the geometrical size of the particles charge radius: $\Lambda_P^2 = m_P^2/b_P = 6\hbar^2 c^2 / \langle r_P^2 \rangle$ [154–156]. Some of the more recent measurements with the smallest uncertainties on the parameters are currently: $\langle r_\pi^2 \rangle = 0.431 \pm 0.013 \text{ fm}^2$ [154, 156, 157], $\Lambda_\eta^{-2} = 1.95 \pm 0.18 \text{ GeV}^{-2}$ [154, 156, 158, 159] and $b_{\eta'} = 1.30 \pm 0.16$ [154, 156, 159].

7.1.1 Numerical Considerations

During the simulation of the background electrons, it is necessary to compute the number of virtual photons per real direct photon for a given global energy constraint. For this the following integral over Equation 7.2 must be computed:

$$N_{\gamma_{ee}^*} = \int_0^\infty dm_{\gamma_{ee}^*} \left(\frac{1}{N_\gamma} \frac{dN_{\gamma_{ee}^*}}{dm_{\gamma_{ee}^*}} \right)_{E_{max}} = \int_{2m_e}^{E_{max}} dm_{\gamma_{ee}^*} \left(\frac{1}{N_\gamma} \frac{dN_{\gamma_{ee}^*}}{dm_{\gamma_{ee}^*}} \right)_{E_{max}} \quad (7.5)$$

While this integral does have a closed-form solution, it is not exactly a short, fast to evaluate, expression. And since it must be evaluated in a relatively big numerical range, it is also of questionable numerical stability. The situation can be massively improved by including knowledge about the physics of the problem into the expression.

The first observation is that at high $m_{\gamma_{ee}^*}$ Equation 7.1 has a very simple asymptotic behaviour. In this case, high means $m_{\gamma_{ee}^*} \gg m_e$, which is the same as $m_e \rightarrow 0$:

$$a(m_{\gamma_{ee}^*}) = \lim_{m_e \rightarrow 0} \left(\frac{1}{N_\gamma} \frac{dN_{\gamma_{ee}^*}}{dm_{\gamma_{ee}^*}} \right)_{\text{free}} = \frac{2}{3\pi\alpha} \frac{1}{m_{\gamma_{ee}^*}} \quad (7.6)$$

The asymptote has a very simple integral. We will use its integral instead of the full expression and tweak the integration limits such that the result corresponds to the integration over Equation 7.2. This works, because the function is below its asymptote in the whole range. The factor distinguishing Equation 7.1 from Equation 7.2 acts only at high $m_{\gamma_{ee}^*}$ suppressing the function towards E_{max} . And thus the high mass behaviour of Equation 7.2 can be expressed by directly applying this factor to the asymptote a . For the integral over the function this suppressing effect can be

simulated by moving the upper limit of the integration towards smaller masses by some fraction x :

$$\int_{2m_e}^{E_{max}} a(m_{\gamma_{ee}^*}) \cdot \left(1 - \left(\frac{m_{\gamma_{ee}^*}}{E_{max}}\right)^2\right)^3 dm_{\gamma_{ee}^*} \stackrel{!}{=} \int_{2m_e}^{x \cdot E_{max}} a(m_{\gamma_{ee}^*}) dm_{\gamma_{ee}^*}$$

$$\Rightarrow x = \exp\left(-\frac{11}{12} + \text{Polynom}_3\left(\frac{m_e^2}{E_{max}^2}\right)\right)$$

$$\text{upper limit} = \lim_{m_e \rightarrow 0} (x) \cdot E_{max} = \exp\left(-\frac{11}{12}\right) \cdot E_{max}$$

In the same limit as before ($m_e \rightarrow 0$) the third degree polynomial vanishes, and the upper limit of the integration over a must thus be $\exp(-11/12) \cdot E_{max}$ such that it equals the integration over a in the whole range including the suppressing factor.

Of course the electron mass is actually not 0. For this to be corrected for the lower limit of the integration must now be moved. This new lower limit can be found by requesting that the integral over the asymptote matches the integral over the whole function:

$$\int_L^{\exp(-\frac{11}{12}) \cdot E_{max}} a(m_{\gamma_{ee}^*}) dm_{\gamma_{ee}^*} \stackrel{!}{=} \int_0^\infty dm_{\gamma_{ee}^*} \left(\frac{1}{N_\gamma} \frac{dN_{\gamma_{ee}^*}}{dm_{\gamma_{ee}^*}}\right)_{E_{max}}$$

$$\Rightarrow L = L(m_e^2, E_{max}^2)$$

The resulting lengthy algebraic expression for L can be simplified under the assumption that $E_{max} \gg m_e$. Under this assumption E_{max} diverges relative to a given finite m_e :

$$\text{lower limit} = \lim_{E_{max} \rightarrow \infty} L = \exp\left(\frac{5}{6}\right) \cdot m_e$$

Thus the approximation to the full integral is given by:

$$N_{\gamma_{ee}^*} \approx \int_{\exp(\frac{5}{6}) \cdot m_e}^{\exp(-\frac{11}{12}) \cdot E_{max}} a(m_{\gamma_{ee}^*}) dm_{\gamma_{ee}^*} = \frac{4 \log \frac{E_{max}}{m_e} - 7}{6\pi\alpha} \quad (7.7)$$

This approximation is usable for $E_{max} > 10 \text{ MeV}$ starting with an error of 2%, and dropping very steeply by more than 20 dB per decade. Figure 7.1 shows a comparison of this approximation to the full calculation.

The number of needed virtual photons is not the only parameter that has to be computed during the simulation. The other value needed for the virtual photons is the mass assigned. This must be drawn from a distribution according to Equation 7.2. The method used is the so-called rejection sampling and is shortly introduced in Chapter 10.3. It requires an envelope to the distribution, with the obvious candidate being the asymptote a from Equation 7.6. Its integral is given by:

$$A(x) = \int_{2m_e}^x a(m_{\gamma_{ee}^*}) dm_{\gamma_{ee}^*} = \frac{2 \log \frac{x}{2m_e}}{3\pi\alpha}$$

And the enveloping cumulative distribution E is then:

$$E(x, E_{max}) = A(x)/A(E_{max})$$

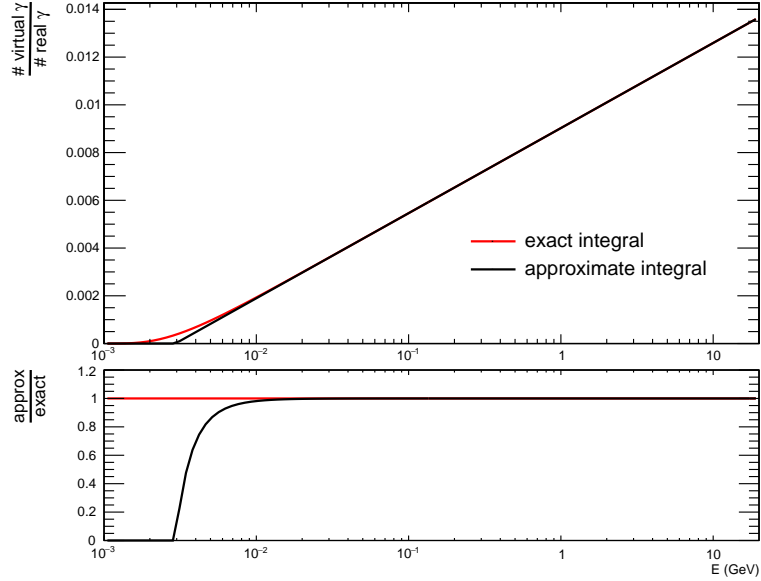


Figure 7.1: The virtual photon production is increasing with the energy due to the increasing volume of phase space the generated lepton pair can populate. For performance reasons, the expression used to compute the amount of virtual photons needed (Equation 7.7) is an approximation to the full calculation (Equation 7.5).

With the also needed inverse of the cumulative distribution being:

$$E^{-1}(y, E_{max}) = 2m_e \left(\frac{2m_e}{E_{max}} \right)^{-y}$$

7.1.2 Dalitz Decay Branching Ratios

The branching ratios of the relevant background electron sources into electrons are of utmost importance. However, not only decays into electrons are important, equally important are high-probability decays into photons, since photons can convert into electron pairs, when going through the detector material. For some particles, like the pion, the branching ratios are very precisely measured, for others, the results are less exact, and for some particles the relevant branching ratios are not available at all. The situation is especially bad for the η' , where one of the most important decay channels into electrons, the Dalitz decay, is measured only up to an upper bound. It is however possible to calculate a prediction for the branching ratio using the expression provided by Kroll and Wada (Equation 7.3 and Equation 7.4). Doing this for particles where the Dalitz decay is measured provides a possibility to test how well the virtual photon calculations compare to measurements. The measured branching ratios are taken from the PDG publications [15].

Having calculated the probability $p_{\gamma_{ee}^*|P}$ of a virtual photon electron-positron pair per real photon by integrating over Equation 7.3 for the particle P , it is possible to calculate the branching ratio of the Dalitz decay $BR(P \rightarrow \gamma e^+ e^-)$ in relation to the given branching ratio of the two-photon decay $BR(P \rightarrow 2\gamma)$. This is done by viewing $p_{\gamma_{ee}^*|P}$ as the probability of a Bernoulli trial for each of the two photons to be a virtual photon. The total probability of having k virtual photon electron-positron

	π^0	η	η'
$BR_{PDG}(\rightarrow 2\gamma)$	$(98.823 \pm 0.034) \%$	$(39.41 \pm 0.20) \%$	$(2.20 \pm 0.08) \%$
$BR_{PDG}(\rightarrow \gamma e^+ e^-)$	$(1.174 \pm 0.035) \%$	$(6.9 \pm 0.4) \cdot 10^{-3}$	$< 9 \cdot 10^{-4}$
$BR_{PDG}(\rightarrow 2(e^+ e^-))$	$(3.34 \pm 0.16) \cdot 10^{-5}$	$(2.40 \pm 0.22) \cdot 10^{-5}$	—
$p_{\gamma_{ee}^* P}$	$(5.9146 \pm 0.0004) \cdot 10^{-3}$	$(7.90 \pm 0.02) \cdot 10^{-3}$	$(8.59 \pm 0.03) \cdot 10^{-3}$
$B(2, p_{\gamma_{ee}^* P}, 0)$	$(98.8206 \pm 0.0001) \%$	$(98.426 \pm 0.003) \%$	$(98.17 \pm 0.02) \%$
$B(2, p_{\gamma_{ee}^* P}, 1)$	$(1.1759 \pm 0.0001) \%$	$(1.568 \pm 0.003) \%$	$(1.70 \pm 0.01) \%$
$B(2, p_{\gamma_{ee}^* P}, 2)$	$(3.4983 \pm 0.0005) \cdot 10^{-5}$	$(6.25 \pm 0.03) \cdot 10^{-5}$	$(7.37 \pm 0.06) \cdot 10^{-5}$
$BR_{KW}(\rightarrow 2\gamma)$	$(98.8206 \pm 0.0001) \%$	$(39.41 \pm 0.20) \%^*$	$(2.20 \pm 0.08) \%^*$
$BR_{KW}(\rightarrow \gamma e^+ e^-)$	$(1.1759 \pm 0.0001) \%$	$(6.28 \pm 0.03) \cdot 10^{-3}*$	$(3.81 \pm 0.14) \cdot 10^{-4}*$
$BR_{KW}(\rightarrow 2(e^+ e^-))$	$(3.4983 \pm 0.0005) \cdot 10^{-5}$	$(2.50 \pm 0.02) \cdot 10^{-5}*$	$(1.65 \pm 0.06) \cdot 10^{-6}*$

Table 7.1: Dalitz decay branching ratios of π^0 , η and η' . *Values are scaled to the measured PDG value of the two-photon decay branching ratio of the respective particle.

pairs from the two possible photons is thus given by the binomial distribution with $B(n = 2, p = p_{\gamma_{ee}^*|P}, k)$. Scaled with the measured (a.k.a. PDG) branching ratio of the two-photon decay thus yields the Kroll-Wada estimate of the branching ratio of the Dalitz decay.

$$p_{\gamma_{ee}^*|P} = \int dm_{\gamma_{ee}^*} \left(\frac{1}{N_\gamma} \frac{dN_{\gamma_{ee}^*}}{dm_{\gamma_{ee}^*}} \right)_P$$

$$BR_{KW}(P \rightarrow (2 - k) \cdot \gamma, k \cdot (e^+ e^-)) = B(2, p_{\gamma_{ee}^*|P}, k) \cdot \frac{BR_{PDG}(P \rightarrow \gamma\gamma)}{B(2, p_{\gamma_{ee}^*|P}, 0)}$$

Since the total width of the pion is entirely given by photonic decays, this scaling is not necessary. Thus for the pion it holds that $BR_{KW}(\pi \rightarrow (2 - k)\gamma, k(e^+ e^-)) = B(2, p_{\gamma_{ee}^*|\pi}, k)$ and this procedure calculates directly all the relevant branching ratios: $\pi^0 \rightarrow 2\gamma$, $\pi^0 \rightarrow \gamma e^+ e^-$ and $\pi^0 \rightarrow 2(e^+ e^-)$. Table 7.1 shows the results for π^0 , η and η' mesons. The calculated Kroll-Wada branching ratios are consistent with the current PDG measurements. For the pion all three branching ratios are entirely inside the one standard deviation of the measurements. This is also true for the double Dalitz decay of the eta, while the single Dalitz decay branching ratios are about 1.5 standard deviations apart. The calculated branching ratio of the single Dalitz decay of the eta prime was used in the cocktail simulation, since the measurements provided only an upper limit. We can conclude that the calculations of the virtual photons are well inside the uncertainties of the most precise measurements currently available. Although outside the scope of this work it should be mentioned that in principle it would be possible to extend the discussion to Dalitz muons by exchanging the binomial distribution with the multinomial distribution.

7.2 Mother Particle p_T Spectra

Many of the mother particles needed for this analysis as input for the simulation, are not easily measured in the needed precision. Being the lightest meson, an abundance of pions is produced in each event. Pions were first anticipated by H. Yukawa in the

1930's as being the particles mediating the strong force between nucleons, giving rise to an attractive potential binding the nucleons into the atomic nuclei. Pions are a spinless bound two-particle state consisting of the two first generation quarks with opposing spin. There are three pions: the charged $|\pi^+\rangle = |u\bar{d}\rangle$, its antiparticle $|\pi^-\rangle = |u\bar{d}\rangle$ and the neutral mixed state $|\pi^0\rangle = (|u\bar{u}\rangle + |d\bar{d}\rangle)/\sqrt{2}$. Being the lightest meson, pions cannot decay under the strong force. While the electromagnetic decay is possible for the neutral pion, which decays into two photons, the charged pion can only decay weakly by coupling to the W^\pm -boson. Due to a remarkable interplay of the properties of the weak force with the pion's zero total spin, it can only decay into the energetically unfavourable configuration of a neutrino and a muon¹⁸. Because of the small volume of phase space remaining and due to the fact that the weak coupling is considerably weaker than the electromagnetic coupling, the life time of the charged pion is 10 orders of magnitude longer than that of the neutral pion. Making it one of the few hadrons that can be measured directly and not by reconstructing its decay products. Thus measurements of charged pions are easily surpassing measurements of other identified particles in both, accuracy and precision.

As shown in Chapter 3.5, all particles decayed by a hydrodynamic QGP should in principle follow the same m_T -distribution, in case of a vanishing flow. However it was also shown that even with a finite flow the approximation may still be usable, especially in the momentum range the inclusive measurement is conducted. This is why this analysis uses the measured charged-pion spectrum as a baseline for the m_T -scaling to describe the momentum distribution of all the other mesons concerned.

7.2.1 Pion p_T Spectrum

There are ALICE measurements for both charged and neutral pions [78, 160, 161]. While the neutral pion measurement would be the natural choice, since only these are part of the electron background, the measurement of the charged pion is of much higher accuracy. And since there are no reasons for the two spectra to be fundamentally different, the measurement of the charged-pion momentum spectrum is used instead.

To produce the background electrons, the Monte Carlo simulation needs this spectrum as input. Thus the spectrum must be fitted with an appropriate functional form. Figure 7.2 shows the neutral and charged pion measurements as well as the fit to the charged-pion spectrum using a modified Hagedorn function [76]. This is the baseline for the m_T -scaling.

Since all the momentum spectra are steeply falling, it would be problematic to directly use these as probability densities for the respective particles. This would produce a very strongly momentum-dependent statistics, with a lot of entries at very low momenta and almost nothing at high momenta. Thus instead the simulation produces the particles following a uniform distribution using the momentum spectra as a weight for each produced particle in consequence of its momentum it

¹⁸Compared to the decay $\pi^\pm \rightarrow e^\pm \nu_e$ which is forbidden due to helicity, the decay $\pi^\pm \rightarrow \mu^\pm \nu_\mu$ is energetically unfavourable because the μ mass (105 MeV) is a large fraction of the π^\pm mass (140 MeV)

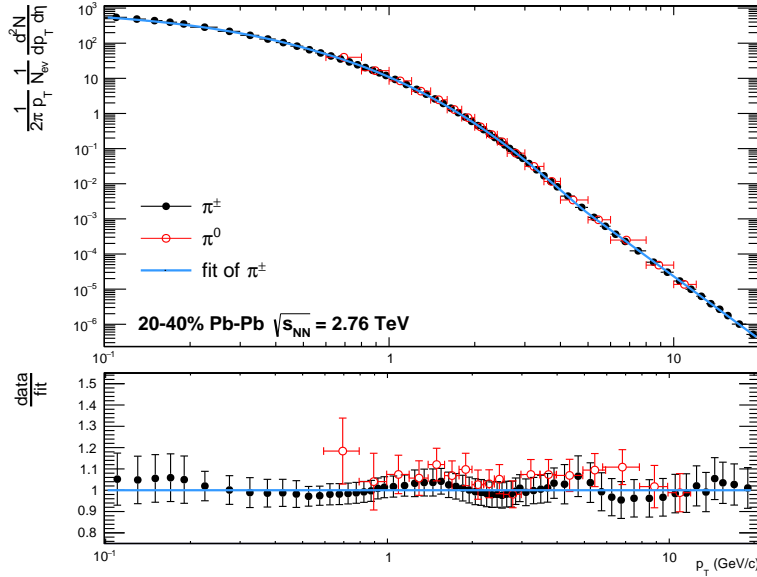


Figure 7.2: p_T spectrum of charged and neutral pions as well as the fit

was generated at. The weight must however be taken into account in the whole simulation and analysis chain.

Systematic Uncertainty

The systematic uncertainty of the pion momentum spectrum is given by the fit error and the deviation of the neutral pions to the fitted charged pions. Both errors can be evaluated from the scattering and the systematic errorbars of the points in Figure 7.2. This is done by fitting the ratio of the measured spectrum to the spectrum fit (lower panel of Figure 7.2) with a one-parameter linear fit, representing only the scale. While a deviation of the parameter fit value from 1 represents a systematic shift, the error of this parameter can be viewed as the standard error of the mean (σ_m) of the deviations of the n data points about the fit:

$$\sigma_m = \frac{\sigma}{\sqrt{n}}$$

Solving for σ , which usually represents the standard deviation of each of the n samples, and thus using this equation backwards, one gets a constant systematic error, effectively equalizing the systematic errors and the scattering of the n points over the whole range.

The uncertainty on the fit due to the scattering and the systematic error of the charged pions about their fit is 5%, while the neutral pions have a 9% scattering. Additionally there is also a systematic shift of 5%. This error is correlated between all other particles whose spectra are based on m_T -scaling.

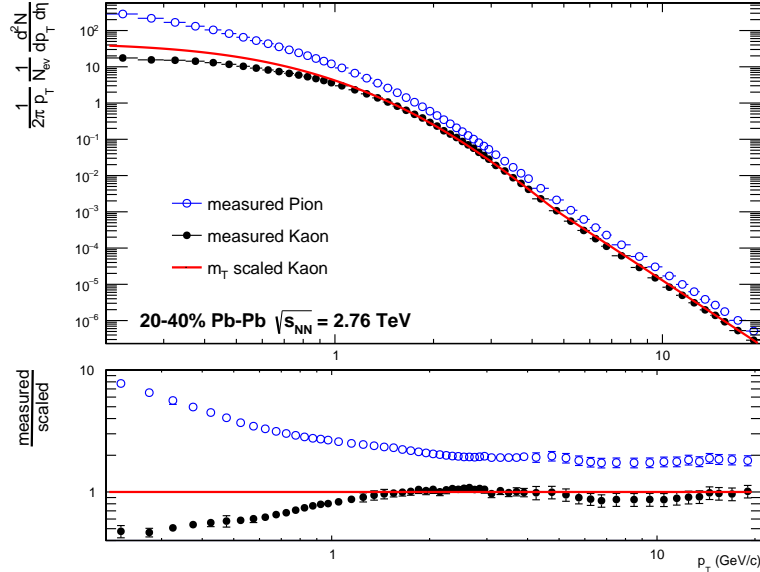


Figure 7.3: The quality of m_T -scaling as compared to measured kaons. This plot can be compared to Figure 3.4 of the hydro calculations in Chapter 3.5.

	Factor	Error	References
η/π	0.476	0.03	[162, 163]
ρ/π	1.0	0.3	[162, 166]
ω/π	0.85	0.06	[162, 165]
η'/π	0.4	0.12	[162, 166]
ϕ/π	0.25	0.08	[162, 164]

Table 7.2: Scaling factors used the m_T -scaling

7.2.2 m_T -Scaling Factors

While the m_T -scaling describes the m_T dependence of the spectrum it does not predict the total scale. As mentioned in Chapter 3.6 it is possible to extend the model to include a global fit for all particle types, however, this is not what is usually done. It is easier to simply scale the m_T -scaled spectrum to a previous measurement: [162–165]. The scaling factors used are shown in Table 7.2. With the scaling factors set, it is worth taking a look at the functional form. Figure 7.3 shows a comparison of measured kaons to the m_T -scaled pions. This comparison shows quantities similar to the calculations in Chapter 3.5. Comparing this plot with Figure 3.4 confirms the expectations on the quality of the m_T -scaling. We see that above about a momentum of 1.5 GeV/c the m_T -scaling works relatively well. Since the mass of the kaon is very similar to that of the eta, this result should be applicable there too. The effect of a different scaling is analysed in Chapter 7.6.

Systematic Uncertainty

The systematic error component entering the momentum spectrum of each particle where m_T -scaling is applied follows directly from the uncertainties on the m_T -scaling

factors shown in Table 7.2.

7.2.3 Direct Photon p_T Spectra

The situation for the direct photons is more complicated than for the mesons. In a heavy-ion collision, there is a huge number of photons produced by many different processes:

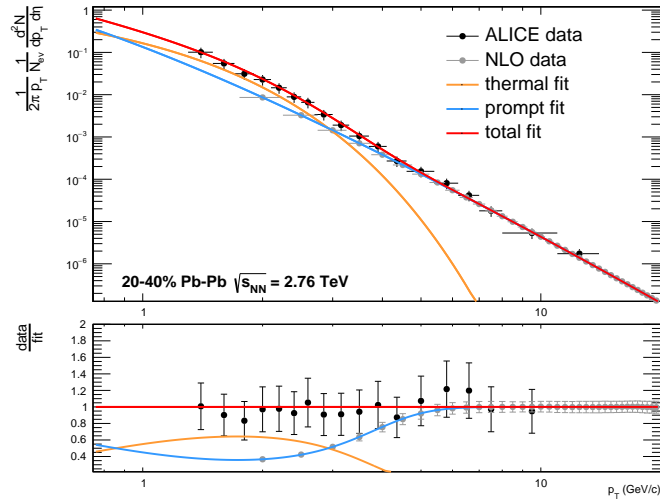
- hard photons from parton Compton scattering and parton annihilation
- hard photons from parton bremsstrahlung and parton fragmentation
- photons from pre-equilibrium
- medium-induced photons
- thermal photons from the QGP and hadron gas
- decay photons

Apart from the decay photons, all other photons listed are called direct photons. The direct photons minus the thermal photons are called prompt photons. The following ALICE measurements are used: [167, 168]. Compared to the momentum reach of the pion measurement, the direct photon measurements are relatively restricted. This might be problematic for the simulation since a converting photon is source of two electrons. It must be secured that the simulated electrons have a reach well above the reach of the inclusive electron measurement. To extend the momentum region of the measurements towards high momenta, the Next-To-Leading Order (NLO) calculations of prompt photons from W. Vogelsang [169] are used additionally. The NLO calculations must be scaled for the given centrality. Since photons do not interact strongly, this can be easily done by scaling with the number of binary collision.

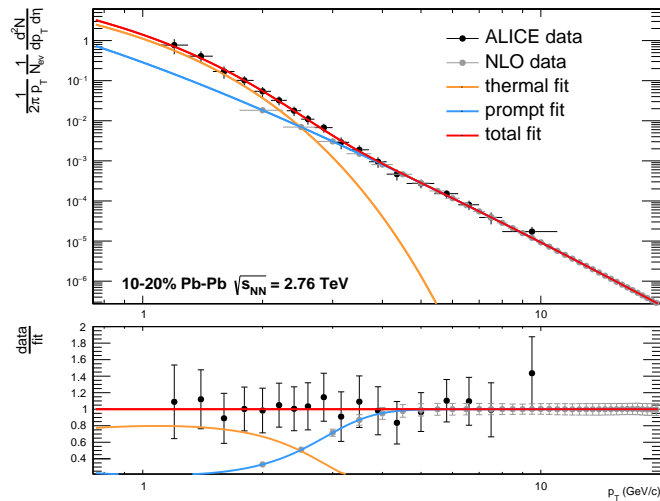
The fit to the data was produced in a two-step procedure. First the data of the NLO calculation was fit with a modified Hagedorn function. Then the ALICE direct-photon measurements were fit adding an exponential part for the thermal component of the spectrum and a free scale parameter for the now fixed Hagedorn part. Figure 7.4 shows a fit of the scaled NLO calculations together with the ALICE measurement. It can be clearly seen that the ALICE measurement increases towards low momentum much faster than the NLO calculations. This is due to the thermal photons, which are not included in the calculations. Since the amount of thermal photons is directly linked to the medium temperature, and the medium temperature is increasing with centrality, the relative and absolute amount of thermal photons increases also with centrality.

Systematic Uncertainty

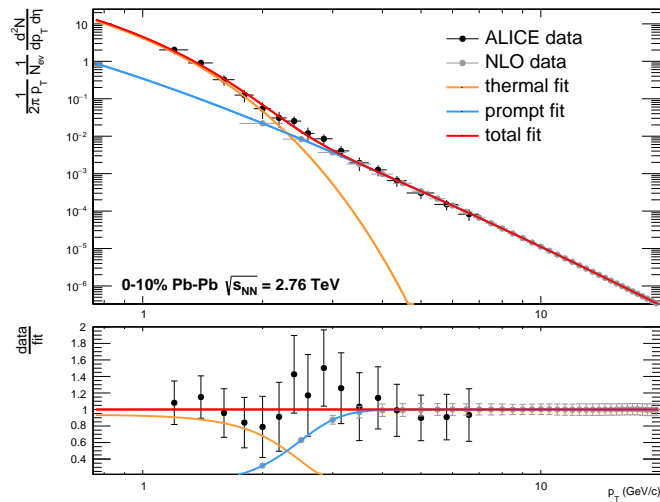
The systematic uncertainty (25%) is extracted just like for the pion by fitting the ratio of the fit to the data. The uncertainty extracted from the NLO calculations (5.6%) is completely outweighed by the errors on the measurements.



(a)



(b)



(c)

Figure 7.4: Direct-photon p_T spectrum in three centrality bins. The thermal photon yield increases going towards more central collisions.

7.2.4 Virtual Direct Photons

Each photon source does not only produce real photons, but also, to a lesser degree, lepton pairs. The coupling of the source to the lepton pair via a virtual photon can be seen as a decay of an emitted massive virtual photon with an immediate decay into the lepton pair. These electron-positron pairs are of course background to the measurement of this work and must be subtracted. However, as the mother photon is just a virtual photon, it cannot be part of any photon measurement. Thus the virtual photon contribution must be estimated based on the amount of real photons.

In this work, the production of virtual photons is estimated by linking it to the production of real photons using Equation 7.2 as explained in Chapter 7.1. For each real photon produced based on the measured real photon spectra, a fraction of virtual photons of a specific mass is produced. In the simulation this is realized by using a weight for the virtual photons, that is given by the integral of Equation 7.2. And the mass is given at random using Equation 7.2 as the probability distribution. Following the discussion in Chapter 7.1 a global energy constraint must be provided. This constraint represents the maximal mass the virtual photon can have such that the electron-positron pair produced by it does not violate global energy conservation.

In principle this means that the momentum spectrum of real photons is scaled with the integral of Equation 7.2 to get the virtual photon spectrum. However, a simple spectrum scaling does not work in this analysis because we are not only interested in the p_T spectrum of the mother particles, but also in the p_T spectrum and especially the v_2 of the daughter electrons. Thus the actual kinematics of the electron-positron pair must be simulated. This was done by treating the virtual photon as a real massive particle that decays into an electron-positron pair. This procedure is roughly comparable to what has been previously conducted at measurements at RHIC [124].

Figure 7.1 shows the number of virtual photons per real photon. The fraction of virtual photons is ever increasing with the global energy constraint.

Systematic Uncertainty

Apart from the value of α the procedure used is based entirely on theoretical calculations, without any relation to measurements. Thus no systematic uncertainties can be attributed to the virtual photon component of the cocktail. The validity of the calculations have however been tested in Chapter 7.1.2.

7.3 Mother Particle v_2 Spectra

Similarly to the m_T -scaling of the meson p_T spectra, for the elliptic flow KE_T -scaling is used to estimate the meson v_2 spectra. As for the p_T spectra, the baseline is the charged pion. Since elliptic flow is the intended measurement, it is also the most important ingredient for the background electron cocktail.

7.3.1 Pion v_2 Spectrum

There are three relevant analyses of the elliptic flow of identified particles in ALICE: two low- p_T and one high- p_T measurement [89, 135, 170, 171]. The two low- p_T analyses differ only in the elliptic flow measurement method used, one using the event-plane method (Chapter 5.2.2), and the other using the scalar product method (Chapter 5.2.4). The high- p_T analysis also uses the event plane method. This was the key argument to use the event-plane method as primary method in this work as well. Figure 7.5 (a) compares the two low- p_T measurements. Since these two measurements are almost identical, the two data sets are completely interchangeable.

As for the momentum spectra, the v_2 spectra must be fit in order to be usable by the Monte Carlo simulation. The low and high p_T measurements were merged using the high- p_T points as an extension to the low- p_T points. The functional form used to fit the spectrum, is based on two sigmoidal functions: one for the raising region and the other in the falling region of the spectrum. These two regions are merged using a trigonometric crossover function. The fit is produced by first fitting the two regions individually and then fitting them together with the crossover function.

The light hadron measurements are segmented in smaller centrality bins than the centrality bin analysed in this work (20-40%). The two centrality bins 20-30% and 30-40% are thus merged by scaling each with its momentum spectrum, which is encoded into the statistical errors of the data points.

Systematic Uncertainty

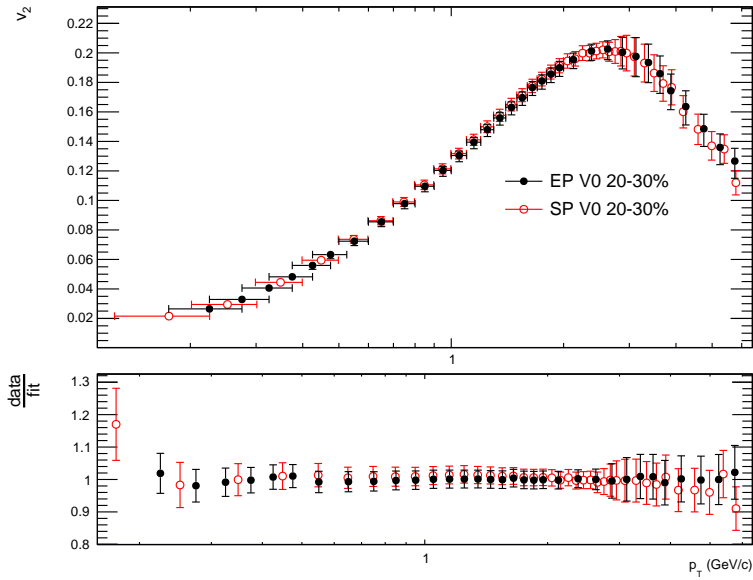
The systematics of the fit are shown in Figure 7.5 (b). They are the result of an individual power-law fit of the lower and upper error of the data. While the error on the data is the squared sum of the statistical and systematic error bars.

The spectrum fit is the spectrum of charged pions, however the simulation must actually produce neutral pions. In contrast to the charged pion, the flow measurement of the neutral pion is rather involved, directly affecting the spread of the measurements and their uncertainties. This is the reason the charged pion data is used for the parametrisation instead. However, available neutral pion measurements for the LHC show a discrepancy to the charged pion in the range +10%/ - 20%, depending on the measurement [172, 173]. This range was taken as an additional systematic uncertainty for the pion v_2 spectrum.

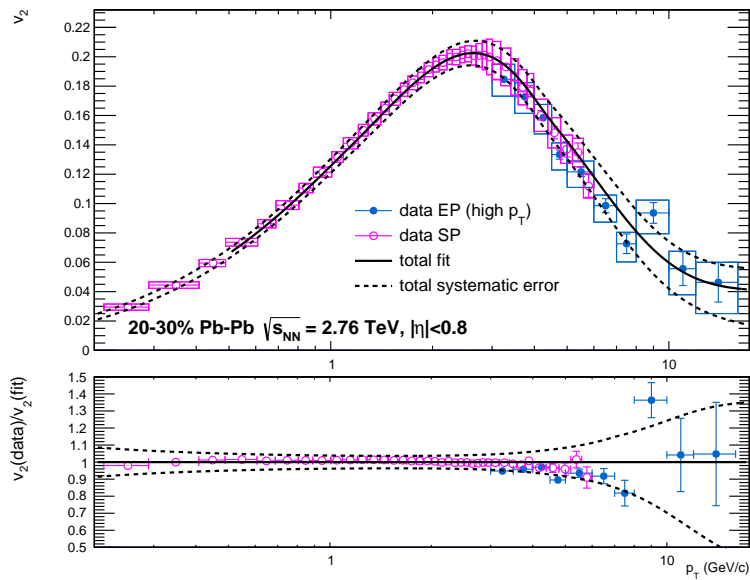
Similarly as for the pion p_T systematic error, the pion v_2 error component is correlated among all particles where KE_T -scaling is used.

7.3.2 KE_T -Scaling

As discussed in Chapter 3.9 it was found that similarly to the situation of the momentum spectra, the elliptic flow of light hadrons are also interrelated. Being an empirical finding, KE_T -scaling is not a perfect property. Figure 7.6 show the comparison between the measured kaon and the pion-based KE_T -scaling approximation. Because of the similar mass of the kaon to the eta, it is assumed that the kaon can be an approximation to the eta.



(a)



(b)

Figure 7.5: Comparison of the elliptic flow of the measured π^\pm using the event plane and the scalar product method (a) and the fit to the data (b).

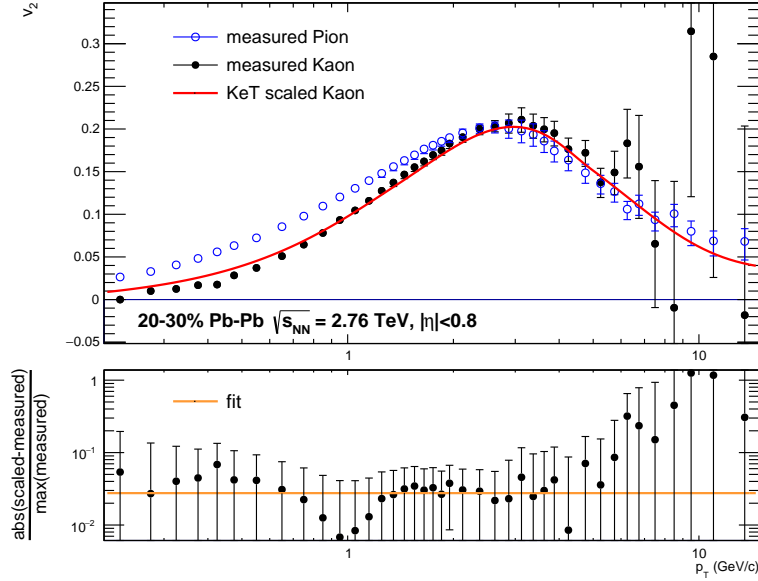


Figure 7.6: The quality of KE_T -scaling as compared to measured kaons.

Systematic Uncertainty

The systematic uncertainty for the KE_T -scaling is extracted from the lower panel of Figure 7.6. It shows the absolute difference of the scaling to the data relative to the maximum of the data and a constant fit to it. This is used as systematic uncertainty for all mesons. Of course the systematics extracted from the kaons is actually not applicable to anything else other than the eta, however, the eta is by far the most important meson after the pion.

As shown in Figure 7.12 (b) the higher mass mesons represent only a very small fraction of the total cocktail, with a maximal aggregated weight of 5% at a transverse momentum of 3 GeV/c. From Figure 3.7 it can be seen that there the ϕ is off by less than 20%. Since it is the heaviest meson included in the cocktail, it can be assumed to represent the worst-case scenario. This means that the additional uncertainty contribution to the total systematic error is less than 1%.

7.3.3 Direct-Photon v_2 Spectrum

The elliptic flow of direct photons has been measured by PHENIX at RHIC and ALICE at the LHC [172, 174]. Figure 7.7 shows the 20-40% ALICE data and the fit to it. Like for most ratio plots in this work, the straight line in the lower panel is not just fixed, but is actually a fit to the ratio points reassuring that the initial fit has worked as expected. Unfortunately this analysis did not produce results for other relevant centralities, with the 0-10% and 10-20% percentiles missing. When these percentiles are of interest, it is possible to use the ratio of the respective pion spectra as a scaling factor. Of course this introduces an additional systematic uncertainty, on top of what is shown in Figure 7.7. This additional uncertainty has been extracted by cross-validating the 3 available centralities of this analysis (0-20%, 20-40% and 0-40%). The uncertainty thus extracted is in the range of about 15 to

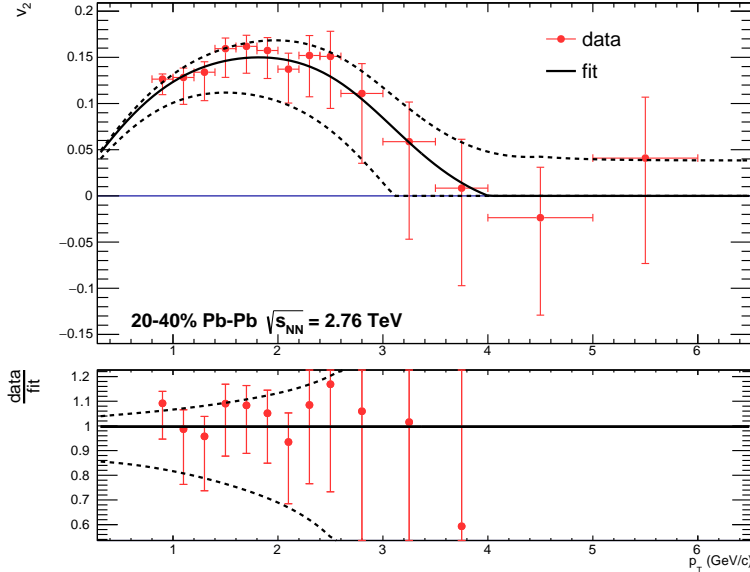


Figure 7.7: The fit to the direct-photon measurement

25% on the spectrum. To be on the safe side, the 25% figure has been taken for all scaled centralities.

What is also visible in Figure 7.7 is that the fit function does not cross into the negative. Letting the function go lower would actually strongly increase the final result's numerical value in the respective momentum region. Up to today no measurement of any particle type has ever yielded any significant measurement of negative elliptic flow in the relevant momentum region. Also from the theoretical point of view, at least from the discussion in Chapter 3.4 it appears implausible to expect any negative elliptic flow. Thus the negative region has been declared unphysical for the scope of this work.

7.4 Electron Generation

The previous chapter described the properties of the simulated electron sources. From each of these sources, there are different ways electrons to be generated. Mesons, like the pion or the eta, can produce electrons either by directly decaying into them in semi-leptonic decays, or through photon decays, with the photons subsequently converting into electron-positron pairs inside the detector material.

The most important decay channels are those decay channels producing the most electrons. This depends on the initial amount of mother particles, on the decay probability into electrons, or on the decay probability into photons multiplied by the conversion probability of the photons into electron pairs. The two most important decay channels are the pion Dalitz decay ($\pi^0 \rightarrow \gamma e^+ e^-$) and the pion two-photon decay $\pi^0 \rightarrow 2\gamma$ with the subsequent conversion into electron pairs ($\gamma \rightarrow e^+ e^-$).

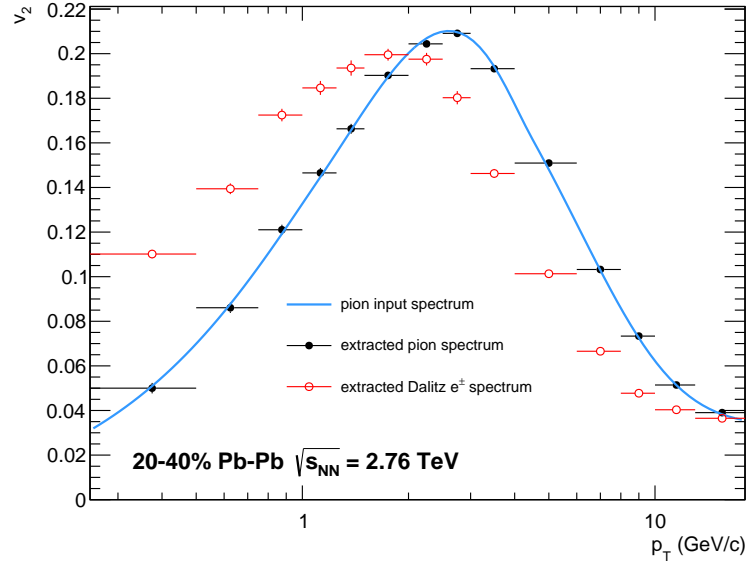


Figure 7.8: Elliptic flow of the mother π and daughter Dalitz e^\pm as extracted from the simulation compared with the input parametrisation for the π .

7.4.1 Decay Electrons

After the generation of the electron sources, the simulation includes a particle decay step, where PYTHIA 6 [166] is used as a decayer. This decayer produces the daughter particles based on relativistic kinematic calculations. A critical ingredient is the decay channel probability, called branching ratio. The branching ratios used were the newest ones available by the PDG publications [15]. For the heavier mesons, there are usually many different decay channels possible, with only a minority actually producing any electrons. To avoid this inefficiency, only the decay channels producing electrons were taken into account, updating the particle weight according to the decay channels probability.

For the eta prime the newest measurement available by the PDG publications provide only an upper limit for one of the most important decay channels, the Dalitz decay. In order to have a reasonable value for this channel, its expected probability was calculated (see Chapter 7.1.2 for details). Figure 7.8 shows a comparison of the elliptic flow of the decay electrons and the mother pion extracted from the simulation. The electrons are shifted towards smaller p_T because they are always produced in pairs. The maximum of the spectrum is slightly below the maximum of the mother pions, because the electrons are decayed with an opening angle, reducing the spatial correlation and thus the eccentricity of the spacial distribution somewhat.

7.4.2 Conversion Electrons

When photons pass through matter, a number of different phenomena are observed. From low to high energy of the photon this can be the photoelectric effect, Thomson or Compton scattering or pair production. In our case we are dealing with high energetic photons of at least a few hundreds of MeV. In this domain, only the

electron pair production is relevant.

Pair production is usually simulated by providing the geometry of the whole detector, and passing the photons step by step through the model. Depending on the currently neighbouring material of the photon in each step, it is randomly decided how to proceed to the next step. In the ALICE software framework this is usually done by the `geant3` library [175]. This high-quality procedure is however extremely slow in computing time, and it would not be possible to produce the statistics needed for this work in reasonable time, and having it saved within reasonable storage space¹⁹.

Instead the relevant procedures of the `geant4` library [176] were adapted to immediately produce a pair production for each photon independently on its surrounding. This slows down the simulation by only 10% and is thus a factor four faster, uses a quarter of the storage space and produces an order of magnitude more statistics compared to the usual procedure. However, the pair production simulated corresponds to an infinite radiation length. To obtain the desired result, the momentum distribution must be scaled to the needed radiation length. This scaling factor is simply given by the mean probability of the pair production itself, as described in Chapter 10.2:

$$\frac{1 - \exp\left(-\frac{7}{9} \cdot \frac{X}{X_0} \cdot \frac{\bar{x}}{x_0}\right)}{1 - \exp\left(-\frac{7}{9} \cdot \frac{\infty}{X_0} \cdot \frac{\bar{x}}{x_0}\right)} = \frac{1 - \exp\left(-\frac{7}{9} \cdot \frac{X}{X_0} \cdot \frac{\bar{x}}{x_0}\right)}{1} = \bar{p}_{pair}$$

The results from both procedures (“full” and “fast”) are compared for the pion, where also a third calculation is possible. This third possibility consists of directly scaling the Dalitz electron spectrum with the above probability and the ratio of the branching ratios of the 2-photon decay to the Dalitz decay:

$$\frac{\text{conversion}}{\text{Dalitz}} = \frac{(2 \cdot BR_{\gamma\gamma} + BR_{\text{Dal}}) \cdot \bar{p}_{pair}}{BR_{\text{Dal}}}$$

This can be only approximative though, since here it is not possible to correct for the photon momentum-dependent conversion probability. Hence, for low momenta this component overestimates the amount of conversion electrons, as can be seen in Figure 7.10 (a). Of course, simply scaling a momentum spectrum does not represent a sound kinematic calculation, and thus there is no possibility to get any elliptic flow spectrum from this method. However, analysing the decay channels of pions into electrons (Figure 7.9) we can see that the Dalitz decay ($\pi \rightarrow \gamma e^+ e^-$) and the 2-photon decay ($\pi \rightarrow 2\gamma$) with a subsequent gamma conversion ($\gamma \rightarrow e^+ e^-$) are in fact very similar.

We can thus expect the elliptic flow of conversion electrons to be the same as for Dalitz decay electrons. Figure 7.10 (b) compares the elliptic flow of the conversion electrons calculated by the two methods (“full” and “fast”) and the Dalitz decay electrons. It can be clearly seen that our expectation is fulfilled. This result means that in fact for the pion we could actually really just scale the momentum spectrum

¹⁹A single simulation of the needed six per centrality already takes a day of CPU time and uses 50GB of storage space

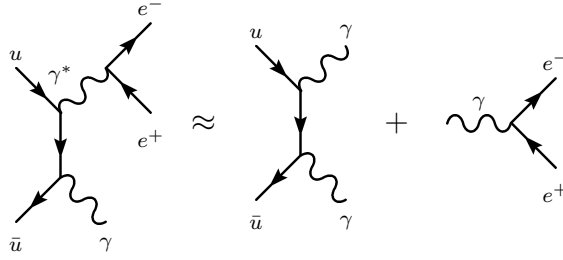


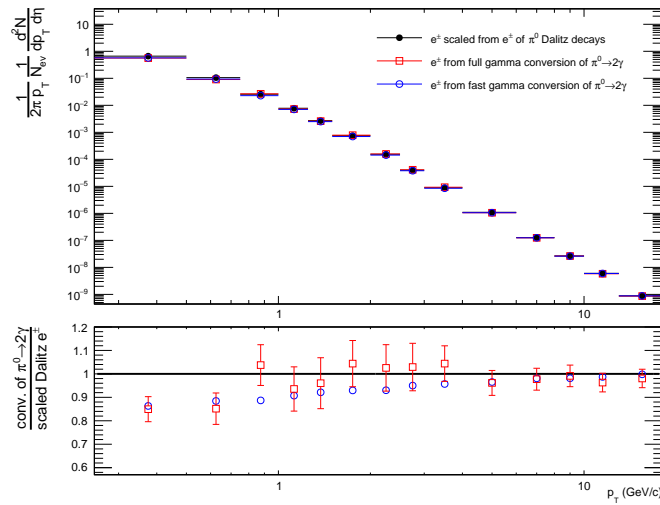
Figure 7.9: Similarity of the pion Dalitz decay and the 2-photon decay with subsequent gamma conversion. Due to this the Dalitz decay is sometimes also called internal conversion.

and use as v_2 spectrum the result from the Dalitz decay electrons. However, this cannot be done for the heavier mesons which have completely unrelated decay channels. Figure 7.10 (c) compares the v_2 of electrons from the direct electron decay of the rho meson, with the electrons for the gamma conversions of rho decay gammas. It can be seen that the elliptic flow of the direct electrons is completely different from the conversion electrons. In all three plots the “fast” conversion mechanism is inside the statistical errors of the “full” calculation but provides much more statistics.

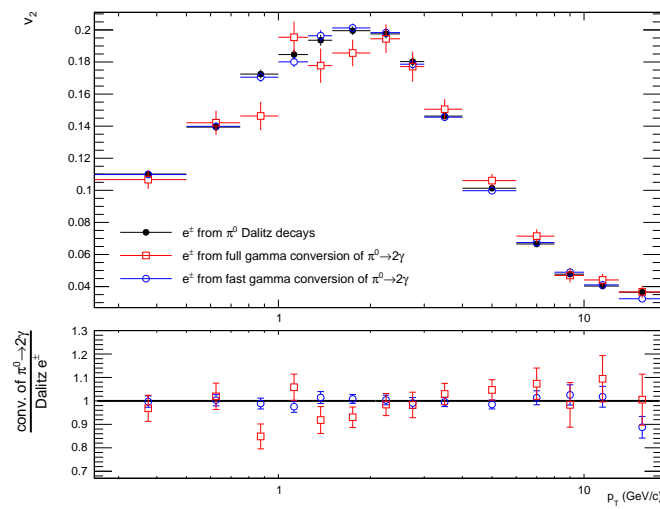
7.4.3 Electrons from Virtual Direct Photons

As shown in the previous paragraph, the kinematics of the pion Dalitz decay (internal conversion) and the conversion decay photons (external conversion) are sufficiently similar, such that all the electrons produced by pions have effectively the same elliptic flow spectrum Figure 7.10 (b). It is thus appealing to extend this argumentation to all virtual photons by assuming that all electrons originating from the same source share the same elliptic flow spectrum, be they produced by conversions of real photons or decay of virtual photons. In fact the only thing special to the virtual photons of the pion is the pion form factor and the relatively low global energy constraint given by the pion mass. While the form factor represents only higher order correction to the virtual photons, the pion mass is indeed low.

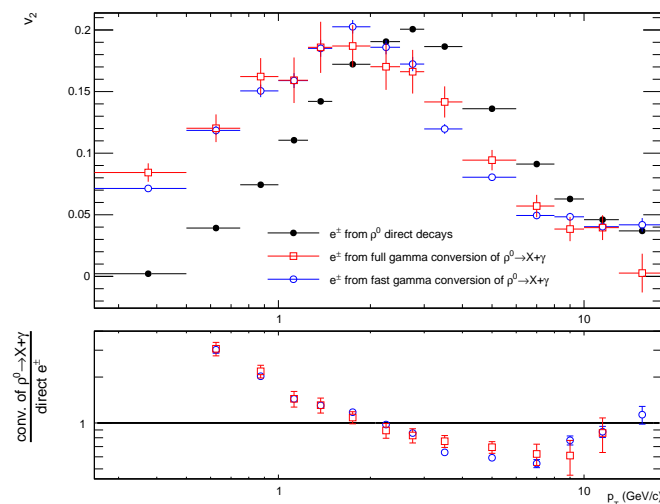
To secure the argumentation, it is worth testing it with a heavier particle. Figure 7.11 (a) compares the elliptic flow of electrons from eta Dalitz decays with the elliptic flow of conversion electrons originating from eta and pion. While both eta electron spectra move in lock step, the pion electrons are considerably different. Thus at a particle four times the mass of the pion, the electrons show a significantly different spectrum, but the result concerning the difference between electrons from Dalitz decays and conversions is the same as for the pion. This test should increase the confidence that indeed electrons from virtual photons generated by any source should have an elliptic flow similar to that from conversion electrons of photons from the same source. And indeed, the implemented decay kinematics of virtual photons provides exactly this finding: Figure 7.11 (b). The virtual photon calculations can thus be regarded as consistent.



(a)

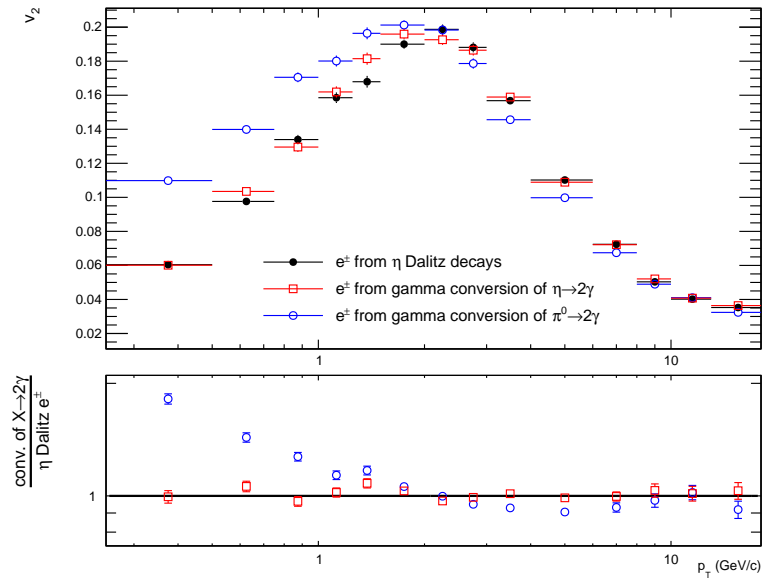


(b)

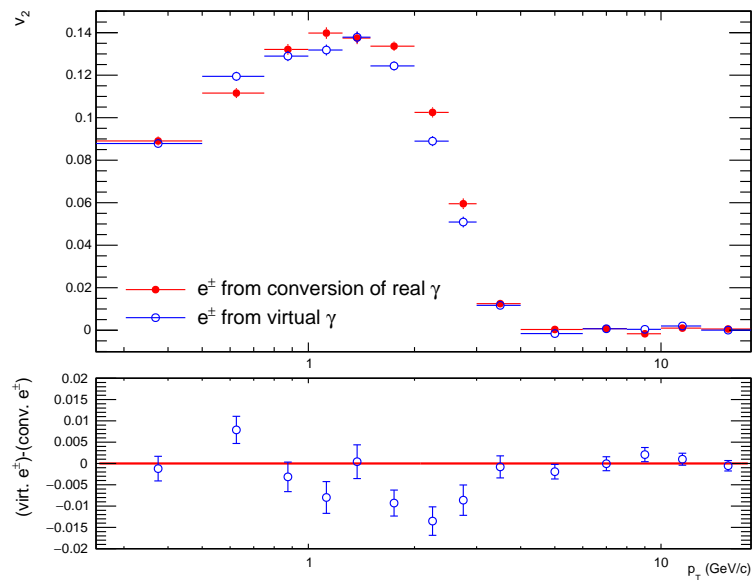


(c)

Figure 7.10: The “full” and “fast” conversion mechanisms are inside each others statistical errors.



(a)



(b)

Figure 7.11: Elliptic flow of the Dalitz e^\pm compared to conversion e^\pm from η mesons (a) and the elliptic flow of electrons from virtual and conversions of real direct photons (b). Electrons from the same sources have the same elliptic flow, independently whether they were produced in a conversion of a real photon or via a virtual photon.

7.5 Cocktail Mixing

The systematic uncertainties of the mother particle elliptic flow spectra are strongly momentum dependent (see also Figure 7.5). It is thus necessary to produce three separate simulations: one where the v_2 is taken from point value of the mother particle v_2 spectra, and one each for the lower and upper end of the systematic error bars respectively. Otherwise, the three simulations are identical, especially concerning the momentum spectra of the particles, which can thus be added together increasing the statistics. All other systematics are taken as flat in momentum, and can thus be applied directly on the electron level, avoiding an unreasonable amount of individual simulations. Then, the momentum and the elliptic flow spectra of all electrons are extracted in groups differentiated by their source particle.

Due to the fact that the branching ratios of the leptonic decays of the mesons are around two orders of magnitude smaller than for the photon decays, it is necessary to separate these two cases: One simulation restricted to the leptonic decays and another one for the photon decays. This increases the amount of necessary simulations by a factor of two, resulting in a total number of six simulations for each mother particle species.

The electrons generated from the simulated mother particles must be merged into one sample to produce the background electron spectrum. Electrons from each source particle have different spectra, as shown in Figure 7.12 (a). The combined momentum spectrum is then simply the sum of the separate momentum spectra of the daughter electrons. In order to get the proper elliptic flow spectrum of the combined sample, the elliptic flow spectra of electrons from each species must be weighted with its respective relative momentum spectrum. Figure 7.12 (b) shows the normalized momentum spectra which are used as a weight for the elliptic flow spectra. The weighted spectra can then be added together producing the intended result of the background electron elliptic flow spectrum, shown in Figure 7.12 (c).

Systematic Uncertainty

To be able to produce the total systematic uncertainties, the cocktail is mixed multiple times: each time with errors corresponding to a different error component. The uncertainties of the electron spectra which originate in the uncertainties of the mother particle spectra must be propagated to the combined sample taking account of the correlations. Particle spectra based on m_T or KE_T -scaling share the systematics of the pion spectra, while the systematics of the m_T and KE_T -scaling themselves are only shared between electrons of the same mother. The errors of these created systematic error cocktails are then finally added under the assumption of being completely uncorrelated among themselves. Figure 7.12 (d) shows the contribution of the error components to the total systematic error.

7.6 Systematic Studies

The following systematic studies were performed to test the stability of the electron background cocktail under modified assumptions.

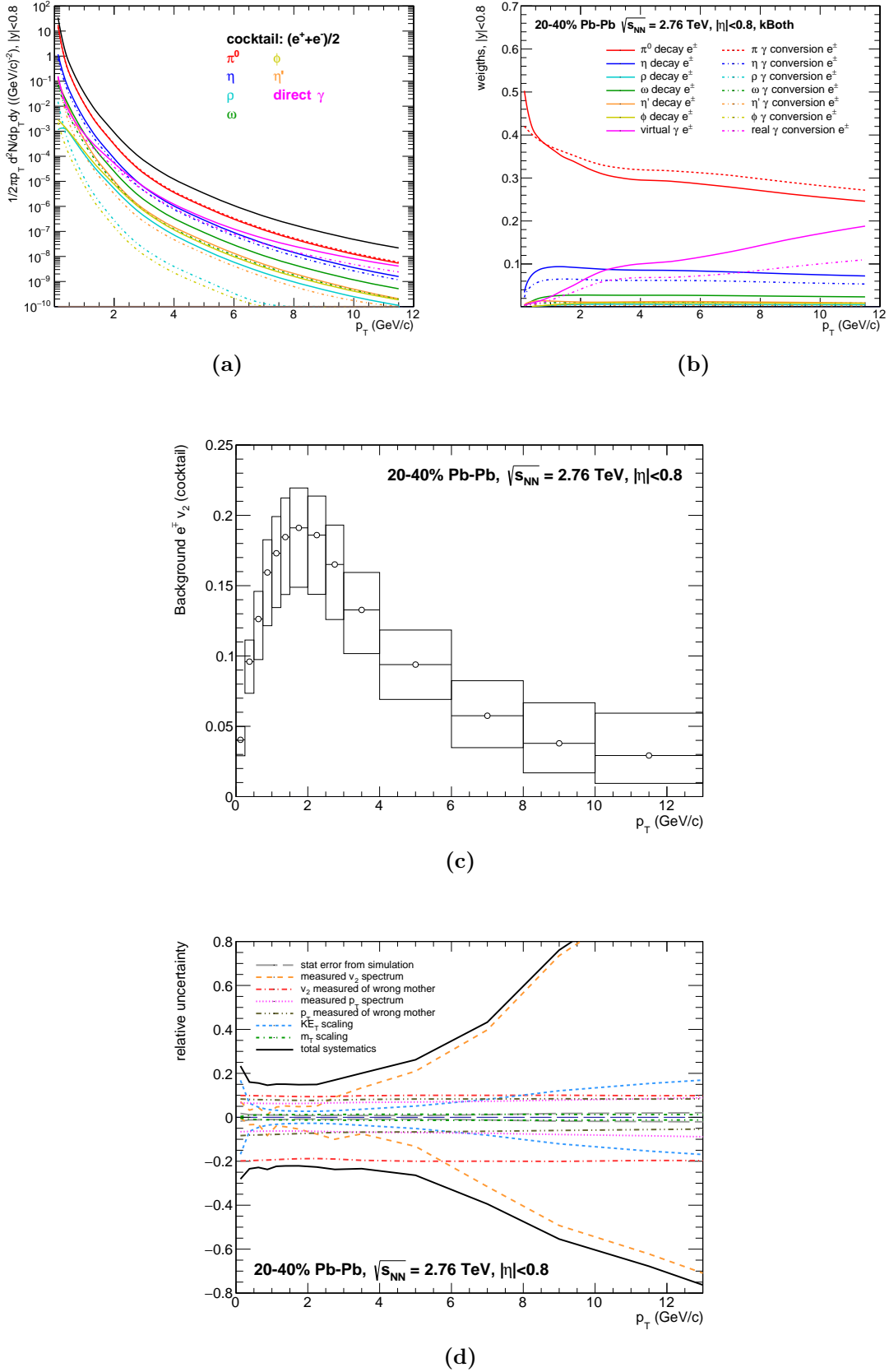


Figure 7.12: Absolute (a) and relative (b) p_T spectra of simulated electrons. The background electron elliptic flow (c) and the constituents of its systematic error (d). The figures of the other centralities analysed are attached in the appendix (Figure 10.3 and Figure 10.4).

7.6.1 Momentum Spectra Scaling

Due to mostly missing measurements, the spectra of all mesons apart from the pion must be estimated. The method of estimating these momentum spectra is based on m_T -scaling of the measured charged pion spectrum (see also Chapter 3.5). Thanks to a measurement of the η/π^0 -ratio in 7 TeV proton-proton collisions [163], it is possible to assert the influence of a different scaling to the cocktail.

Figure 7.13 (a) shows a comparison of the measured data and the m_T -scaling. In the high momentum part, the fit is influenced heavily by the high-uncertainty points, producing an overshoot which appears quite unphysical. From Chapter 3.5, Figure 3.4 and Figure 7.3 there is the data-backed expectation that m_T -scaling should be rather good at high momenta. Nevertheless, a test using this fit to the η/π^0 -ratio was used, by scaling it with the 2.76 TeV Pb-Pb π^\pm measurement (Figure 7.2).

The resulting cocktail (Figure 7.13 b) shows no significant departures from the m_T -scaling based cocktail.

7.6.2 Reconstruction Resolution

The background electron cocktail is based on completely corrected measurements of the electron sources. This means that all the detector effects have been deconvoluted from the respective spectra. The measurement of the inclusive electrons (Chapter 6) however does still include the detector effects. Since the background is subtracted from the inclusive measurement to get the final result, there are now two possibilities to get a really consistent treatment: Deconvolute the detector effects from the inclusive measurement or convolute the detector effects to the background.

It appeared easier to perform the latter. For this, resolution maps have been extracted from full simulations, characterizing the detector resolution (shown in Figure 7.13 c and d). The resolution maps were applied as an after-processing to the electron background simulation by randomly smearing the electron tracks according to the resolution maps. Comparison on the final background electron cocktail level shows that the detector resolution does not significantly change the electron cocktail (shown in Figure 7.13 (f) with blue markers).

7.6.3 Late Electrons

The inclusive electrons are all required to pass a cut asking for hits in the first ITS layer. This cut is supposed to reduce the amount of conversion electrons included in the final sample. Since electrons produced in conversions after the first ITS layer cannot have produced a signal in it.

However it turned out that this is not strictly true because there is a probability to wrongly associate hits in the first ITS layer with tracks of an electron from a later conversion. This probability is especially high at high occupancies in the ITS (central events) and at low momenta. The amount of these late electrons has been calculated in a full simulation for the 0-10% and 20-40% centrality (shown in Figure 7.13 e). Being an effect based on tracking mismatching, it is quite natural that these electrons were additionally found to have a somewhat lower reconstruction resolution than the normal electrons.

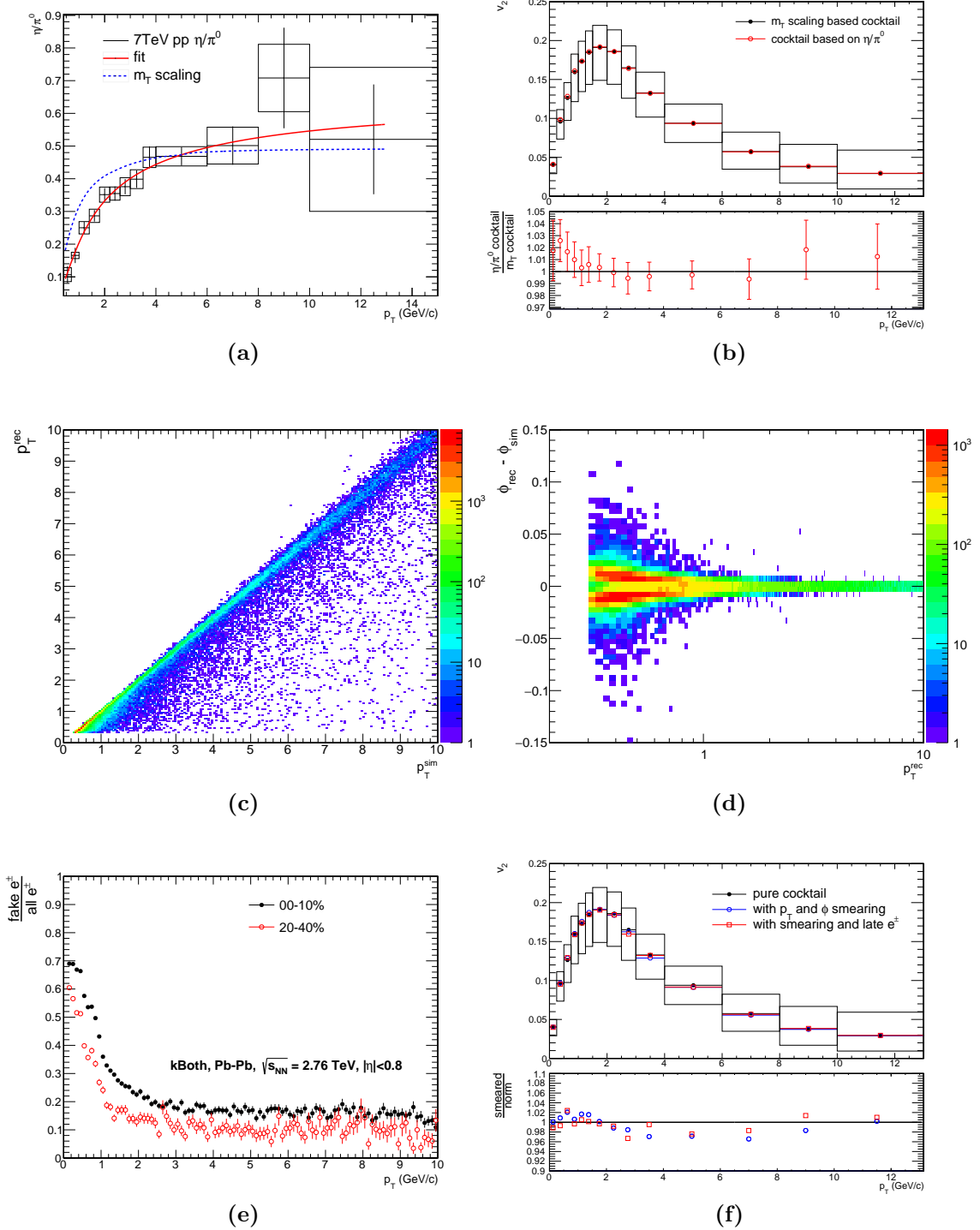


Figure 7.13: Alternative of the estimation of the η momentum spectrum (a) and its effect on the cocktail (b). Electron momentum (c) and ϕ resolution (d), amount of late electrons (e) and their effects on the cocktail (f).

When both effects are taken together, the electron reconstruction resolution and the additional late electrons, no significant deviation outside of the statistical uncertainties can be made out (shown in Figure 7.13 (f) with red markers).

8 Background Subtraction

Having measured the inclusive electron sample in Chapter 6 and having estimated the electron background using the cocktail method in Chapter 7, it is now possible to finally calculate the heavy-flavour-electron elliptic flow by subtracting one from the other.

8.1 Signal-to-Background Ratio

According to Equation 5.1 it is important to determine the ratio of the amount of electrons from heavy flavours (HFE) to the amount of electron from the other sources (non-HFE). This work uses the already available result of this ratio, provided by another analysis. The paper presenting the final ALICE result of the elliptic flow of heavy-flavour electrons [144] is a merger of that analysis and this work. The approach of determining the needed quantity shall now be outlined.

The so-called signal-to-background ratio (R_{SB}) needed to subtract the electron background from the inclusive electron sample is simply given by:

$$R_{SB} = \frac{N_{HFE}}{N_{nonHFE}}$$

While both, the amount of heavy-flavour electrons (N_{HFE}) and the amount of non-heavy-flavour electrons (N_{nonHFE}) cannot be measured directly, only the sum of both is measured by the inclusive sample (N_{incl}):

$$N_{incl} = N_{nonHFE} + N_{HFE}$$

These two expressions can be rearranged to:

$$R_{SB} + 1 = \frac{N_{HFE}}{N_{nonHFE}} + \frac{N_{nonHFE}}{N_{nonHFE}} = \frac{N_{HFE} + N_{nonHFE}}{N_{nonHFE}} = \frac{N_{incl}}{N_{nonHFE}} \quad (8.1)$$

The amount of non-heavy-flavour electrons (N_{nonHFE}), however, can be measured indirectly by an additional analysis step.

8.1.1 Low-Mass Dielectrons

Figure 8.1 (a) shows a typical low-mass dielectron spectrum. It can be seen that the charm ($c\bar{c}$) and beauty ($b\bar{b}$) contribution is dominant at high masses, which is of course rather intuitive considering the high masses of the quarks involved. Towards lower masses, the spectrum is dominated by the contributions of the light-flavour hadrons (π^0 , η , ω , η' , ϕ) which are part of the electron background cocktail calculations presented in Chapter 7. It can be seen that at very low invariant masses ($< 0.1 \text{ GeV}/c^2$) the contribution of charm and beauty is completely outshined by the light hadrons. Thus a sample of reconstructed very low invariant mass electrons will include almost exclusively electrons from the background electron sources.

The analysis of reconstructing these electron pairs exploits the fact that due to the lepton number conservation of the electromagnetic and strong nuclear interactions, the electron pairs produced in particle decays must in fact consist of an

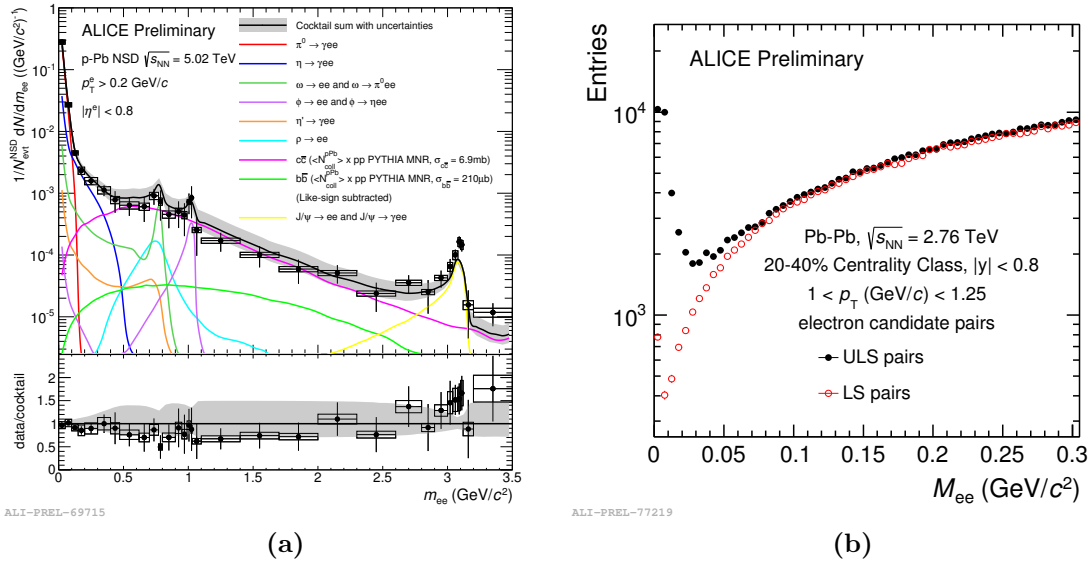


Figure 8.1: Low-Mass dielectron spectrum (a) and the reconstruction of like sign (LS) and unlike sign (ULS) electron pairs (b). Dielectrons of low masses are dominated by the electron pairs from light hadrons.

electron and a positron. All random unlike-sign (ULS) electron pairs of a collision are thus candidates for being products of decayed particles, while like-sign (LS) pairs can only be purely random combination. The mass of the decaying particle is converted into the kinetic energy of the electron pair due to energy conservation, while the total momentum of the pair must correspond to the momentum of the decayed particle. In the rest frame of a particle decaying into an electron pair, momentum conservation further restricts the two electrons to be emitted back-to-back. Transforming into the lab frame, this topology is changed due to the Lorentz boost (see also Chapter 2.2). The relatively low masses of the particles decaying and their relatively high momenta lead to a very small opening angle of the pair as measured in the lab frame. The opening angle cut is a very important measure used in the reconstruction, greatly reducing the number of purely random pairs.

Figure 8.1 (b) shows the reconstructed unlike-sign (ULS) and like-sign (LS) electron pairs. The random combinatorics of electrons not representing a real particle decay can be removed by subtracting the like-sign from the unlike-sign pairs:

$$N_{\text{nonHFE}}^{\text{rec}} = N_{\text{ULS}}^{\text{rec}} - N_{\text{LS}}^{\text{rec}}$$

8.1.2 Reconstruction Efficiency and Resulting R_{SB}

In order for the sample to include only the non-heavy-flavour electrons, and following the previous discussion, a low invariant-mass cut of $< 70 \text{ MeV}/c^2$ is introduced. It is thus clear that the measurement cannot include all produced electron pairs. Furthermore, a real detector is also restricted by its reconstruction efficiency and its geometrical acceptance. The reconstructed sample of pairs thus represents only a

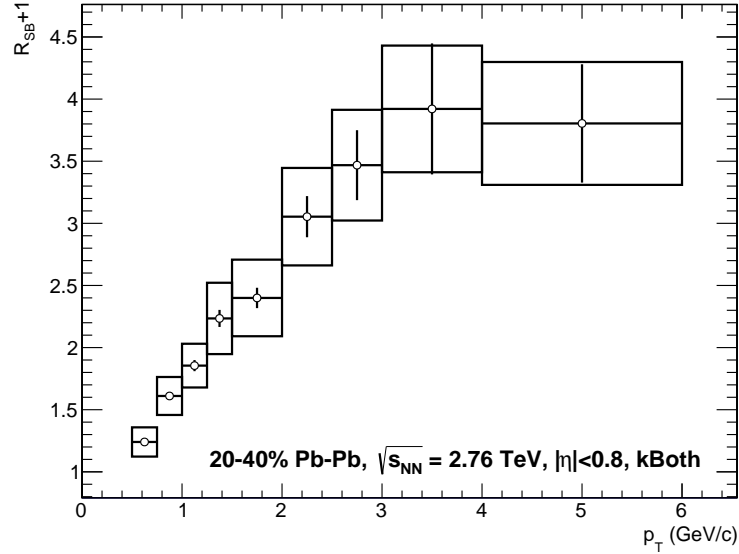


Figure 8.2: Signal-to-Background Ratio

fraction of the pairs produced:

$$\begin{aligned} \varepsilon_{nonHFE}^{rec} \cdot N_{nonHFE} &= N_{nonHFE}^{rec} \\ \Leftrightarrow N_{nonHFE} &= \frac{N_{nonHFE}^{rec}}{\varepsilon_{nonHFE}^{rec}} \end{aligned} \quad (8.2)$$

This non-heavy-flavour reconstruction efficiency ($\varepsilon_{nonHFE}^{rec}$) is computed using a Monte Carlo (MC) calculation. The HIJING [177] Monte Carlo production used (LHC12a17d fix and LHC12a17e fix) is enriched with additional π^0 and η in order to increase the statistics. Following the same argumentation as for the simulation produced for the background cocktail, these additional particles are distributed following a uniform momentum distribution, to not produce a very strongly momentum-dependent statistics. The weights used for the particles follow the mother particle spectra presented in Chapter 7.2. The reconstruction efficiency is calculated by reconstructing the simulated data sample and dividing the momentum spectrum of the reconstructed particles with the spectrum of the simulated particles.

With the non-heavy-flavour electrons determined by using Equation 8.2, it is possible to compute the signal-to-background ratio by using Equation 8.1, which is shown in Figure 8.2.

8.2 Final Result and Discussion

With all ingredients determined, it is now possible to proceed with the subtraction procedure according to Equation 5.1. v_2^{incl} is the elliptic flow of the measured inclusive electron sample as it is shown in Figure 6.10 (a), v_2^{back} is the elliptic flow of the background electrons as shown in Figure 7.12 (c), and R_{SB} is the ratio of heavy-flavour electrons to the non-heavy-flavour electrons which is shown in Figure

8.2. Although not explicitly stated in the expression, all the variables are thus momentum dependent. The elliptic flow of the heavy-flavour electrons (v_2^{HFE}) is shown in Figure 8.3 (a). It is superimposed to the v_2^{incl} and v_2^{back} . The errors of the input variables have been propagated to the output using a numerical estimation of the second-order approximation to the full propagation (see Chapter 10.7 for details). The result shows a heavy-flavour electron v_2 significantly above 0, at significance level of over 4σ in the centralities 20-40% and 10-20%. It is below the v_2 of both, the non-heavy-flavour background and the inclusive electrons and it is decreasing with p_T and centrality in parallel to both. In the lower momentum range, the dominant contribution is expected to be coming from charm quarks, and in the higher momentum region from beauty.

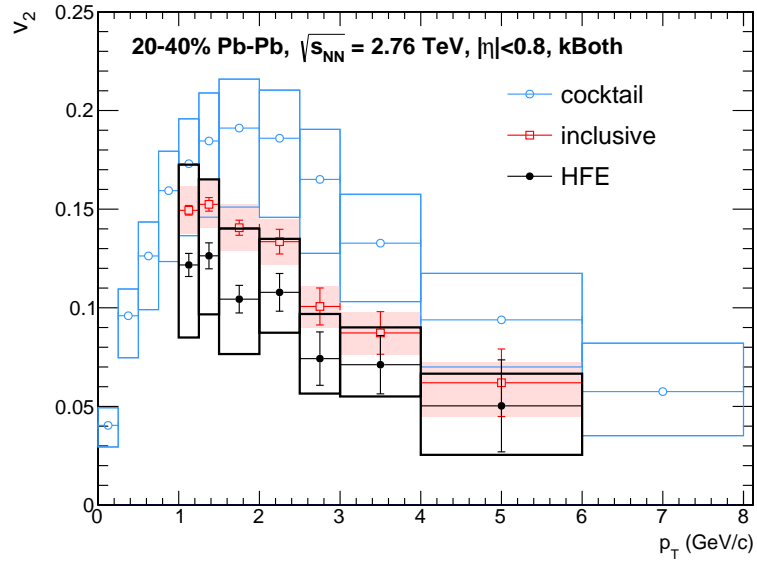
In the hydrodynamic picture, this suggests that at least the charm quarks do also participate in the collective expansion of the medium together with the light flavours, which hints to considerable interaction with the medium, confirming the observations from the R_{AA} measurements [126–129]. Since most heavy quarks should be produced early in the initial hard scatterings, and due to the so-called “dead cone effect”, where the gluon radiation of high-mass partons should be drastically suppressed [178, 179], heavy quarks should neither already be thermalized at the time the medium builds up, nor should they become thermalized on the time scale of the lifetime of the medium [180]. Thus the findings of the measurements are rather surprising. This result is also consistent with the ALICE measurements of the flow of D mesons [141, 142] and of heavy-flavour muons [143] at forward rapidity and with the previous results from RHIC [124, 140].

8.2.1 Comparison to Model Calculations

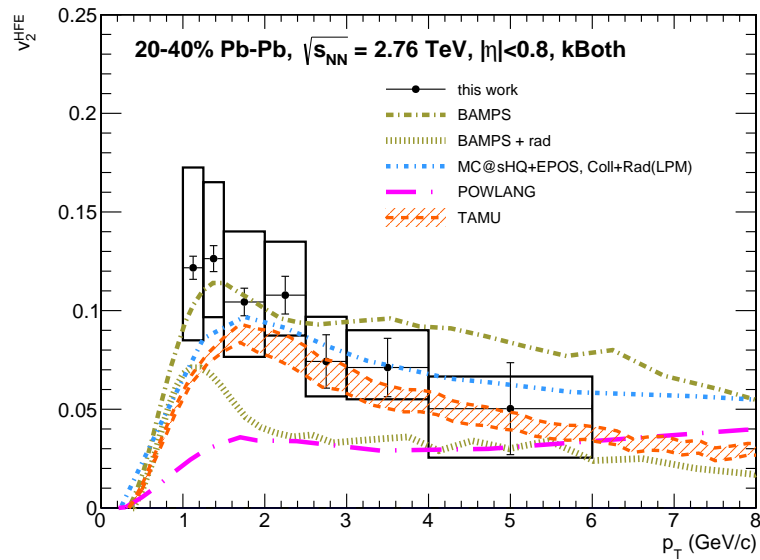
Figure 8.3 shows the comparison of the measurement with the following theoretical model calculations:

BAMPS is a partonic transport model, simulating the 3+1D space-time evolution of multi-parton scatterings in the QGP by solving the Boltzmann equation. All interaction processes of light partons are included. The two versions provided differ in the treatment of the heavy flavours: The model “BAMPS” includes only the binary elastic collisions, with the cross-sections scaled to roughly match the contribution of radiative processes, which are not included. The model “BAMPS + rad” is an update to the first, adding a full treatment of the relevant radiation processes. The running coupling is explicitly taken into account for all interactions modelled. Both models use vacuum fragmentation functions. [181, 182]

MC@sHQ+EPOS is a perturbative QCD model including interactions from collisional energy loss in a 3+1D fluid-dynamical expanding medium, radiative interactions with high-energy corrections due to the QCD analogon of the Landau-Pomeranchuk-Migdal effect with a running coupling. Initial conditions are obtained from a flux-tube approach (EPOS). The hadronization takes place at the transition temperature, via coalescence and fragmentation. [183]



(a)



(b)

Figure 8.3: Elliptic flow of heavy-flavour electrons compared with the inclusive measurement and the background cocktail (a) and compared with model calculations (b). The figures of the other centralities analysed are attached in the appendix (Figure 10.5 and Figure 10.6).

POWLANG is a pQCD event generator (POWHEG) at next-to-leading order (NLO) accuracy with CTEQ6M parton distribution functions corrected by EPS09 nuclear modifications, interfaced with a PYTHIA parton shower which is iteratively transported through an expanding viscous hydrodynamical background medium based on the relativistic Langevin equation. Fragmentation is based on vacuum fragmentation functions. [184, 185]

TAMU is a non-perturbative heavy-flavour transport model based on a Fokker-Planck Langevin dynamics with strong coupling by resonance formation and dissociation in a 2+1D evolving tuned ideal hydrodynamic medium constrained by measured light-hadron spectra. Energy loss is based on elastic processes in the partonic stage and by diffusion in the hadronic stage. The hadronization includes a component of recombination of the heavy quarks with light-flavour hadrons in the QGP. [186]

Models which quantitatively describe the elliptic flow of heavy-flavour electrons well, do also describe the elliptic flow of D mesons [141, 142] and heavy-flavour muons [143]. Together with the heavy-flavour R_{AA} measurements [126–129], the elliptic flow from heavy flavours constrain the current models.

8.3 Outlook

The ALICE experiment is going to receive significant upgrades in the upcoming years. The upgrade will include the following hardware changes [103, 187]:

- a new beam pipe with smaller diameter to allow the first ITS layer to move nearer to the interaction point
- a new high-resolution ITS detector with decreased radiation length
- a new high-speed TPC with continuous read out
- upgrade of the readout electronics of the TRD, TOF and the Muon Spectrometer for high-rate operation
- upgrade of the forward detectors

The upgrade of the TPC will replace the wire chamber layout with a layout based on Gas Electron Multipliers (GEMs). Through the possibility of continuous operation it will increase the maximal readout rate to 50kHz. This will provide a luminosity increase of an order of magnitude, increasing the statistics respectively. The increase in resolution of the new ITS will provide the possibility of better signal-to-background ratios. Its lower radiation length will decrease the contribution of conversion electrons and the movement of the first layer nearer to the interaction point will increase the separation possibility between primary and secondary particles. All these changes will contribute to a significant reduction of the systematic uncertainties. With these upgrades it will be possible to perform this analysis additionally discriminating between charm and beauty contributions. This would be of utmost interest since in the bottom sector the contribution of secondary processes is expected to be insignificant.

9 Summary

The LHC particle accelerator was built to find answers to current most fundamental questions of particle physics and astrophysics. Its four main experiments have been developed with different emphasis on these questions. The general-purpose experiment ALICE was built with a focus to study the properties of the condensed matter which is generated in the heavy-ion collisions. It is the state of matter of the highest temperatures and pressures, naturally existing only in the most extreme events known: In supernova explosions and during the first microsecond at the beginning of our universe, right after the Big-Bang. This state of matter is characterized by the disintegration of the atomic nucleus into its nucleons and further into its component partons, called quarks and gluons. Borrowing from its electromagnetical equivalent, this state of matter is referred to as quark-gluon plasma (QGP).

Being produced mostly at the very first instant of a heavy-ion collision, heavy quarks are a unique probe for studying the properties of the QGP. The interactions with the surrounding medium can be expressed by radiative and collisional energy loss. An efficient way to study heavy quarks is via their decay electrons, which can leave the strongly interacting QGP mostly unobstructed. Through measurements of collective phenomena, it was found that the QGP can be described to very high accuracy by a strongly interacting fluid.

The collective motion of the particles inside the medium can be analyzed by a Fourier decomposition of the azimuthal anisotropic particle distribution. Elliptic flow is the component of the collective motion characterized by the second harmonic moment of this decomposition. It is a direct consequence of the initial geometry of the collision which is translated to a particle number anisotropy due to the strong interactions inside the medium. The amount of elliptic flow of low-momentum heavy quarks is related to their thermalization with the medium, while high-momentum heavy quarks provide a way to assess the path-length dependence of the energy loss induced by the interaction with the medium.

The analysis is based on a three-step procedure: Inclusive electron measurement, estimation of the background electrons and subtraction of the background from the inclusive measurement. The first part of the thesis describes the inclusive electron measurement. The elliptic flow was measured using two of the most widely used methods: the event-plane method and the scalar-product method. A very good agreement was found with insignificant differences between both methods. Due to its particle-identification capabilities, the ALICE experiment is especially suited for these kind of electron measurements. This work is based on a particle identification (PID) using the Time-Projection Chamber (TPC), the Inner Tracking System (ITS) and the Time-Of-Flight detector (TOF). To increase the electron purity as much as possible, only high-quality runs were included in the analysis, rejecting runs with any detector issues. The available calibration of the TPC signal was further improved to provide accurate PID cuts, rejecting as much contamination as reasonably possible. Custom data fitting procedures were implemented to estimate the remaining contamination of the electron sample, which was finally subtracted from the measurement.

The second part presents a method of calculating the electron background. Here

the electrons from light hadrons and direct photons are evaluated in a simulation of the respective particle decays. The necessary inputs to the simulation are previous ALICE measurements of the momentum and elliptic flow spectra of charged pions and direct photons. The spectra of other relevant light hadrons are based on m_T and KE_T scaling of the pion spectra. The virtual photons are based on the real photon measurement taking into account the increasing probability of leptonic pair production with increasing available energy. Electrons are generated using PYTHIA6 as a decayer and electrons from gamma conversions are handled by a custom implementation of GEANT4 code providing a fast simulation. The spectra of electrons from the different sources are extracted from the simulation and added to produce the background electron cocktail. Additional systematic studies were conducted to prove the stability of the resulting cocktail spectra under different assumption.

The final result of this work emerges by subtracting the background electron cocktail from the inclusive electron measurement. The result shows a positive elliptic flow decreasing with p_T and towards more central collisions, which is in line with expectations based on hydrodynamics. This is consistent with the fact that charm participates to the expansion of the medium at low momenta. At high momenta, the expected path-length dependence of the heavy-quark energy loss from model calculations results in a small positive elliptic flow, which is consistent with the measurements within systematic errors. The dominant contribution at low momenta is expected to come from charm, while at higher momenta from bottom quarks. This confirms previous results of the direct measurements of charm hadrons and measurements of heavy-flavour decay muons at forward rapidity. Compared to results from RHIC the elliptic flow of heavy quarks seems not have increased any further.

Thanks to the increase in statistics, the improvement of the ITS and the TPC and the availability of a full Transition Radiation Detector (TRD), it can be expected that future periods of the Pb-Pb data taking, results separating charm and beauty will be reachable.

10 Appendix

10.1 Potential Energy

In order to describe the behaviour of the forces it is necessary to introduce some basic physics concepts. The interaction between particles is described by a force field $\vec{F}(\vec{x})$, which is a vector field. The work W is then given by the line integral along the path of movement C :

$$W(C) = \int_C \vec{F}(\vec{x}) \cdot d\vec{x}$$

If this integral is independent of the path, then the field is called a conservative force field. In this case the work is only dependent on the starting and end point of the path (\vec{a} and \vec{b}), which means that no work is done on any closed path:

$$W(\vec{a}, \vec{b}) = \int_{\vec{a}}^{\vec{b}} \vec{F}(\vec{x}) \cdot d\vec{x}$$

$$\oint_C \vec{F}(\vec{x}) \cdot d\vec{x} = 0$$

In this case it is possible to define a scalar field V called potential, such that:

$$\vec{F}(\vec{x}) = \vec{\nabla}V(\vec{x}) \quad , \quad \vec{\nabla} = \begin{pmatrix} \frac{\partial}{\partial x} \\ \frac{\partial}{\partial y} \\ \frac{\partial}{\partial z} \end{pmatrix}$$

Work is then given simply by the difference of the potentials at the starting and end points and is called potential energy:

$$W_{pot}(\vec{a}, \vec{b}) = \int_{\vec{a}}^{\vec{b}} \vec{F}(\vec{x}) \cdot d\vec{x} = V(\vec{b}) - V(\vec{a})$$

In case it is possible to simplify the problem further, such that the field is not dependent of the position but only on the distance to the origin, the field is then called a central force field with a central force potential.

$$\vec{F}(r) = \vec{\nabla}V(r)$$

$$W_{pot}(r_a, r_b) = \int_{r_a}^{r_b} \vec{F}(r) \cdot dr = V(r_b) - V(r_a)$$

The potential energy is usually defined relative to a point at $r = \infty$ at which the potential energy is zero:

$$W_{pot}(r) := \int_r^{\infty} \vec{F}(r') \cdot dr' = V(\infty) - V(r) = 0 - V(r) = -V(r)$$

10.2 Radiation Length and Pair Production

The passage of particles through the detector material is important to consider. High energy electrons lose energy by bremsstrahlung and high energy photons can convert into electron-positron pairs. The relevant scale of the probability to do so is given by the radiation length X_0 . The radiation length represents 7/9 of the mean free path of the photon and the distance where the electron has lost $1 - 1/e \approx 0.63$ of its energy. By the choice of materials detectors are made such that the actual radiation length inside the detector X is only a fraction of the total radiation length X_0 . The probability of a pair production is thus given by:

$$p_{pair} = 1 - \exp\left(-\frac{7}{9} \cdot \frac{X}{X_0}\right)$$

The nominal radiation length X/X_0 is usually given for particles travelling perpendicular to the detector material, having a minimal path length through the material (x_0). For the central barrel this means for particles with pseudorapidity $\eta = 0$. Particles at other pseudorapidity will have an increased path length through the material (x):

$$\frac{x(\theta(\eta))}{x_0} = \frac{1}{\sin(\theta(\eta))}$$

The dependence between θ and η is given by Equation 2.11. For this analysis the pseudorapidity range is $|\eta| < 0.8$. In this range the particle production can be assumed to be rapidity independent and thus the mean excess path length of the particles can easily be calculated:

$$\frac{\bar{x}}{x_0} = \frac{1}{2\eta} \int_{-\eta}^{\eta} \frac{1}{\sin(\theta(\eta))} = \frac{1}{2} \frac{\exp(\eta) - \exp(-\eta)}{\eta}$$

In this case the mean probability of a pair production is given by:

$$\bar{p}_{pair} = 1 - \exp\left(-\frac{7}{9} \cdot \frac{X}{X_0} \cdot \frac{\bar{x}}{x_0}\right)$$

This probability is true only for photons with infinite momentum. Photons with a finite momentum will have an additional multiplicative probability component which is dependent on the photon momentum and the material Z . For photons above $1 \text{ GeV}/c$ this component is approximately 1.

10.3 Random Number Sampling

In Monte-Carlo simulations it is usually of need to generate a random number according to a given distribution. In this work this could usually be done relying onto the capabilities of the ROOT framework. The method used is a numerical inverse transform sampling working in small bins.

10.3.1 Inverse Transform Sampling

The primary observation used is that, if x is a random variable with cumulative distribution F , then $y = F(x)$ is a uniform random variable with support $[0, 1]$. Thus a random variable can be generated having a given probability density f , by generating a uniform random variable y with support $[0, 1]$ and using the inverse of the cumulative distribution to get $x = F^{-1}(y)$. This works only when the cumulative distribution F is invertible. Apart from some pathological cases this can however always be done in small bins with converging quality of the approximation of F with a simple polynomial. Thus F must be a real analytic function.

10.3.2 Rejection Sampling

In cases when F^{-1} is sufficiently complicated to evaluate, a different method might be of use: It may be possible to define an envelope e to f such that it remains sufficiently near, and has an invertible cumulative distribution E which is easily evaluable. In such a case the sampling can be performed exactly like for the inverse transform sampling: $x = E^{-1}(y)$ with y being generated according to a uniform distribution with support $[0, 1]$. Additionally the value x thus found must now be rejected with a probability representing the amount the envelope e overestimates the density f at this value x . This can be achieved by drawing an additional random variable t from a uniform distribution with support $[0, x]$. x is then rejected whenever $t > f(x)$.

10.4 Parametric Distribution Functions

The distribution of large data samples can often be described by a Gaussian. This empirical finding is mathematically explained by the central limit theorem. However, in real world data and when high precision is necessary, distributions can significantly deviate from Gaussian distributions. They can be skewed, be leptokurtic or platykurtic. This paragraph will introduce two distribution functions: One which can transition from a Gaussian into a skewed version of the Gaussian, and another building on top of the first one, with additionally variable excess kurtosis.

The Pearson distribution family [188–190] is not an option. Since an unbound support is necessary, the only possibility would be the Pearson IV function. However this function cannot reach into the negative excess kurtosis region (platykurticity). The situation is thus similar to the other candidate, the Johnson SU distribution family [191]. There the reachable skewness is additionally increasingly limited with decreasing kurtosis (going from leptokurtic to mesokurtic).

10.4.1 Skewed Gaussian

The first function is the skewed normal distribution ($\phi_\alpha(x)$) which was first suggested by O'Hagan and Leonard [192]. The distribution is constructed from the normal distribution ($\phi(x)$) and the cumulative normal distribution ($\Phi(x)$):

$$\phi(x) = \frac{\exp(-x^2/2)}{\sqrt{2\pi}}$$

$$\Phi(x) = \int_{-\infty}^x \phi(t) dt = \frac{1}{2} \left(1 + \operatorname{erf} \left(\frac{x}{\sqrt{2}} \right) \right)$$

$$\phi_\alpha(x) = 2\phi(x)\Phi(\alpha x)$$

Location (ξ) and scale (ς) are added similarly as for the Gaussian itself:

$$\phi(x) \rightarrow \phi_{\xi,\varsigma}(x) = \frac{\phi\left(\frac{x-\xi}{\varsigma}\right)}{\varsigma} = \frac{\exp\left(-\frac{(x-\xi)^2}{\varsigma^2}\right)}{\varsigma \cdot \sqrt{2\pi}}$$

$$\Phi(x) \rightarrow \Phi_{\xi,\varsigma}(x) = \Phi\left(\frac{x-\xi}{\varsigma}\right) = \frac{1}{2} \left(1 + \operatorname{erf} \left(\frac{x-\xi}{\varsigma \cdot \sqrt{2}} \right) \right)$$

$$\Rightarrow \phi_{\xi,\varsigma,\alpha}(x) = 2\phi_{\xi,\varsigma}(x)\Phi_{\xi,\varsigma}(\alpha x)$$

The parameter α is responsible for changing the asymmetry of the distribution, however it simultaneously also has effects on the position and the width. This is highly unsatisfactorily because it means that the parameters are not orthogonal. Such functions are not very well suited as fitting functions because the correlations between the parameters make the minimization process of the fitting algorithm very hard. Luckily it is possible to orthogonalize the parameters, simply by requiring the location (ξ) and scale (ς) to coincide with the mean (m) and standard deviation (σ) respectively. It thus remains only to calculate the mean and sigma of the skewed Gaussian $\phi_{\xi,\varsigma,\alpha}(x)$:

$$m_{\xi,\varsigma,\alpha} - \xi = m_{0,\varsigma,\alpha} = \int_{-\infty}^{\infty} x \phi_{0,\varsigma,\alpha}(x) dx = \frac{\alpha \cdot \varsigma}{\sqrt{1 + \alpha^2}} \sqrt{\frac{2}{\pi}} \quad (10.1)$$

$$\frac{\sigma_{\varsigma,\alpha}^2}{\varsigma^2} = \sigma_{1,\alpha}^2 = \int_{-\infty}^{\infty} x^2 \phi_{0,1,\alpha}(x) dx - \left(\int_{-\infty}^{\infty} x \phi_{0,1,\alpha}(x) dx \right)^2 = 1 - m_{0,1,\alpha}^2 = 1 - \frac{2\alpha^2}{(1 + \alpha^2)}$$

The parameters can finally be orthogonalized with the following two substitutions:

$$\xi \rightarrow m - m_{0,\varsigma,\alpha} \quad , \quad \varsigma \rightarrow \frac{\sigma}{\sigma_{1,\alpha}}$$

The skewed Gaussian with uncorrelated parameters is thus:

$$\hat{\phi}_{m,\sigma,\alpha}(x) = \phi_{\{m - m_{\{0, \frac{\sigma}{\sigma_{1,\alpha}}, \alpha\}}, \frac{\sigma}{\sigma_{1,\alpha}}, \alpha\}}(x)$$

For $\alpha = 0$ this distribution is identical to the Normal distribution. The parameter α does not represent directly the skewness, it is however perfectly correlated to it. The skewness, a.k.a. the third standardized moment $\gamma_1 = \mu_3/\sigma^3$, can be changed in the interval $\gamma_1 \in] -1..1[$.

10.4.2 “Variakurtic” Skewed Gaussian

In some situations more general distributions are needed, where the kurtosis is also variable in addition to the location, width and skewness. The suggested “variakurtic” skewed Gaussian is based on the first version of the generalized Gaussian [193]. This is a symmetric distribution with a kurtosis parameter (β):

$$\phi_{\beta}(x) = \frac{\beta \cdot \exp(-|x|^{\beta})}{2 \cdot \Gamma(1/\beta)}$$

$$\Phi_{\beta}(x) = \int_{-\infty}^x \phi_{\beta}(t) dt = \frac{1}{2} + \text{sign}(x) \cdot \frac{\gamma(1/\beta, |x|^{\beta})}{2 \cdot \Gamma(1/\beta)}$$

With $\gamma(x, y)$ being the lower incomplete gamma function. Location (ξ) and scale (ζ') are added as for the Gaussian:

$$\phi_{\beta}(x) \rightarrow \phi_{\xi, \zeta', \beta}(x) = \frac{\phi_{\beta}\left(\frac{x-\xi}{\zeta'}\right)}{\zeta'} = \frac{\beta \cdot \exp\left(-\left|\frac{x-\xi}{\zeta'}\right|^{\beta}\right)}{2 \cdot \zeta' \cdot \Gamma(1/\beta)}$$

$$\Phi_{\beta}(x) \rightarrow \Phi_{\xi, \zeta', \beta}(x) = \Phi_{\beta}\left(\frac{x-\xi}{\zeta'}\right)$$

It is important to note that the width is influenced by β already at this stage. Before continuing this must be corrected for:

$$\zeta' \rightarrow \zeta \cdot \sqrt{\frac{\Gamma(1/b)}{\Gamma(3/b)}}$$

$$\Rightarrow \hat{\phi}_{\xi, \zeta, \beta}(x) = \phi_{\{\xi, \zeta \sqrt{\frac{\Gamma(1/b)}{\Gamma(3/b)}}, \beta\}}(x) \quad , \quad \hat{\Phi}_{\xi, \zeta, \beta}(x) = \Phi_{\{\xi, \zeta \sqrt{\frac{\Gamma(1/b)}{\Gamma(3/b)}}, \beta\}}(x)$$

Using this generalized Gaussian instead of the Normal distribution as a base for constructing the skewed Gaussian generates the suggested “variakurtic” skewed Gaussian:

$$\phi_{\xi, \zeta, \alpha, \beta}(x) = 2\hat{\phi}_{\xi, \zeta, \beta}(x)\hat{\Phi}_{\xi, \zeta, \beta}(\alpha x)$$

Similarly to the skewed Gaussian the parameters α and β have considerable crosstalk to the position and width but also among themselves. A stringent resolution of this situation is however much more complicated in this case, since the integral in the equivalent calculation to Equation 10.1 appears to not be analytically solvable. It is however possible to reach an approximated solution for the correction of location and scale by integrating a Taylor expansion of the problem in β around the point of no excess kurtosis. With increasing order the integrals get increasingly more complicated such that it was only possible to find an analytic solution up to the linear term. The quadratic term was found numerically. Due to the length of the numerical solution however, only the first two terms of the Taylor expansion are presented:

$$m_{0, \zeta, \alpha, \beta} = \frac{\alpha \cdot \zeta}{\sqrt{1 + \alpha^2}} \sqrt{\frac{2}{\pi}} + \frac{\beta - 2}{\zeta^{-1}} \left[\frac{3(1 + \alpha^2)(1 + \ln(1 + \alpha^2)) - 2\alpha^2 \ln \alpha}{\alpha^{-1} \cdot (1 + \alpha^2)^{3/2} 2\sqrt{2\pi}} - \frac{4 \sinh^{-1} \alpha}{2\sqrt{2\pi}} \right]$$

$$\begin{aligned} \frac{\sigma_{\zeta,\alpha,\beta}^2}{\zeta^2} &= \sigma_{1,\alpha,\beta}^2 = 1 - m_{0,1,\alpha,\beta}^2 \\ \Rightarrow \xi &\rightarrow m - m_{0,\zeta,\alpha,\beta} \quad , \quad \zeta \rightarrow \frac{\sigma}{\sigma_{1,\alpha,\beta}} \\ \Rightarrow \hat{\phi}_{m,\sigma,\alpha,\beta}(x) &= \phi_{\{m - m_{\{0, \frac{\sigma}{\sigma_{1,\alpha,\beta}}, \alpha, \beta\}}, \frac{\sigma}{\sigma_{1,\alpha,\beta}}, \alpha, \beta\}}(x) \end{aligned}$$

For $\beta = 2$ the distribution is identical to the skewed Gaussian. The parameters α and β are responsible for skewness and kurtosis but are somewhat correlated. This can be resolved with a numerical mapping between them and skewness and kurtosis. The kurtosis can range from extremely leptokurtic over mesokurtic to moderately platykurtic. The useful skewness range of the distribution is increasingly limited with increasing platykurticity.

10.5 Feature Detection

Feature detection is a term in image processing referring to algorithms used for detecting specific features of images. The features needed to be detected are so-called blobs, these are regions that have significantly different properties than the surrounding. The method used is the so-called Laplacian of the Gaussian. The input image is blurred by a Gaussian kernel with a radius bigger than one pixel. Finally the Laplace operator is applied to the image:

$$\Delta I = \nabla^2 I = \frac{\partial^2 I}{\partial x^2} + \frac{\partial^2 I}{\partial y^2}$$

While the derivative is defined as a pixel operation:

$$\begin{aligned} \frac{\partial}{\partial x} I(x_i, y_j) &= \frac{I(x_{i+1}, y_j) - I(x_{i-1}, y_j)}{2} \\ \frac{\partial}{\partial y} I(x_i, y_j) &= \frac{I(x_i, y_{j+1}) - I(x_i, y_{j-1})}{2} \end{aligned}$$

The result of this method is a high-contrast image where detected regions are marked by a high intensity compared to a flattened low-intensity surrounding.

10.6 FAST-ELTS: An Efficiency Regaining Fast Least Trimmed Squares Fitter

The ROOT software package provides several fitting algorithms, some intended for general fitting and one for robust fitting. However, the general fitters are much more flexible than the robust fitter, in the sense that the robust fitter puts restrictions in the functional form of the fitting function and cannot be used with general forms or with external function (as needed for fitting arbitrary functions defined in external libraries). The situation was resolved by implementing a robust fitter around the already existing general fitters.

The fitter is a custom three-step implementation based on a combination of the two-step FAST-LTS algorithm by Rousseeuw and Driessen (2006) [194] and the efficiency regaining step ELTS(n) published by Doornik (2011) [195].

The initialization step selects the non-robust least squares minimum-residual subset from a probabilistic minimal choice of points. The number of points in each subset is taken such that the least squares problem is not underdetermined. The number of subsets drawn from the given set of points is calculated depending on the expected maximal contamination of the original set and the amount of points needed in each subset such that there is a high probability to have at least one subset without any contamination.

Based on the initialization with a minimal number of points the second step tries to find all other not contaminated points by minimizing the total χ^2 of non-robust fits on maximal subsets of permutations of points sorted by the residual. The size of the subset is given by the expected maximal contamination, with all other points with greater residual presumably being the contamination.

Often there is no good way to have an accurate expectation on the amount of contamination. In such cases it is safe to assume the maximal possible contamination of up to 50%. However, whenever the contamination is much lower the efficiency of the fit would be unnecessarily low. In this case the last step can now try to include as many points as possible without letting the fit deteriorate.

10.7 Error Propagation

Nothing really existing is truly perfect. Perfection is only an idealisation of the world. This Plato inspired statement extends to physical experiments and has a direct impact on the workflow of the experimentalist (thought experiments like the ones extensively and famously utilised by Einstein being of course the noteworthy exception). Any result measured will be influenced by the deviations of the actually existing setup to the conceptual perfection. It is thus paramount to not only arrive to a result, but to also consider the inherent uncertainties and propagate them to this final result. This leads to a probability statement of the region around the measurement value. Thanks to the central limit theorem, the probability distribution of a final value will very often be approximately normally distributed. The size of the uncertainty is commonly quoted as the size of one standard deviation.

It is possible to propagate the uncertainties of the input variables X_i to the output variable Y of a calculation by the following expression [196]:

$$f_Y(y) = \int \dots \int dx_1 \dots dx_n \cdot \delta(y - Y(x_1, \dots, x_n)) \cdot f_{X_1}(x_1) \dots f_{X_n}(x_n)$$

with $f_A(a)$ being the probability density of the random variable A being evaluated at a . While the propagation is thus fully determined, finding a solution can be a lengthy task. However, it is possible to reach an approximate solution by a simulation: The input variables are then randomly drawn from their probability distribution and the output variable is saved in a histogram. Whatever way is proceeded, it is clear that the underlying distribution functions of all input variables are needed in any case. This is a stronger precondition than it might appear. When the input variables are not under direct control, the underlying distributions might simply not be known. Very often it is the case that the only information at hand is the mean and an uncertainty interval. Of course it would be possible to simply assume normal

distributions to recover the previous expression, however it appears unreasonable to proceed with the full complexity of this solution given that the actual distributions are guessed.

10.7.1 Linear Approximation

A very often used method for the propagation of uncertainties is based on a first order expansion of $Y(\mathbf{X})$ around the expectation values of the X_i . With the correlation coefficient ρ_{ij} of the input variables X_i and X_j and their standard deviations σ_i and σ_j respectively, this yields:

$$E[Y] = Y(E[X_1], \dots, E[X_n])$$

$$\sigma_Y^2 = \sum_i \left(\frac{\partial Y}{\partial x_i} \right)^2 \sigma_i^2 + 2 \sum_{l < m} \left(\frac{\partial Y}{\partial x_l} \right) \left(\frac{\partial Y}{\partial x_m} \right) \rho_{lm} \sigma_l \sigma_m$$

While this can be easily computed for any expression, it can also be numerically estimated to high accuracy: Observing the variations $\Delta_{\pm i}$ of Y due to variations of the input X_i by an amount of $\pm 1\sigma_{X_i}$ around $E[X_i]$:

$$\Delta_{+i} = Y(E[X_1], \dots, E[X_i] + \sigma_i, \dots, E[X_n]) - E[Y]$$

$$\Delta_{-i} = E[Y] - Y(E[X_1], \dots, E[X_i] - \sigma_i, \dots, E[X_n])$$

If $\Delta_{+i} \approx \Delta_{-i} = \Delta_i$ does not hold for any i , than the linear approximation cannot be used. In case it can be used the standard deviation of the output variable can be written as:

$$\sigma_Y^2 = \sum_i \Delta_i^2 + 2 \sum_{l < m} \rho_{lm} \Delta_l \Delta_m$$

10.7.2 Deviations from Linearity

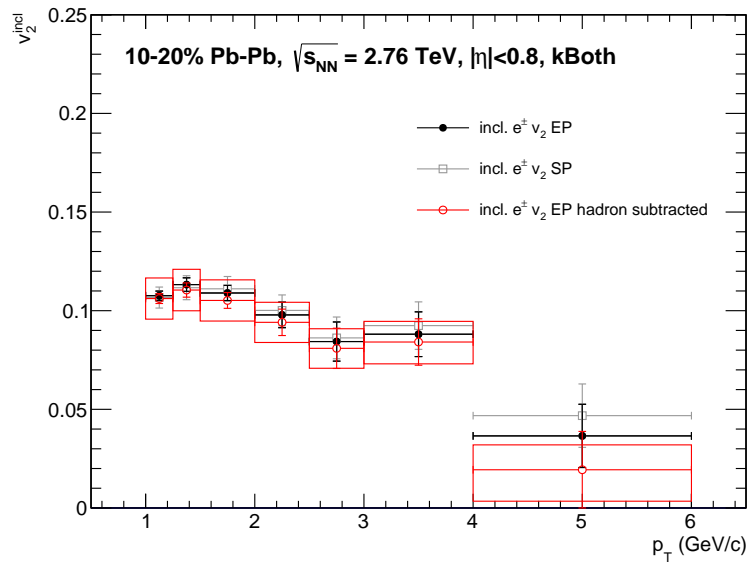
When $\Delta_{+i} \approx \Delta_{-i}$ does not hold, the linearity assumption cannot be further sustained and the expansion of $Y(\mathbf{X})$ must be extended to the second term. It can be shown [196] that a numerical estimation to the second order approximation is given by:

$$E[Y] \approx Y(E[X_1], \dots, E[X_n]) + \sum_i \bar{\Delta}_i$$

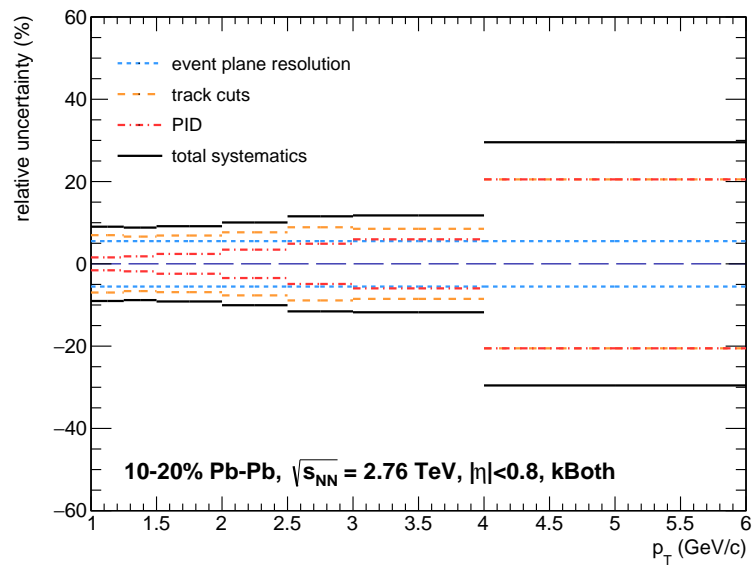
$$\sigma_Y^2 \approx \sum_i \bar{\nabla}_i^2$$

with $\bar{\Delta}_i = (\Delta_{+i} - \Delta_{-i})/2$ and $\bar{\nabla}_i = (\Delta_{+i} + \Delta_{-i})/2$. Due to the noticeable departure from linearity of Equation 5.1 for relatively small values of R_{SB} in comparison to relatively large uncertainties (see also Figure 8.2), this procedure was adopted to calculate the size of the errorbars throughout this work.

10.8 Figures for the Centralities 0-10% and 10-20%

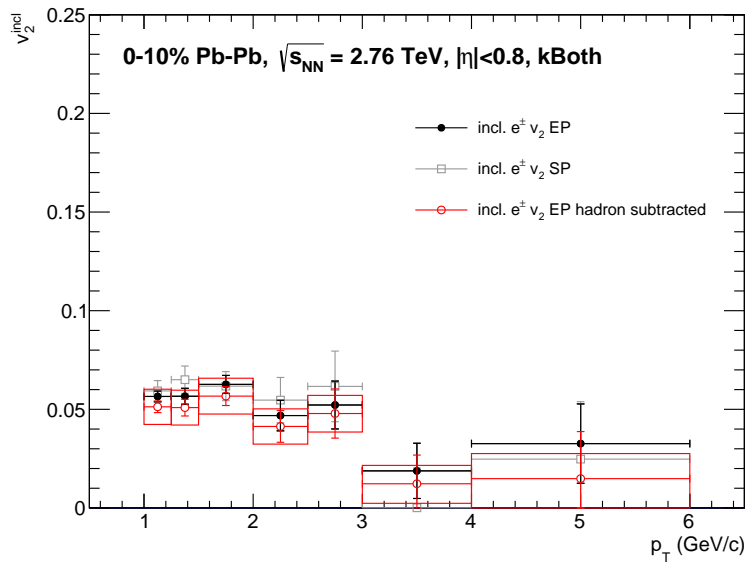


(a)

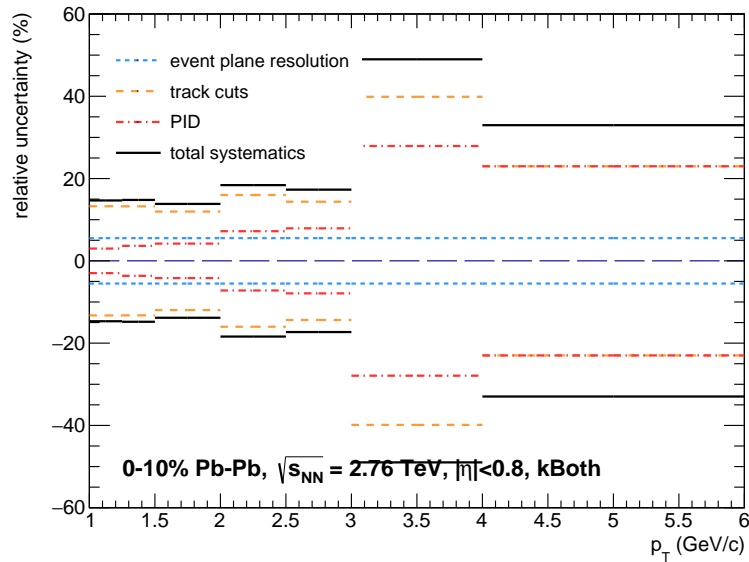


(b)

Figure 10.1: Inclusive electron elliptic flow (a). The total systematic uncertainty and the contributions to it (b).



(a)



(b)

Figure 10.2: Inclusive electron elliptic flow (a). The total systematic uncertainty and the contributions to it (b).

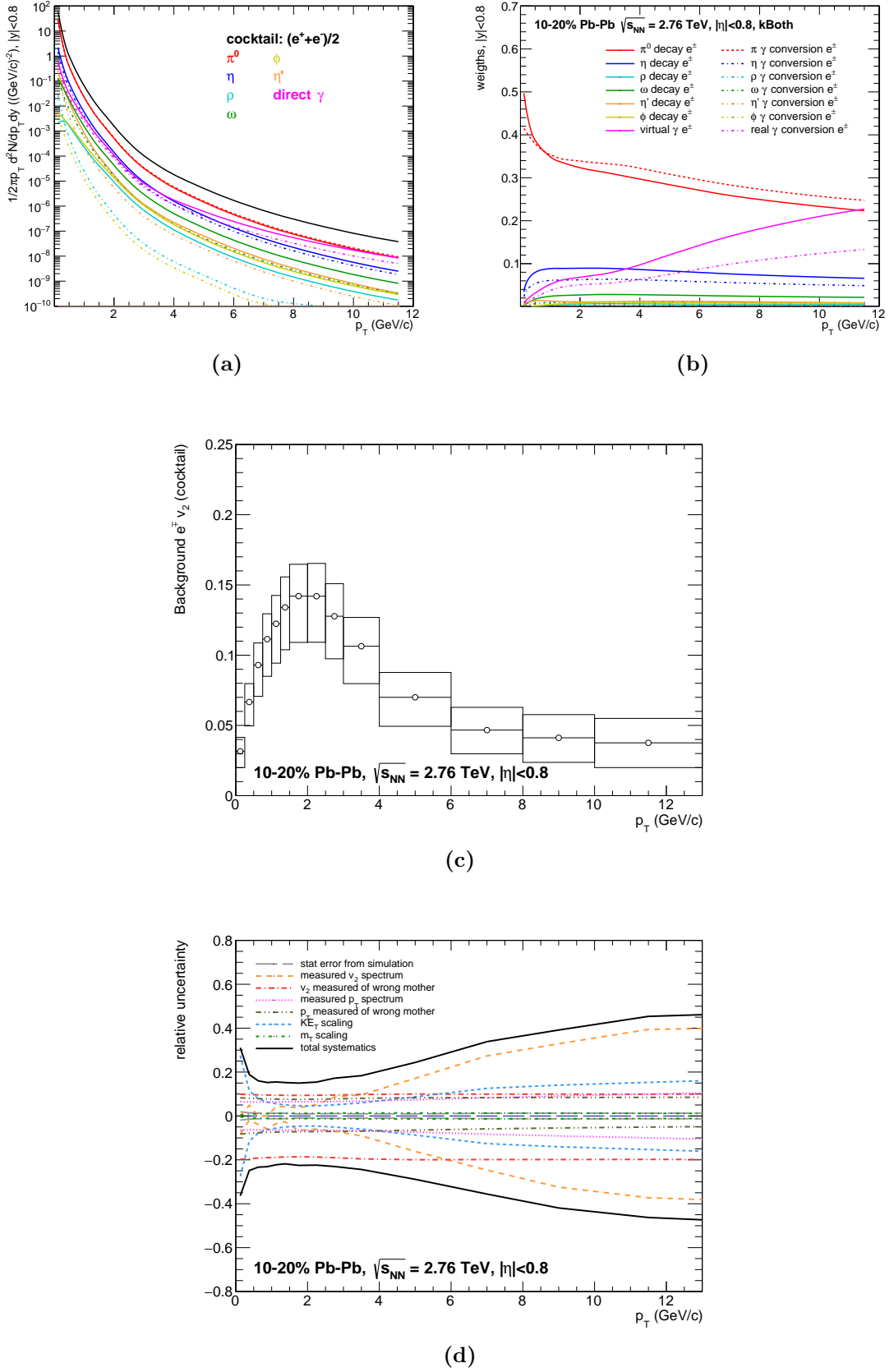


Figure 10.3: Absolute (a) and relative (b) p_T spectra of simulated electrons. The background electron elliptic flow (c) and the constituents of its systematic error (d).

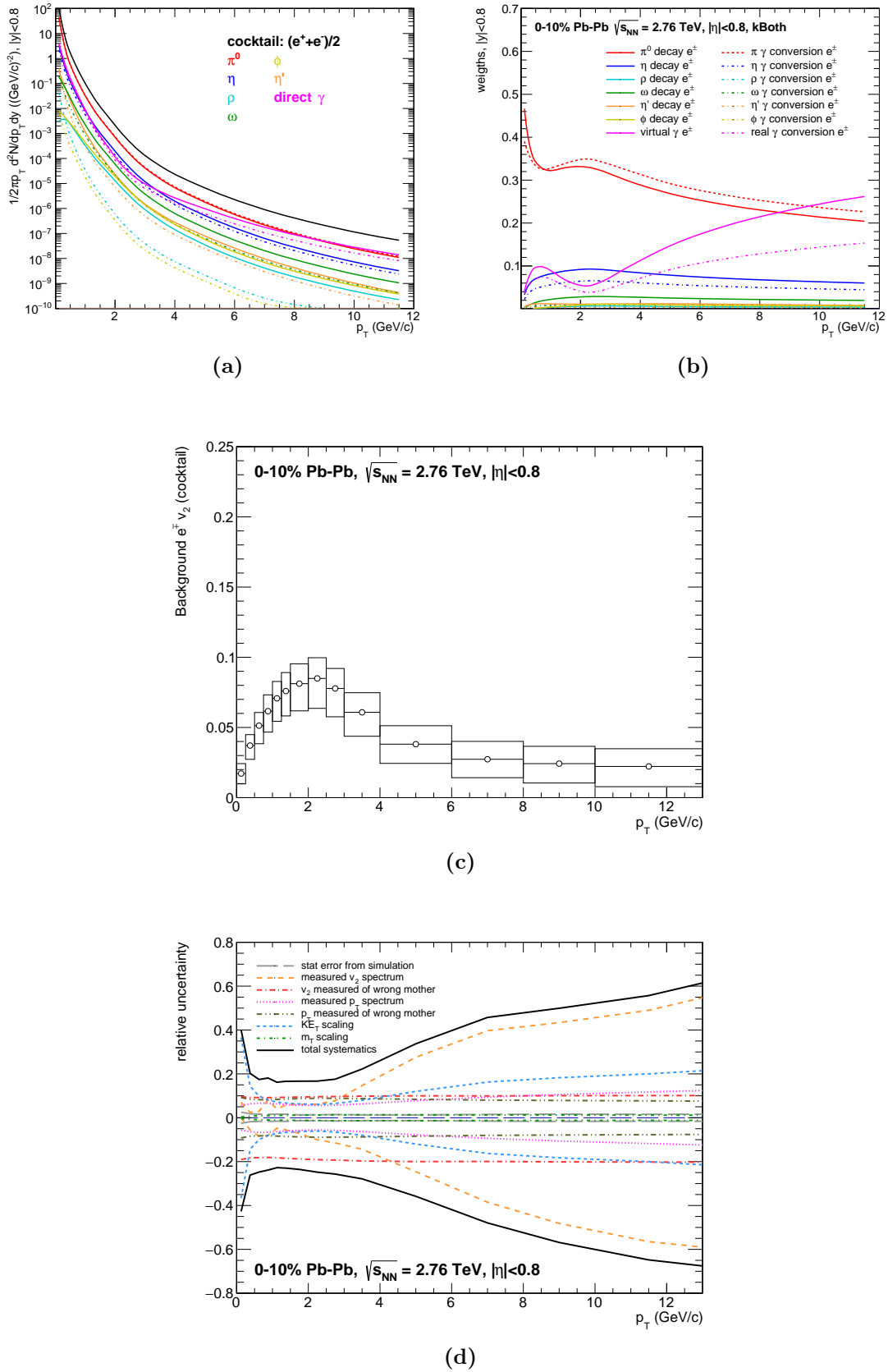
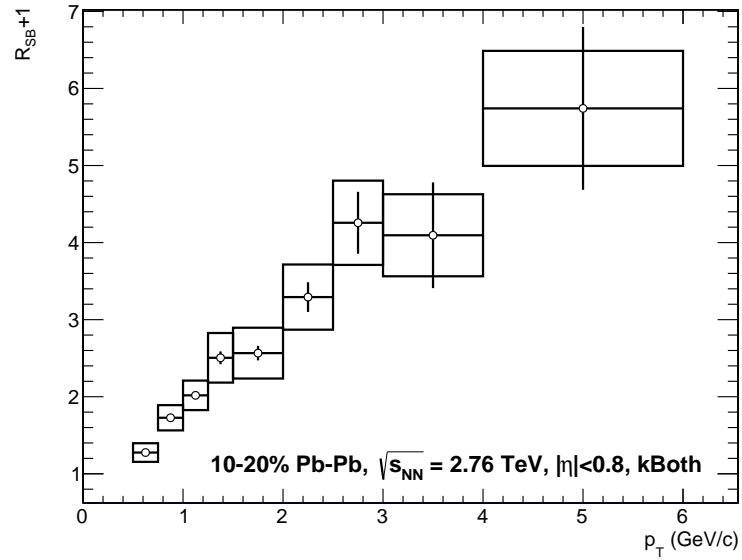
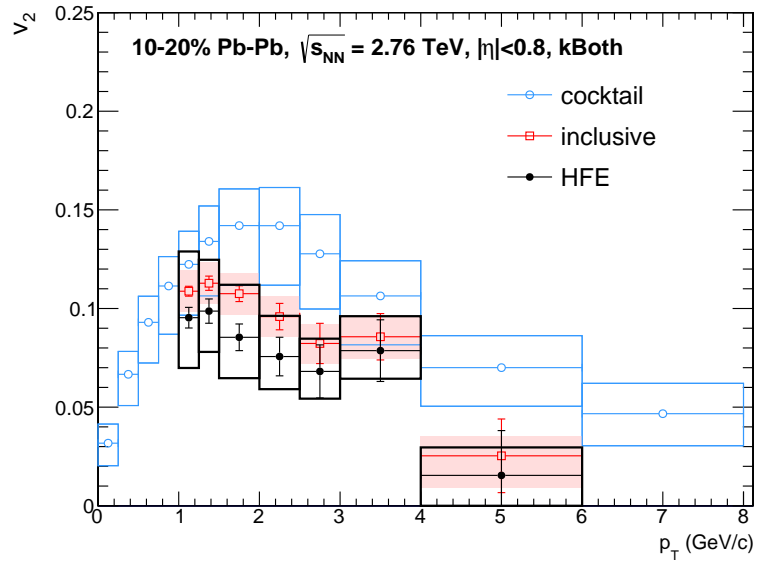


Figure 10.4: Absolute (a) and relative (b) p_T spectra of simulated electrons. The background electron elliptic flow (c) and the constituents of its systematic error (d).

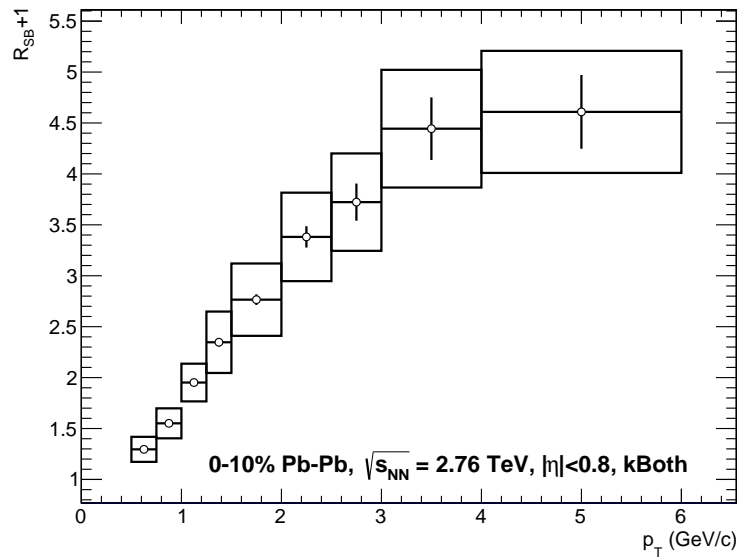


(a)

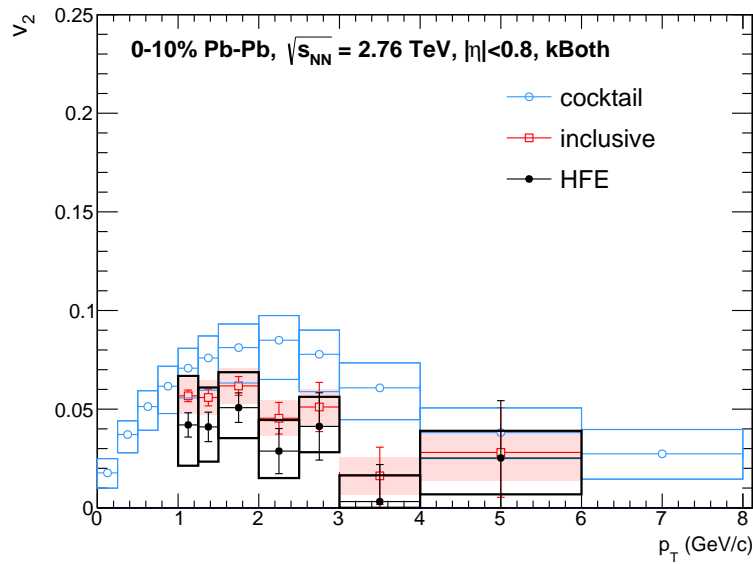


(b)

Figure 10.5: Signal-to-Background Ratio (a) and elliptic flow of heavy-flavour electrons compared with the inclusive measurement and the background cocktail (b)



(a)



(b)

Figure 10.6: Signal-to-Background Ratio (a) and elliptic flow of heavy-flavour electrons compared with the inclusive measurement and the background cocktail (b)

List of Figures

1.1	Asymptotic freedom of $\alpha_s(Q)$	8
1.2	Phase diagram of quarks and gluons	9
1.3	UrQMD Collision Picture	11
1.4	Glauber Collision Picture	11
3.1	Spatial distribution in the transverse plane	27
3.2	Comparison of Tsallis Exponentials	28
3.3	Comparison of pp and $Au + Au$ data to m_T -scaling	29
3.4	m_T -scaling of Tsallis spectra with flow	30
3.5	Thermal Model particle ratios at RHIC and LHC	31
3.6	Elliptic flow mass ordering	33
3.7	KE_T -scaling of identified-particle v_2	34
4.1	The CERN accelerator complex	38
4.2	The ALICE Experiment and its detectors	39
4.3	Layout of the ALICE TPC	41
4.4	Layout of the ALICE TRD and TOF	43
4.5	TRD working principle	44
4.6	Centrality estimation using V0 and ZDC	46
5.1	Definition of the angles used in the flow measurement	51
6.1	TPC signal of excluded runs	57
6.2	Centrality dependence of the number of events	58
6.3	Centrality and track number correlations	59
6.4	PID cuts for TOF and TPC	61
6.5	TRD working principle	63
6.6	Armenteros-Podolanski Plot	65
6.7	Electron sample contamination	67
6.8	Distribution of the event-plane angle	68
6.9	Event plane resolution	69
6.10	Inclusive electron elliptic flow	70
7.1	Virtual photon production	77
7.2	Charged and neutral pion p_T spectrum	80
7.3	The quality of m_T -scaling as compared to measured kaons	81
7.4	Direct-photon p_T spectrum	83
7.5	Elliptic flow of π^\pm	86
7.6	The quality of KE_T -scaling as compared to measured kaons	87
7.7	Direct-photon elliptic flow	88
7.8	Elliptic flow of π and Dalitz e^\pm extracted from the simulation	89
7.9	Pion Decay Feynman Diagrams	91
7.10	Comparison of “full” and “fast” conversion mechanisms	92
7.11	Elliptic flow calculations of virtual photons	93
7.12	Elliptic flow of the background cocktail	95
7.13	Systematic studies	97
8.1	Low-Mass dielectron spectrum	100
8.2	Signal-to-Background Ratio	101
8.3	Elliptic flow of heavy-flavour electrons	103

10.1	Inclusive electron elliptic flow (10-20%)	115
10.2	Inclusive electron elliptic flow (0-10%)	116
10.3	Elliptic flow of the background cocktail (10-20%)	117
10.4	Elliptic flow of the background cocktail (0-10%)	118
10.5	Elliptic flow of heavy-flavour electrons (10-20%)	119
10.6	Elliptic flow of heavy-flavour electrons (0-10%)	120

List of Tables

1.1	Eigenstates of fermions according to the Standard Model	5
1.2	The interactions and their gauge bosons	6
1.3	Unit system used in high energy physics	15
4.1	Main parameters of the LHC	38
4.2	Active area of the ITS layers	42
7.1	Dalitz decay branching ratios of π^0 , η and η'	78
7.2	Scaling factors used for the m_T -scaling	81

References

- [1] J. Bjorken et al. “Inelastic Electron Proton and gamma Proton Scattering, and the Structure of the Nucleon”. In: *Phys. Rev.* 185(5) (1969), pp. 1975–1982. DOI: 10.1103/PhysRev.185.1975 (cit. on p. 4).
- [2] E. D. Bloom et al. “High-Energy Inelastic e p Scattering at 6-Degrees and 10-Degrees”. In: *Phys. Rev. Lett.* 23(16) (1969), pp. 930–934. DOI: 10.1103/PhysRevLett.23.930 (cit. on p. 4).
- [3] M. Breitenbach et al. “Observed Behavior of Highly Inelastic electron-Proton Scattering”. In: *Phys. Rev. Lett.* 23(16) (1969), pp. 935–939. DOI: 10.1103/PhysRevLett.23.935 (cit. on p. 4).
- [4] M. Gell-Mann. “A Schematic Model of Baryons and Mesons”. In: *Phys. Lett.* 8(3) (1964), pp. 214–215. DOI: 10.1016/S0031-9163(64)92001-3 (cit. on p. 4).
- [5] G. Zweig. “An SU(3) model for strong interaction symmetry and its breaking. Version 2”. In: *CERN-TH-412* (1964) (cit. on p. 4).
- [6] V. E. Barnes et al. “Observation of a Hyperon with Strangeness Minus Three”. In: *Phys. Rev. Lett.* 12(8) (1964), pp. 204–206. DOI: 10.1103/PhysRevLett.12.204 (cit. on p. 4).
- [7] D. H. Perkins. *Introduction to High Energy Physics*. Cambridge University Press (cit. on pp. 4, 6).
- [8] K. Bethge. *Kernphysik: Eine Einführung*. Springer (cit. on pp. 4, 6).
- [9] W. Demtröder. *Experimentalphysik 3/4*. Springer (cit. on p. 4).
- [10] F. J. Dyson. “The Radiation Theories of Tomonaga, Schwinger, and Feynman”. In: *Phys. Rev.* 75(3) (1949), pp. 486–502. DOI: 10.1103/PhysRev.75.486 (cit. on p. 4).
- [11] H. Fritzsch, M. Gell-Mann and H. Leutwyler. “Advantages of the color octet gluon picture”. In: *Phys. Lett. B* 47(4) (1973), pp. 365–368. DOI: 10.1016/0370-2693(73)90625-4 (cit. on p. 4).
- [12] P. W. Higgs. “Broken Symmetries and the Masses of Gauge Bosons”. In: *Phys. Rev. Lett.* 13(16) (1973), pp. 508–509. DOI: 10.1103/PhysRevLett.13.508 (cit. on p. 4).
- [13] ATLAS Collaboration and CMS Collaboration. “Combined Measurement of the Higgs Boson Mass in pp Collisions at $\sqrt{s} = 7$ and 8 TeV with the ATLAS and CMS Experiments”. In: *Phys. Rev. Lett.* 114.191803 (2015). DOI: 10.1103/PhysRevLett.114.191803. arXiv: 1503.07589 (cit. on p. 4).
- [14] LHCb Collaboration. “Observation of $J/\psi p$ Resonances Consistent with Pentaquark States in $\Lambda_b^0 \rightarrow J/\psi K^- p$ Decays”. In: *Phys. Rev. Lett.* 115.072001 (2015). DOI: 10.1103/PhysRevLett.115.072001. arXiv: 1507.03414 (cit. on p. 4).

- [15] K.A. Olive et al. (Particle Data Group). “Review of Particle Physics”. In: *Chin. Phys. C* 38.090001 (2014). URL: pdg.lbl.gov (cit. on pp. 5, 8, 41, 77, 89).
- [16] D. J. Gross and F. Wilczek. “Ultraviolet Behavior of Non-Abelian Gauge Theories”. In: *Phys. Rev. Lett.* 30(26) (1973), pp. 1343–1346. DOI: 10.1103/PhysRevLett.30.1343 (cit. on p. 8).
- [17] H. D. Politzer. “Reliable Perturbative Results for Strong Interactions?” In: *Phys. Rev. Lett.* 30(26) (1973), pp. 1346–1349. DOI: 10.1103/PhysRevLett.30.1346 (cit. on p. 8).
- [18] A. Nakamura and S. Sakaib. “Viscosities of Hot Gluon – A Lattice QCD Study –”. In: *Nucl. Phys. A* 774 (2006), pp. 775–778. DOI: 10.1016/j.nuclphysa.2006.06.134. arXiv: hep-lat/0510039 (cit. on p. 8).
- [19] O. Philipsen. “Status of the QCD Phase Diagram from Lattice Calculations”. In: *Acta Phys. Polon. Supp.* 5(3) (2012), pp. 825–835. DOI: 10.5506/APhysPolBSupp.5.825. arXiv: 1111.5370 (cit. on p. 8).
- [20] F. Karsch. “Lattice QCD at High Temperature and Density”. In: *Lect. Notes Phys.* 583 (2002), pp. 209–249. DOI: 10.1007/3-540-45792-5_6. arXiv: hep-lat/0106019 (cit. on p. 8).
- [21] Z. Fodor and S. D. Katz. “Lattice QCD at finite T and μ and the critical point of QCD”. In: *Nucl. Phys. Proc. Suppl.* 106 (2002), pp. 441–443. DOI: 10.1016/S0920-5632(01)01740-6. arXiv: hep-lat/0110102 (cit. on p. 8).
- [22] N. Cabibbo and G. Parisi. “Exponential Hadronic Spectrum and Quark Liberation”. In: *Phys. Lett. B* 59(1) (1975), pp. 67–69. DOI: 10.1016/0370-2693(75)90158-6 (cit. on p. 9).
- [23] J. C. Collins and M. J. Perry. “Superdense Matter: Neutrons or Asymptotically Free Quarks?” In: *Phys. Rev. Lett.* 34(21) (1975), pp. 1353–1356. DOI: 10.1103/PhysRevLett.34.1353 (cit. on p. 9).
- [24] E. V. Shuryak. “Quark-Gluon Plasma and Hadronic Production of Leptons, Photons and Psions”. In: *Phys. Lett. B* 78(1) (1978), pp. 150–153. DOI: 10.1016/0370-2693(78)90370-2 (cit. on p. 9).
- [25] B. Povh et al. *Teilchen und Kerne: Eine Einführung in die physikalischen Konzepte*. Springer (cit. on p. 9).
- [26] B. Friman et al. “The CBM Physics Book: Compressed Baryonic Matter in Laboratory Experiments”. In: *Lect. Notes Phys.* 814 (2011), pp. 1–980. URL: <https://www-alt.gsi.de/documents/DOC-2009-Sep-120-2.pdf> (cit. on p. 9).
- [27] D. H. Rischke. “The Quark-Gluon Plasma in Equilibrium”. In: *Prog. Part. Nucl. Phys.* 52(1) (2004), pp. 197–296. DOI: 10.1016/j.ppnp.2003.09.002. arXiv: nucl-th/0305030 (cit. on p. 9).
- [28] M. Buballa. “NJL-model analysis of dense quark matter”. In: *Phys. Rep.* 407(4) (2005), pp. 205–376. DOI: 10.1016/j.physrep.2004.11.004. arXiv: hep-ph/0402234 (cit. on p. 9).

- [29] M. G. Alford et al. “Color superconductivity in dense quark matter”. In: *Rev. Mod. Phys.* 80(4) (2008), pp. 1455–1515. DOI: 10.1103/RevModPhys.80.1455. arXiv: 0709.4635 (cit. on p. 9).
- [30] Y. Aoki et al. “The QCD transition temperature: results with physical masses in the continuum limit”. In: *Phys. Lett. B* 643(1) (2006), pp. 46–54. DOI: 10.1016/j.physletb.2006.10.021. arXiv: hep-lat/0609068 (cit. on p. 9).
- [31] A. Bazavov et al. “Equation of state and QCD transition at finite temperature”. In: *Phys. Rev. D* 80.014504 (2009). DOI: 10.1103/PhysRevD.80.014504. arXiv: 0903.4379 (cit. on p. 9).
- [32] M. Cheng et al. “The Transition temperature in QCD”. In: *Phys. Rev. D* 74.054507 (2006). DOI: 10.1103/PhysRevD.74.054507. arXiv: hep-lat/0608013 (cit. on p. 9).
- [33] F. Weber. “Strange Quark Matter and Compact Stars”. In: *Prog. Part. Nucl. Phys.* 54(1) (2005), pp. 193–288. DOI: 10.1016/j.ppnp.2004.07.001. arXiv: astro-ph/0407155 (cit. on p. 10).
- [34] N.A. Gentile et al. “The QCD phase transition and supernova core collapse”. In: *Astrophys. J.* 414 (1993), pp. 701–711. DOI: 10.1086/173116 (cit. on p. 10).
- [35] I. Sagert et al. “Signals of the QCD phase transition in core-collapse supernovae”. In: *Phys. Rev. Lett.* 102.081101 (2009). DOI: 10.1103/PhysRevLett.102.081101. arXiv: 0809.4225 (cit. on p. 10).
- [36] CMS Collaboration. “Measurement of the elliptic anisotropy of charged particles produced in PbPb collisions at $\sqrt{s_{NN}} = 2.76$ TeV”. In: *Phys. Rev. C* 87.014902 (2013). DOI: 10.1103/PhysRevC.87.014902. arXiv: 1204.1409 (cit. on pp. 11, 49).
- [37] M. L. Miller et al. “Glauber Modeling in High Energy Nuclear Collisions”. In: *Ann. Rev. Nucl. Part. Sci.* 57 (2007), pp. 205–243. DOI: 10.1146/annurev.nucl.57.090506.123020 (cit. on pp. 11, 49).
- [38] A. D. Martin et al. “Parton distributions for the LHC”. In: *Eur. Phys. J. C* 63(2) (2009), pp. 189–285. DOI: 10.1140/epjc/s10052-009-1072-5. arXiv: 0901.0002 (cit. on p. 12).
- [39] NNPDF Collaboration. “Parton distributions for the LHC Run II”. In: *JHEP* 0904.040 (2015). DOI: 10.1007/JHEP04(2015)040. arXiv: 1410.8849 (cit. on p. 12).
- [40] Hung-Liang Lai et al. “New parton distributions for collider physics”. In: *Phys. Rev. D* 82.074024 (2010). DOI: 10.1103/PhysRevD.82.074024. arXiv: 1007.2241 (cit. on p. 12).
- [41] K. J. Eskola, H. Paukkunen and C. A. Salgado. “EPS09 — A new generation of NLO and LO nuclear parton distribution functions”. In: *JHEP* 0904.065 (2009). DOI: 10.1088/1126-6708/2009/04/065. arXiv: 0902.4154 (cit. on p. 12).

- [42] K. Kovarik et al. “Nuclear Corrections in Neutrino-Nucleus Deep Inelastic Scattering and their Compatibility with Global Nuclear Parton-Distribution-Function Analyses”. In: *Phys. Rev. Lett.* 106.122301 (2011). DOI: 10.1103/PhysRevLett.106.122301. arXiv: 1012.0286 (cit. on p. 12).
- [43] D. de Florian et al. “Global analysis of nuclear parton distributions”. In: *Phys. Rev. D* 85.074028 (2012). DOI: 10.1103/PhysRevD.85.074028. arXiv: 1112.6324 (cit. on p. 12).
- [44] STAR Collaboration. “Distributions of Charged Hadrons Associated with High Transverse Momentum Particles in pp and $Au+Au$ Collisions at $\sqrt{s_{NN}} = 200$ GeV”. In: *Phys. Rev. Lett.* 95.152301 (2005). DOI: 10.1103/PhysRevLett.95.152301. arXiv: nucl-ex/0501016 (cit. on p. 13).
- [45] PHENIX Collaboration. “Dense-Medium Modifications to Jet-Induced Hadron Pair Distributions in $Au + Au$ Collisions at $\sqrt{s_{NN}} = 200$ GeV”. In: *Phys. Rev. Lett.* 97.052301 (2006). DOI: 10.1103/PhysRevLett.97.052301 (cit. on p. 13).
- [46] P. Koch, B. Müller and J. Rafelski. “Strangeness in Relativistic Heavy Ion Collisions”. In: *Phys. Rept.* 142(4) (1986), pp. 167–262. DOI: 10.1016/0370-1573(86)90096-7 (cit. on p. 14).
- [47] T. Matsui and H. Satz. “ J/Ψ suppression by quark-gluon plasma formation”. In: *Phys. Lett. B* 178(4) (1986), pp. 416–422. DOI: 10.1016/0370-2693(86)91404-8 (cit. on p. 14).
- [48] P. Braun-Munzinger and J. Stachel. “(Non)thermal aspects of charmonium production and a new look at J/Ψ suppression”. In: *Phys. Lett. B* 490(3) (2000), pp. 196–202. DOI: 10.1016/S0370-2693(00)00991-6. arXiv: nucl-th/0007059 (cit. on pp. 14, 31).
- [49] P. Braun-Munzinger and J. Stachel. “On Charm Production near the Phase Boundary”. In: *Nucl. Phys. A* 690(1) (2001), pp. 119–126. DOI: 10.1016/S0375-9474(01)00936-8. arXiv: nucl-th/0012064 (cit. on pp. 14, 31).
- [50] R. L. Thews, M. Schroedter and J. Rafelski. “Enhanced J/Ψ production in deconfined quark matter”. In: *Phys. Rev. C* 63.054905 (2001). DOI: 10.1103/PhysRevC.63.054905. arXiv: hep-ph/0007323 (cit. on p. 14).
- [51] “Resolution 1 of the 24th CGPM”. In: *Comptes Rendus de la 24e CGPM* (2011), pp. 532–536. URL: <http://www.bipm.org/utis/common/pdf/CGPM/CGPM24.pdf> (cit. on p. 14).
- [52] “Resolution 1 of the 25th CGPM”. In: *Comptes Rendus de la 25e CGPM* (2014), pp. 416–417. URL: <http://www.bipm.org/utis/common/pdf/CGPM/CGPM25.pdf> (cit. on p. 14).
- [53] *The International System of Units (SI)*. Bureau International des Poids et Mesures. 2008. URL: http://www.bipm.org/utis/common/pdf/si_brochure_8.pdf (cit. on p. 14).
- [54] A. Einstein. “Zur Elektrodynamik bewegter Körper”. In: *Ann. Phys.* 322 (1905), pp. 891–921. DOI: 10.1002/andp.19053221004 (cit. on p. 17).

- [55] A. Einstein. “Ist die Trägheit eines Körpers von seinem Energieinhalt abhängig?” In: *Ann. Phys.* 323 (1905), pp. 639–641. DOI: 10.1002/andp.200590007 (cit. on p. 17).
- [56] A. Einstein. “Das Prinzip von der Erhaltung der Schwerpunktsbewegung und die Trägheit der Energie”. In: *Ann. Phys.* 325 (1906), pp. 627–633. DOI: 10.1002/andp.200590011 (cit. on p. 17).
- [57] A. Einstein. “Über die vom Relativitätsprinzip geforderte Trägheit der Energie”. In: *Ann. Phys.* 328 (1907), pp. 371–384. DOI: 10.1002/andp.200590018 (cit. on p. 17).
- [58] A. Einstein. *Über die spezielle und die allgemeine Relativitätstheorie*. Springer, 1916. ISBN: 978-3-540-87776-9. DOI: 10.1007/978-3-540-87777-6 (cit. on p. 17).
- [59] Jean-Yves Ollitrault. “Relativistic hydrodynamics for heavy-ion collisions”. In: *Eur. J. Phys.* 29(2) (2008), pp. 275–302. DOI: 10.1088/0143-0807/29/2/010. arXiv: 0708.2433 (cit. on p. 23).
- [60] A. K. Chaudhuri. “Knudsen number, ideal hydrodynamic limit for elliptic flow, and QGP viscosity in $\sqrt{s_{NN}} = 62$ and 200 GeV $Cu + Cu/Au + Au$ collisions”. In: *Phys. Rev. C* 82.047901 (2010). DOI: 10.1103/PhysRevC.82.047901. arXiv: 1006.4478 (cit. on p. 23).
- [61] Derek A. Teaney. *Viscous Hydrodynamics and the Quark Gluon Plasma*. 2009. arXiv: 0905.2433 (cit. on p. 23).
- [62] B. H. Alver et al. “Triangular flow in hydrodynamics and transport theory”. In: *Phys. Rev. C* 82.034913 (2010). DOI: 10.1103/PhysRevC.82.034913. arXiv: 1007.5469 (cit. on p. 23).
- [63] P. Huovinen and P.V. Ruuskanen. “Hydrodynamic Models for Heavy Ion Collisions”. In: *Ann. Rev. Nucl. Part. Sci.* 56 (2006), pp. 163–206. DOI: 10.1146/annurev.nucl.54.070103.181236. arXiv: nucl-th/0605008 (cit. on p. 23).
- [64] H. Niemi and G. S. Denicol. *How large is the Knudsen number reached in fluid dynamical simulations of ultrarelativistic heavy ion collisions?* 2014. arXiv: 1404.7327 (cit. on p. 23).
- [65] E. T. Jaynes. “Information Theory and Statistical Mechanics”. In: *Phys. Rev.* 106(4) (1957), pp. 620–630. DOI: 10.1103/PhysRev.106.620 (cit. on p. 27).
- [66] C. Tsallis. “Possible generalization of Boltzmann-Gibbs statistics”. In: *J. Stat. Phys.* 52(1) (1988), pp. 479–487. DOI: 10.1007/BF01016429 (cit. on p. 27).
- [67] C. Tsallis. “What are the Numbers that Experiments Provide?” In: *Quim. Nova* 17(6) (1994), pp. 468–471 (cit. on p. 27).
- [68] S. Chatterjee et al. “Freeze-Out Parameters in Heavy-Ion Collisions at AGS, SPS, RHIC, and LHC Energies”. In: *Adv.High Energy Phys.* 2015.349013 (2015). DOI: 10.1155/2015/349013 (cit. on pp. 28, 30, 32).
- [69] P. Sett and P. Shukla. *Inferring freeze-out parameters from pion measurements at RHIC and LHC*. 2015. arXiv: 1505.05258 (cit. on pp. 28, 30, 32).

- [70] J. Cleymans and D. Worku. “Relativistic Thermodynamics: Transverse Momentum Distributions in High-Energy Physics”. In: *Eur. Phys. J. A* 48.160 (2012). DOI: 10.1140/epja/i2012-12160-0. arXiv: 1203.4343 (cit. on p. 28).
- [71] F. Cooper and G. Frye. “Single-particle distribution in the hydrodynamic and statistical thermodynamic models of multiparticle production”. In: *Phys. Rev. D* 10(1) (1974), pp. 186–189. DOI: 10.1103/PhysRevD.10.186 (cit. on p. 29).
- [72] Cheuk-Yin Wong and Grzegorz Wilk. “Tsallis Fits to p_T Spectra for pp Collisions at LHC”. In: *Acta Phys. Polon. B* 43(11) (2012), pp. 2047–2054. DOI: 10.5506/APhysPolB.43.2047. arXiv: 1210.3661 (cit. on p. 29).
- [73] M. D. Azmi and J. Cleymans. *Transverse Momentum Distributions in p-Pb collisions and Tsallis Thermodynamics*. 2013. arXiv: 1311.2909 (cit. on p. 29).
- [74] M.D. Azmi and J. Cleymans. “Transverse Momentum Distributions in proton - proton Collisions at LHC Energies and Tsallis Thermodynamics”. In: *J. Phys. G* 41.065001 (2014). DOI: 10.1088/0954-3899/41/6/065001. arXiv: 1401.4835 (cit. on p. 29).
- [75] PHENIX Collaboration. “Detailed measurement of the e^+e^- pair continuum in $p + p$ and $Au + Au$ collisions at $\sqrt{s_{NN}} = 200$ GeV and implications for direct photon production”. In: *Phys. Rev. C* 81.034911 (2010). DOI: 10.1103/PhysRevC.81.034911. arXiv: 0912.0244 (cit. on p. 29).
- [76] R. Hagedorn. “Multiplicities, p_T Distributions and the Expected Hadron \rightarrow Quark - Gluon Phase Transition”. In: *Riv. Nuovo Cim.* 6(10) (1983), pp. 1–50. DOI: 10.1007/BF02740917 (cit. on pp. 29, 79).
- [77] ALICE Collaboration. “Results on identified particle production in pp, p-Pb and Pb-Pb collisions measured with ALICE at the LHC”. In: *EPJ Web Conf.* 71.00101 (2014). DOI: 10.1051/epjconf/20147100101. arXiv: 1402.0835 (cit. on pp. 30, 32, 33).
- [78] ALICE Collaboration. “Centrality dependence of π , K, and p production in Pb-Pb collisions at $\sqrt{s_{NN}} = 2.76$ TeV”. In: *Phys. Rev. C* 88(4) (2013). DOI: 10.1103/PhysRevC.88.044910. arXiv: 1303.0737 (cit. on pp. 30, 79).
- [79] P. Braun-Munzinger, K. Redlich and J. Stachel. *Particle Production in Heavy Ion Collisions*. 2003. arXiv: nucl-th/0304013 (cit. on p. 31).
- [80] A. Andronic et al. “The statistical model in Pb-Pb collisions at the LHC”. In: *Nucl. Phys. A* 904-905 (2013), pp. 535c–538c. DOI: 10.1016/j.nuclphysa.2013.02.070. arXiv: 1210.7724 (cit. on pp. 31, 32).
- [81] G. Policastro, D. T.Son and A. O.Starinets. “From AdS/CFT correspondence to hydrodynamics”. In: *JHEP* 0209.043 (2002). DOI: 10.1088/1126-6708/2002/09/043. arXiv: hep-th/0205052 (cit. on p. 34).

- [82] P. Kovtun, D. T. Son and A. O. Starinets. “Viscosity in Strongly Interacting Quantum Field Theories from Black Hole Physics”. In: *Phys. Rev. Lett.* 94.111601 (2005). DOI: 10.1103/PhysRevLett.94.111601. arXiv: hep-th/0405231 (cit. on p. 34).
- [83] B. Schenke, S. Jeon and C. Gale. “Elliptic and Triangular Flow in Event-by-Event $D = 3 + 1$ Viscous Hydrodynamics”. In: *Phys. Rev. Lett.* 106.042301 (2011). DOI: 10.1103/PhysRevLett.106.042301. arXiv: 1009.3244 (cit. on p. 34).
- [84] PHENIX Collaboration. “Azimuthal Anisotropy of π^0 Production in $Au + Au$ Collisions at $\sqrt{s_{NN}} = 200$ GeV: Path-Length Dependence of Jet Quenching and the Role of Initial Geometry”. In: *Phys. Rev. Lett.* 105.142301 (2010). DOI: 10.1103/PhysRevLett.105.142301. arXiv: 1006.3740 (cit. on p. 34).
- [85] B. Betz, M. Gyulassy and G. Torrieri. “Sensitivity of Azimuthal Jet Tomography to Early Time Energy-Loss at RHIC and LHC”. In: *J. Phys. G* 38.124153 (2011). DOI: 10.1088/0954-3899/38/12/124153. arXiv: 1106.4564 (cit. on p. 34).
- [86] J. Jia and R. Wei. “Dissecting the role of initial collision geometry for jet quenching observables in relativistic heavy ion collisions”. In: *Phys. Rev. C* 82.024902 (2010). DOI: 10.1103/PhysRevC.82.024902. arXiv: 1005.0645 (cit. on p. 34).
- [87] PHENIX Collaboration. “Scaling Properties of Azimuthal Anisotropy in $Au + Au$ and $Cu + Cu$ Collisions at $\sqrt{s_{NN}} = 200$ GeV”. In: *Phys. Rev. Lett.* 98.162301 (2007). DOI: 10.1103/PhysRevLett.98.162301. arXiv: nucl-ex/0608033 (cit. on p. 34).
- [88] J. Jia and C. Zhang. “Quark number scaling of v_2 in transverse kinetic energy and its implications for coalescence models”. In: *Phys. Rev. C* 75.031901(R) (2007). DOI: 10.1103/PhysRevC.75.031901. arXiv: hep-ph/0608187 (cit. on p. 34).
- [89] ALICE Collaboration. “Anisotropic flow of identified particles in Pb-Pb collisions at $\sqrt{s_{NN}} = 2.76$ TeV measured with ALICE at the LHC”. In: *Nucl. Phys. A* 904-905 (2013), pp. 483c–486c. DOI: 10.1016/j.nuclphysa.2013.02.058. arXiv: 1212.1292 (cit. on pp. 34, 85).
- [90] A. M. Poskanzer and S. A. Voloshin. “Methods for analyzing anisotropic flow in relativistic nuclear collisions”. In: *Phys. Rev. C* 58(3) (1998), pp. 1671–1678. DOI: 10.1103/PhysRevC.58.1671. arXiv: nucl-ex/9805001 (cit. on pp. 35, 50, 55).
- [91] PHENIX Collaboration. “Elliptic Flow of Identified Hadrons in $Au + Au$ Collisions at $\sqrt{s_{NN}} = 200$ GeV”. In: *Phys. Rev. Lett.* 91.182301 (2003). DOI: 10.1103/PhysRevLett.91.182301. arXiv: nucl-ex/0305013 (cit. on p. 35).
- [92] STAR Collaboration. “Energy and system size dependence of elliptic flow: using rapidity gaps to suppress non-flow contribution”. In: *AIP Conf. Proc.* 870 (2006), pp. 691–694. DOI: 10.1063/1.2402731. arXiv: nucl-ex/0610038 (cit. on p. 35).

- [93] *LHC Design Report*. CERN-2004-003-V-1. CERN. 2004. DOI: 10.5170/CERN-2004-003-V-1. URL: <http://cds.cern.ch/record/782076> (cit. on pp. 37, 38, 58).
- [94] L. Evans and P. Bryant. “LHC Machine”. In: *JINST* 3.S08001 (2008). DOI: 10.1088/1748-0221/3/08/S08001. URL: <http://cds.cern.ch/record/1129806> (cit. on p. 37).
- [95] *CERN-Brochure-2009-003*. CERN. URL: <http://cds.cern.ch/record/1165534> (cit. on p. 38).
- [96] *Definition of the ALICE Coordinate System and Basic Rules for Sub-detector Components Numbering*. ALICE-INT-2003-038. CERN. 2003. URL: https://www.cern.ch/Alice-Servotech/HELP_DCDB-SVT/Help_Files/ALICE-INT-2003-038.pdf (cit. on p. 40).
- [97] ALICE Collaboration. “The ALICE experiment at the CERN LHC”. In: *JINST* 3.S08002 (2008) (cit. on p. 40).
- [98] ALICE Collaboration. *ALICE: Technical Design Report of the Time Projection Chamber*. CERN-OPEN-2000-183; ALICE-TDR-7; CERN-LHCC-2000-001. CERN. 2000. URL: <http://cds.cern.ch/record/451098> (cit. on p. 41).
- [99] J. Alme, Y. Andres, H. Appelshauser et al. “The ALICE TPC, a large 3-dimensional tracking device with fast readout for ultra-high multiplicity events”. In: *Nucl. Instrum. Meth. A* 622(1) (2010), pp. 316–367. DOI: 10.1016/j.nima.2010.04.042. arXiv: 1001.1950 (cit. on p. 41).
- [100] ALICE Collaboration. “Particle Identification in the ALICE Experiment”. In: *J. Phys. G* 38.124073 (2011). DOI: 10.1088/0954-3899/38/12/124073. arXiv: 1107.1514 (cit. on pp. 41, 45).
- [101] F. Sauli. *Principles of Operation of Multiwire Proportional and Drift Chambers*. CERN-77-09. CERN. 1977. DOI: 10.5170/CERN-1977-009. URL: <http://cds.cern.ch/record/117989> (cit. on p. 41).
- [102] ALICE Collaboration. *ALICE: Technical Design Report of the Inner Tracking System (ITS)*. ALICE-TDR-4; CERN-LHCC-99-012. CERN. 1999. URL: <http://cds.cern.ch/record/391175> (cit. on p. 42).
- [103] ALICE Collaboration. “Technical Design Report for the Upgrade of the ALICE Inner Tracking System”. In: *J. Phys. G* 41.087002 (2014). DOI: 10.1088/0954-3899/41/8/087002. URL: <http://cds.cern.ch/record/1625842> (cit. on pp. 42, 104).
- [104] V. L. Ginzburg and I. M. Frank. “Radiation of a uniformly moving electron due to its transition from one medium into another”. In: *Zh. Eksp. Teor. Fiz.* 16 (1946), pp. 15–28 (cit. on p. 43).
- [105] P. Goldsmith and J. V. Jelley. “Optical Transition Radiation from Protons Entering Metal Surfaces”. In: *Phil. Mag.* 4 (1959), pp. 836–844 (cit. on p. 43).

- [106] ALICE TRD collaboration. “Transition Radiation Spectroscopy with Prototypes of the ALICE TRD”. In: *Nucl. Instrum. Meth. A* 522 (2004), pp. 45–49. DOI: 10.1016/j.nima.2004.01.016. arXiv: physics/0404106 (cit. on p. 44).
- [107] ALICE Collaboration. *ALICE: Technical Design Report of the Transition Radiation Detector*. ALICE-TDR-9; CERN-LHCC-2001-021; LYCEN-2001-97. CERN. 2001. URL: <http://cds.cern.ch/record/519145> (cit. on p. 44).
- [108] ALICE Collaboration. *ALICE: Technical Design Report of the Time-of-Flight System (TOF)*. ALICE-TDR-8; CERN-LHCC-2000-012. CERN. 2000. URL: <http://cds.cern.ch/record/430132> (cit. on p. 44).
- [109] ALICE Collaboration. *ALICE: Addendum to the Technical Design Report of the Time of Flight System (TOF)*. ALICE-TDR-8-add-1; CERN-LHCC-2002-016. CERN. 2002. URL: <http://cds.cern.ch/record/545834> (cit. on p. 44).
- [110] ALICE Collaboration. *ALICE: Electromagnetic Calorimeter Technical Design Report*. CERN-LHCC-2008-014; ALICE-TDR-14. CERN. 2008. URL: <http://cds.cern.ch/record/1121574> (cit. on p. 45).
- [111] ALICE Collaboration. *ALICE: Technical Design Report on Forward Detectors: FMD, T0 and V0*. ALICE-TDR-11; CERN-LHCC-2004-025. CERN. 2004. URL: <http://cds.cern.ch/record/781854> (cit. on p. 46, 47).
- [112] ALICE Collaboration. “Centrality determination of Pb-Pb collisions at $\sqrt{s_{NN}} = 2.76$ TeV with ALICE”. In: *Phys. Rev. C* 88.044909 (2013). DOI: 10.1103/PhysRevC.88.044909. arXiv: 1301.4361 (cit. on p. 46).
- [113] ALICE Collaboration. *ALICE: Technical Design Report of the Zero Degree Calorimeter (ZDC)*. ALICE-TDR-3; CERN-LHCC-99-005. CERN. 1999. URL: <http://cds.cern.ch/record/381433> (cit. on p. 46).
- [114] J. Uphoff et al. “Heavy quark production at RHIC and LHC within a partonic transport model”. In: *Phys. Rev. C* 82.044906 (2010). DOI: 10.1103/PhysRevC.82.044906. arXiv: 1003.4200 (cit. on p. 49).
- [115] A. Majumder and M. Van Leeuwen. “The theory and phenomenology of perturbative QCD based jet quenching”. In: *Prog. Part. Nucl. Phys.* 66(1) (2011), pp. 41–92. DOI: 10.1016/j.pnnp.2010.09.001. arXiv: 1002.2206 (cit. on p. 49).
- [116] Miklos Gyulassy and Michael Plumer. “Jet Quenching in Dense Matter”. In: *Phys. Lett. B* 243(4) (1990), pp. 432–438. DOI: 10.1016/0370-2693(90)91409-5 (cit. on p. 49).
- [117] R. Baier et al. “Radiative energy loss and p_{\perp} -broadening of high energy partons in nuclei”. In: *Nucl. Phys. B* 484 (1997), pp. 265–282. DOI: 10.1016/S0550-3213(96)00581-0. arXiv: hep-ph/9608322 (cit. on p. 49).
- [118] M. H. Thoma and M. Gyulassy. “Quark damping and energy loss in the high temperature QCD”. In: *Nucl. Phys. B* 351(3) (1991), pp. 491–506. DOI: 10.1016/S0550-3213(05)80031-8 (cit. on p. 49).

- [119] E. Braaten and M. H. Thoma. “Energy loss of a heavy quark in the quark-gluon plasma”. In: *Phys. Rev. D* 44(9) (1991), R2625–R2630. DOI: 10.1103/PhysRevD.44.R2625 (cit. on p. 49).
- [120] R. J. Glauber and G. Matthiae. “High-energy scattering of protons by nuclei”. In: *Nucl. Phys. B* 21(2) (1970), pp. 135–157. DOI: 10.1016/0550-3213(70)90511-0 (cit. on p. 49).
- [121] STAR Collaboration. “Transverse Momentum and Centrality Dependence of High- p_T Nonphotonic Electron Suppression in $Au + Au$ Collisions at $\sqrt{s_{NN}} = 200$ GeV”. In: *Phys. Rev. Lett.* 98.192301 (2007). DOI: 10.1103/PhysRevLett.98.192301. arXiv: nucl-ex/0607012 (cit. on p. 49).
- [122] STAR Collaboration. “Observation of D^0 Meson Nuclear Modifications in $Au + Au$ Collisions at $\sqrt{s_{NN}} = 200$ GeV”. In: *Phys. Rev. Lett.* 113.142301 (2014). DOI: 10.1103/PhysRevLett.113.142301. arXiv: 1404.6185 (cit. on p. 49).
- [123] PHENIX Collaboration. “Nuclear Modification of Electron Spectra and Implications for Heavy Quark Energy Loss in $Au + Au$ Collisions at $\sqrt{s_{NN}} = 200$ GeV”. In: *Phys. Rev. Lett.* 96.032301 (2006). DOI: 10.1103/PhysRevLett.96.032301. arXiv: nucl-ex/0510047 (cit. on p. 49).
- [124] PHENIX Collaboration. “Heavy-quark production in $p + p$ and energy loss and flow of heavy quarks in $Au + Au$ collisions at $\sqrt{s_{NN}} = 200$ GeV”. In: *Phys. Rev. C* 84.044905 (2011). DOI: 10.1103/PhysRevC.84.044905. arXiv: 1005.1627 (cit. on pp. 49, 50, 84, 102).
- [125] PHENIX Collaboration. “Nuclear-modification factor for open-heavy-flavor production at forward rapidity in $Cu + Cu$ collisions at $\sqrt{s_{NN}} = 200$ GeV”. In: *Phys. Rev. C* 86.024909 (2012). DOI: 10.1103/PhysRevC.86.024909. arXiv: 1204.0754 (cit. on p. 49).
- [126] ALICE Collaboration. “Suppression of high transverse momentum D mesons in central Pb-Pb collisions at $\sqrt{s_{NN}} = 2.76$ TeV”. In: *JHEP* 1209.112 (2012). DOI: 10.1007/JHEP09(2012)112. arXiv: 1203.2160 (cit. on pp. 49, 102, 104).
- [127] ALICE Collaboration. “Production of Muons from Heavy Flavor Decays at Forward Rapidity in pp and Pb-Pb Collisions at $\sqrt{s_{NN}} = 2.76$ TeV”. In: *Phys. Rev. Lett.* 109.112301 (2012). DOI: 10.1103/PhysRevLett.109.112301. arXiv: 1205.6443 (cit. on pp. 49, 102, 104).
- [128] ALICE Collaboration. “Centrality dependence of high- p_T D meson suppression in Pb-Pb collisions at $\sqrt{s_{NN}} = 2.76$ TeV”. In: *JHEP* 1511.205 (2015). DOI: 10.1007/JHEP11(2015)205. arXiv: 1506.06604 (cit. on pp. 49, 102, 104).
- [129] CMS Collaboration. “Suppression of non-prompt J/ψ , prompt J/ψ , and $\Upsilon(1S)$ in PbPb collisions at $\sqrt{s_{NN}} = 2.76$ TeV”. In: *JHEP* 1205.063 (2012). DOI: 10.1007/JHEP05(2012)063. arXiv: 1201.5069 (cit. on pp. 49, 102, 104).

- [130] M. Gyulassy, I. Vitev et al. “High p_T Azimuthal Asymmetry in Noncentral $A + A$ at RHIC”. In: *Phys. Rev. Lett.* 86(12) (2001), pp. 2537–2540. DOI: 10.1103/PhysRevLett.86.2537. arXiv: nucl-th/0012092 (cit. on p. 49).
- [131] E. V. Shuryak. “Azimuthal asymmetry at large p_t seem to be too large for a pure “jet quenching””. In: *Phys. Rev. C* 66.027902 (2002). DOI: 10.1103/PhysRevC.66.027902. arXiv: nucl-th/0112042 (cit. on p. 49).
- [132] STAR Collaboration. “Azimuthal anisotropy in $Au+Au$ collisions at $\sqrt{s_{NN}} = 200$ GeV”. In: *Phys. Rev. C* 72.014904 (2005). DOI: 10.1103/PhysRevC.72.014904. arXiv: nucl-ex/0409033 (cit. on p. 49).
- [133] PHENIX Collaboration. “High- p_T π^0 production with respect to the reaction plane in $Au + Au$ collisions at $\sqrt{s_{NN}} = 200$ GeV”. In: *Phys. Rev. C* 80.054907 (2009). DOI: 10.1103/PhysRevC.80.054907. arXiv: 0903.4886 (cit. on p. 49).
- [134] ALICE Collaboration. “Elliptic Flow of Charged Particles in Pb-Pb Collisions at $\sqrt{s_{NN}} = 2.76$ TeV”. In: *Phys. Rev. Lett.* 105.252302 (2010). DOI: 10.1103/PhysRevLett.105.252302. arXiv: 1011.3914 (cit. on p. 49).
- [135] ALICE Collaboration. “Elliptic flow of identified hadrons in Pb-Pb collisions at $\sqrt{s_{NN}} = 2.76$ TeV”. In: *JHEP* 1506.190 (2015). DOI: 10.1007/JHEP06(2015)190. arXiv: 1405.4632 (cit. on pp. 49, 85).
- [136] ATLAS Collaboration. “Measurement of the azimuthal anisotropy for charged particle production in $\sqrt{s_{NN}} = 2.76$ TeV lead-lead collisions with the ATLAS detector”. In: *Phys. Rev. C* 86.014907 (2012). DOI: 10.1103/PhysRevC.86.014907. arXiv: 1203.3087 (cit. on p. 49).
- [137] Jean-Yves Ollitrault. “Anisotropy as a signature of transverse collective flow”. In: *Phys. Rev. D* 46(1) (1992), pp. 229–245. DOI: 10.1103/PhysRevD.46.229 (cit. on p. 49).
- [138] D. Teaney, J. Lauret and E. V. Shuryak. “Flow at the SPS and RHIC as a Quark-Gluon Plasma Signature”. In: *Phys. Rev. Lett.* 86(21) (2001), pp. 4783–4786. DOI: 10.1103/PhysRevLett.86.4783 (cit. on p. 49).
- [139] P. F. Kolb and U. W. Heinz. *Hydrodynamic description of ultrarelativistic heavy ion collisions*. 2003. arXiv: nucl-th/0305084 (cit. on p. 49).
- [140] STAR Collaboration. *Elliptic flow of non-photonic electrons in Au+Au collisions at $\sqrt{s_{NN}} = 200, 62.4$ and 39 GeV*. 2014. arXiv: 1405.6348 (cit. on pp. 49, 102).
- [141] ALICE Collaboration. “ D Meson Elliptic Flow in Noncentral Pb-Pb Collisions at $\sqrt{s_{NN}} = 2.76$ TeV”. In: *Phys. Rev. Lett.* 111.102301 (2013). DOI: 10.1103/PhysRevLett.111.102301. arXiv: 1305.2707 (cit. on pp. 50, 102, 104).
- [142] ALICE Collaboration. “Azimuthal anisotropy of D meson production in Pb-Pb collisions at $\sqrt{s_{NN}} = 2.76$ TeV”. In: *Phys. Rev. C* 90.034904 (2014). DOI: 10.1103/PhysRevC.90.034904. arXiv: 1405.2001 (cit. on pp. 50, 102, 104).

- [143] ALICE Collaboration. “Elliptic flow of muons from heavy-flavour hadron decays at forward rapidity in Pb-Pb collisions at $\sqrt{s_{NN}} = 2.76$ TeV”. In: *Phys. Lett. B* 753 (2016), pp. 41–56. DOI: 10.1016/j.physletb.2015.11.059. arXiv: 1507.03134 (cit. on pp. 50, 102, 104).
- [144] ALICE Collaboration. *Elliptic flow of electrons from heavy-flavour hadron decays at mid-rapidity in Pb-Pb collisions at $\sqrt{s_{NN}} = 2.76$ TeV*. 2016. arXiv: 1606.00321. URL: <http://cds.cern.ch/record/2154390> (cit. on pp. 50, 99).
- [145] PHENIX Collaboration. “Measurement of Single Electrons and Implications for Charm Production in $Au + Au$ Collisions at $\sqrt{s_{NN}} = 130$ GeV”. In: *Phys. Rev. Lett.* 88.192303 (2002). DOI: 10.1103/PhysRevLett.88.192303. arXiv: nucl-ex/0202002 (cit. on p. 50).
- [146] N. Borghini, P. M. Dinh and Jean-Yves Ollitrault. “New method for measuring azimuthal distributions in nucleus-nucleus collisions”. In: *Phys. Rev. C* 63.054906 (2001). DOI: 10.1103/PhysRevC.63.054906. arXiv: nucl-th/0007063 (cit. on pp. 50, 53, 55).
- [147] N. Borghini, P. M. Dinh and Jean-Yves Ollitrault. “Flow analysis from multiparticle azimuthal correlations”. In: *Phys. Rev. C* 64.054901 (2001). DOI: 10.1103/PhysRevC.64.054901. arXiv: nucl-th/0105040 (cit. on p. 50).
- [148] A. Bilandzic, R. Snellings and S. Voloshin. “Flow analysis with cumulants: Direct calculations”. In: *Phys. Rev. C* 83.044913 (2011). DOI: 10.1103/PhysRevC.83.044913. arXiv: 1010.0233 (cit. on p. 50).
- [149] STAR Collaboration. “Elliptic flow from two- and four-particle correlations in $Au + Au$ collisions at $\sqrt{s_{NN}} = 130$ GeV”. In: *Phys. Rev. C* 66.034904 (2002). DOI: 10.1103/PhysRevC.66.034904. arXiv: nucl-ex/0206001 (cit. on pp. 50, 53).
- [150] S. Voloshin and Y. Zhang. “Flow study in relativistic nuclear collisions by Fourier expansion of azimuthal particle distributions”. In: *Z. Phys. C* 70(4) (1996), pp. 665–672. DOI: 10.1007/s002880050141. arXiv: hep-ph/9407282 (cit. on p. 52).
- [151] M. Luzum and Jean-Yves Ollitrault. “Eliminating experimental bias in anisotropic-flow measurements of high-energy nuclear collisions”. In: *Phys. Rev. C* 87.044907 (2013). DOI: 10.1103/PhysRevC.87.044907. arXiv: 1209.2323 (cit. on p. 55).
- [152] J. Podolanski and R. Armenteros. “Analysis of V-Events”. In: *Phil. Mag.* 45(360) (1954), pp. 13–30. DOI: 10.1080/14786440108520416 (cit. on p. 64).
- [153] N. M. Kroll and W. Wada. “Internal pair production associated with the emission of high-energy gamma rays”. In: *Phys. Rev.* 98 (1955), pp. 1355–1359. DOI: 10.1103/PhysRev.98.1355 (cit. on p. 74).
- [154] L. Ametlle et al. “Transition form-factors in π^0 , η and η' couplings to $\gamma\gamma^*$ ”. In: *Phys. Rev. D* 45(3) (1992), pp. 986–989. DOI: 10.1103/PhysRevD.45.986. URL: <http://cds.cern.ch/record/224283> (cit. on p. 75).

- [155] Jefferson Lab Collaboration. “Charged pion form factor between $Q^2 = 0.60$ and 2.45 GeV^2 . II. Determination of, and results for, the pion form factor”. In: *Phys. Rev. C* 78.045203 (2008). DOI: 10.1103/PhysRevC.78.045203. arXiv: 0809.3052 (cit. on p. 75).
- [156] R. Escribano. “A rational approach to η and η' transition form factors”. In: *Int. J. Mod. Phys. Conf. Ser.* 35.1460398 (2014). DOI: 10.1142/S2010194514603986. arXiv: 1403.7449 (cit. on p. 75).
- [157] S.R. Amendolia et al. “A Measurement of the Pion Charge Radius”. In: *Phys. Lett. B* 146(1-2) (1984), pp. 116–120. DOI: 10.1016/0370-2693(84)90655-5. URL: <http://cds.cern.ch/record/151706> (cit. on p. 75).
- [158] A2 Collaboration. “New determination of the η transition form factor in the Dalitz decay $\eta \rightarrow e^+e^-\gamma$ with the Crystal Ball/TAPS detectors at the Mainz Microtron”. In: *Phys. Rev. C* 89.044608 (2014). DOI: 10.1103/PhysRevC.89.044608. arXiv: 1309.5648 (cit. on p. 75).
- [159] TPC/Two Gamma Collaboration. “Investigation of the electromagnetic structure of η and η' mesons by two-photon interactions”. In: *Phys. Rev. Lett.* 64 (1990), p. 172. DOI: 10.1103/PhysRevLett.64.172. URL: http://ccdb5fs.kek.jp/cgi-bin/img_index?8911395 (cit. on p. 75).
- [160] ALICE Collaboration. “Neutral pion production at midrapidity in pp and Pb–Pb collisions at $\sqrt{s_{NN}} = 2.76 \text{ TeV}$ ”. In: *Eur. Phys. J. C* 74.3108 (2014). DOI: 10.1140/epjc/s10052-014-3108-8. arXiv: 1405.3794 (cit. on p. 79).
- [161] ALICE Collaboration. “Production of charged pions, kaons and protons at large transverse momenta in pp and Pb–Pb collisions at $\sqrt{s_{NN}} = 2.76 \text{ TeV}$ ”. In: *Phys. Lett. B* 736 (2014), pp. 196–207. DOI: 10.1016/j.physletb.2014.07.011. arXiv: 1401.1250 (cit. on p. 79).
- [162] P. K. Khandai, P. Shukla and V. Singh. “Meson spectra and m_T scaling in p+p, d+Au and Au+Au collisions at $\sqrt{s_{NN}} = 200 \text{ GeV}$ ”. In: *Phys. Rev. C* 84 (2011). DOI: 10.1103/PhysRevC.84.054904. arXiv: 1110.3929 (cit. on p. 81).
- [163] ALICE Collaboration. “Neutral pion and η meson production in proton-proton collisions at $\sqrt{s} = 0.9 \text{ TeV}$ and 7 TeV ”. In: *Phys. Lett. B* 717 (2012), pp. 162–172. DOI: 10.1016/j.physletb.2012.09.015. arXiv: 1205.5724 (cit. on pp. 81, 96).
- [164] ALICE Collaboration. “Production of $K^*(892)^0$ and $\phi(1020)$ in pp collisions at $\sqrt{s} = 7 \text{ TeV}$ ”. In: *Eur. Phys. J. C* 72.2183 (2012). DOI: 10.1140/epjc/s10052-012-2183-y. arXiv: 1208.5717 (cit. on p. 81).
- [165] ALICE Collaboration. “Neutral meson production in pp and Pb-Pb collisions at the LHC measured with ALICE”. In: *Nucl. Phys. A* 904-905 (2013), pp. 755c–758c. DOI: 10.1016/j.nuclphysa.2013.02.127. arXiv: 1210.5749 (cit. on p. 81).
- [166] T. Sjostrand S. Mrenna and P. Skands. “PYTHIA 6.4 physics and manual”. In: *JHEP* 0605.026 (2006). DOI: 10.1088/1126-6708/2006/05/026. arXiv: hep-ph/0603175 (cit. on pp. 81, 89).

- [167] ALICE Collaboration. “Measurement of Direct Photons in pp and Pb-Pb Collisions with ALICE”. In: *Nucl. Phys. A* 904-905 (2013), pp. 573c–576c. DOI: 10.1016/j.nuclphysa.2013.02.079. arXiv: 1210.5958 (cit. on p. 82).
- [168] ALICE Collaboration. “Direct photon production in Pb-Pb collisions at $\sqrt{s_{NN}} = 2.76$ TeV”. In: *Phys. Lett. B* 754 (2016), pp. 235–248. DOI: 10.1016/j.physletb.2016.01.020. arXiv: 1509.07324 (cit. on p. 82).
- [169] W. Vogelsang. “Next-to-leading order hadronic single-spin production of polarized prompt photons”. In: *Phys. Rev. D* 50(7) (1994), pp. 4436–4446. DOI: 10.1103/PhysRevD.50.4436. URL: <http://cds.cern.ch/record/260297> (cit. on p. 82).
- [170] ALICE Collaboration. “Anisotropic flow of charged hadrons, pions and (anti-)protons measured at high transverse momentum in Pb-Pb collisions at $\sqrt{s_{NN}} = 2.76$ TeV”. In: *Phys. Lett.* 719 (2013), pp. 18–28. DOI: 10.1016/j.nuclphysa.2013.02.058. arXiv: 1205.5761 (cit. on p. 85).
- [171] ALICE Collaboration. “Spectra and elliptic flow for identified hadrons in 2.76 A TeV Pb+Pb collisions”. In: *Phys. Rev. C* 89.034919 (2014). DOI: 10.1103/PhysRevC.89.034919. arXiv: 1311.0157 (cit. on p. 85).
- [172] Daniel Lohner. “Anisotropic flow of direct photons in Pb-Pb collisions at $\sqrt{s_{NN}} = 2.76$ TeV”. CERN-THESIS-2013-158. PhD thesis. Ruperto-Carola-University, 2013. URL: <https://cds.cern.ch/record/1611118> (cit. on pp. 85, 87).
- [173] CMS Collaboration. “Measurement of the Azimuthal Anisotropy of Neutral Pions in Pb-Pb Collisions at $\sqrt{s_{NN}} = 2.76$ TeV”. In: *2013* 110.042301 (Phys. Rev. Lett.). DOI: 10.1103/PhysRevLett.110.042301. arXiv: 1208.2470 (cit. on p. 85).
- [174] PHENIX Collaboration. “Observation of Direct-Photon Collective Flow in Au + Au Collisions at $\sqrt{s_{NN}} = 200$ GeV”. In: *Phys. Rev. Lett.* 109.122302 (2012). DOI: 10.1103/PhysRevLett.109.122302. arXiv: 1105.4126 (cit. on p. 87).
- [175] R. Brun et al. *GEANT 3*. CERN-DD-EE-84-1. CERN. 1987. URL: <http://cds.cern.ch/record/1119728/> (cit. on p. 90).
- [176] GEANT4 Collaboration. “GEANT4: A Simulation toolkit”. In: *Nucl. Instrum. Meth. A* 506 (2003), pp. 250–303. DOI: 10.1016/S0168-9002(03)01368-8. URL: <http://cds.cern.ch/record/602040> (cit. on p. 90).
- [177] Miklos Gyulassy and Xin-Nian Wang. “HIJING 1.0: A Monte Carlo program for parton and particle production in high-energy hadronic and nuclear collisions”. In: *Comput.Phys.Commun.* 83 (1994), pp. 307–331. DOI: 10.1016/0010-4655(94)90057-4. arXiv: nucl-th/9502021 (cit. on p. 101).
- [178] Yu. L. Dokshitzer and D. E. Kharzeev. “Heavy quark colorimetry of QCD matter”. In: *Phys. Lett. B* 519 (2001), pp. 199–206. DOI: 10.1016/S0370-2693(01)01130-3. arXiv: hep-ph/0106202 (cit. on p. 102).

- [179] B.-W. Zhang, E. Wang and X.-N. Wang. “Heavy Quark Energy Loss in Nuclear Medium”. In: *Phys. Rev. Lett.* 93.072301 (2004). DOI: 10.1103/PhysRevLett.93.072301. arXiv: nucl-th/0309040 (cit. on p. 102).
- [180] R. Rapp and H. van Hees. *Heavy Quark Diffusion as a Probe of the Quark-Gluon Plasma*. 2008. arXiv: 0803.0901. URL: <http://cds.cern.ch/record/1093074> (cit. on p. 102).
- [181] J. Uphoff et al. “Open heavy flavor in Pb + Pb collisions at $\sqrt{s_{NN}} = 2.76$ TeV within a transport model”. In: *Phys. Lett.* 717 (2012), pp. 430–435. DOI: 10.1016/j.physletb.2012.09.069. arXiv: 1205.4945 (cit. on p. 102).
- [182] J. Uphoff et al. “Heavy vs. light flavor energy loss within a partonic transport model”. In: *J. Phys. Conf. Ser.* 509.012077 (2014). DOI: 10.1088/1742-6596/509/1/012077. arXiv: 1310.3597 (cit. on p. 102).
- [183] M. Nahrgang et al. “Influence of hadronic bound states above T_c on heavy-quark observables in Pb + Pb collisions at the CERN Large Hadron Collider”. In: *Phys. Rev. C* 89.014905 (2014). DOI: 10.1103/PhysRevC.89.014905. arXiv: 1305.6544 (cit. on p. 102).
- [184] W. M. Alberico et al. “Heavy flavor production in pp and AA collisions at the LHC”. In: *Nucl. Phys. A* 910-911 (2013), pp. 395–398. DOI: 10.1016/j.nuclphysa.2012.12.066. arXiv: 1208.0705 (cit. on p. 104).
- [185] W. M. Alberico et al. “Heavy flavours in AA collisions: production, transport and final spectra”. In: *Eur. Phys. J. C* 73.2481 (2013). DOI: 10.1140/epjc/s10052-013-2481-z. arXiv: 1305.7421 (cit. on p. 104).
- [186] M. He, R. J. Fries and R. Rapp. “Heavy Flavor at the Large Hadron Collider in a Strong Coupling Approach”. In: *Phys. Lett.* 735 (2014), pp. 445–450. DOI: 10.1016/j.physletb.2014.05.050. arXiv: 1401.3817 (cit. on p. 104).
- [187] ALICE Collaboration. *Upgrade of the ALICE Time Projection Chamber*. CERN-LHCC-2013-020; ALICE-TDR-016. CERN. URL: <http://cds.cern.ch/record/1622286> (cit. on p. 104).
- [188] K. Pearson. “Contributions to the Mathematical Theory of Evolution. II. Skew Variation in Homogeneous Material”. In: *Phil. Trans. A* 186 (1895), pp. 343–414. DOI: 10.1098/rsta.1895.0010. URL: <http://www.jstor.org/stable/90649> (cit. on p. 109).
- [189] K. Pearson. “Mathematical Contributions to the Theory of Evolution. X. Supplement to a Memoir on Skew Variation”. In: *Phil. Trans. A* 197 (1901), pp. 443–459. DOI: 10.1098/rsta.1901.0023. URL: <http://www.jstor.org/stable/90841> (cit. on p. 109).
- [190] K. Pearson. “Mathematical Contributions to the Theory of Evolution. XIX. Second Supplement to a Memoir on Skew Variation”. In: *Phil. Trans. A* 216 (1916), pp. 429–457. DOI: 10.1098/rsta.1916.0009. URL: <http://www.jstor.org/stable/91092> (cit. on p. 109).

- [191] N. L. Johnson. “Systems of Frequency Curves Generated by Methods of Translation”. In: *Biometrika* 36 (1949), pp. 149–176. DOI: 10.1093/biomet/36.1-2.149. URL: <http://www.jstor.org/stable/2332539> (cit. on p. 109).
- [192] A. O’Hagan and T. Leonard. “Bayes estimation subject to uncertainty about parameter constraints”. In: *Biometrika* 63(1) (1976), pp. 201–203. DOI: 10.1093/biomet/63.1.201 (cit. on p. 109).
- [193] M. K. Varanasi and B. Aazhang. “Parametric generalized Gaussian density estimation”. In: *J. Acoust. Soc. Am.* 86 (1989), p. 1404. DOI: 10.1121/1.398700 (cit. on p. 111).
- [194] P. J. Rousseeuw and K. Van Driessen. “Computing LTS Regression for Large Data Sets”. In: *Data Min. Knowl. Discov* 12(1) (2006), pp. 29–45. DOI: 10.1007/s10618-005-0024-4 (cit. on p. 112).
- [195] J. A. Doornik. *Robust Estimation Using Least Trimmed Squares*. 2011. URL: http://econ.au.dk/fileadmin/site_files/filer_oekonomi/subsites/creates/Seminar_Papers/2011/ELTS.pdf (cit. on p. 112).
- [196] G. D’Agostini and M. Raso. *Uncertainties due to imperfect knowledge of systematic effects: general considerations and approximate formulae*. CERN-EP-2000-026. 2000. arXiv: hep-ex/0002056. URL: <http://cds.cern.ch/record/427962> (cit. on pp. 113, 114).